

**EFFECT OF SHAPE AND PARTICLE COORDINATION ON COLLECTIVE
DYNAMICS OF GRANULAR MATTER**

A Dissertation
Presented to
The Academic Faculty

By

William C. Savoie

In Partial Fulfillment
of the Requirements for the Degree
Doctor of Philosophy in the
School of Physics

Georgia Institute of Technology

May 2019

Copyright © William C. Savoie 2019

**EFFECT OF SHAPE AND PARTICLE COORDINATION ON COLLECTIVE
DYNAMICS OF GRANULAR MATTER**

Approved by:

Dr. Daniel I. Goldman, Advisor
School of Physics
Georgia Institute of Technology

Dr. James Gumbart
School of Physics
Georgia Institute of Technology

Dr. Peter Yunker
School of Physics
Georgia Institute of Technology

Dr. Kurt Wiesenfeld
School of Physics
Georgia Institute of Technology

Dr. Dana Randall
College of Computing
Georgia Institute of Technology

Date Approved: February 26, 2019

I sell propane and propane accessories

Hank Hill

For Mom and Caine.

ACKNOWLEDGEMENTS

Without the support of my mother and my brother, I cannot imagine where I would be. You are both my biggest role models, and I strive to be more like you both.

I want to thank all of my friends, you make life worth living. I'd like to give a special thanks to Steve Carter, you have dramatically altered the course of my life, I am forever in your debt. I want to thank my fellow lab mates, with a special thanks to Perrin Schiebel: your friendship these past few years was irreplaceable, let's keep it that way. Furthermore, I'd like to thank Tingnan Zhang and Shengkai Li as well, I would have made far less progress without y'all.

Lastly, I would like to thank Prof. Goldman for letting me stick around for the whole ride: I know I can be tough to deal with at times. My greatest joy during this process was learning all the various techniques and skills to work on so many projects. Thank you for the opportunity.

TABLE OF CONTENTS

Acknowledgments	v
List of Tables	x
List of Figures	xi
Chapter 1: Introduction and Background	1
1.1 Overview and motivation	1
1.2 Geometric Mechanics	2
1.2.1 Introduction	3
1.2.2 Robophysics	5
1.2.3 Modeling granular media systems	6
1.3 Smarticles: shape changing particles	8
1.3.1 Smarticles	9
1.3.2 Kinematic Mount	10
1.4 Biological active granular matter	12
1.4.1 Introduction	12
1.4.2 Model organism: the fire ant	13
1.5 Organization of the thesis	13

Chapter 2: Reversibility in granular materials	21
2.1 Summary	21
2.1.1 Introduction	22
2.2 Materials and methods	25
2.2.1 Robotic design	25
2.2.2 Plastic particle system	26
2.2.3 Poppy seed system	27
2.2.4 Illustrative example data	29
2.3 Results and discussion	30
2.3.1 Reversibility as a function of depth in media	30
2.3.2 Reversibility as a function of frequency	31
2.3.3 Reversibility as a function of volume fraction	32
2.4 Conclusion	33
Chapter 3: Applying geometric mechanics to the hybrid dynamical smarticle crawler	41
3.1 Summary	41
3.2 Introduction	42
3.3 Materials and methods	43
3.4 Results and discussion	47
3.5 Conclusion	53
Chapter 4: Supersmarticle	55
4.1 Summary	55

4.2	Introduction	56
4.3	Material and methods	57
4.4	Results and discussion	58
4.4.1	Smarticle cloud	58
4.4.2	Supersmarticle dynamics	59
4.4.3	Statistical model	61
4.5	Conclusion	66
4.6	Appendix	68
Chapter 5: Smarticle Chain		72
5.1	Summary	72
5.2	Introduction	72
5.3	Materials and methods	73
5.3.1	Multibody simulation of smarticles	73
5.3.2	Experimental system	77
5.4	Results and Discussion	80
5.4.1	Simulation	80
5.4.2	Experiment	85
5.5	Conclusion	86
Chapter 6: Simulations of traffic and workload distribution in fire ant nest construction		88
6.1	Summary	88
6.2	Introduction	89

6.2.1	Simulated system	90
6.3	Materials and methods	91
6.4	Results and discussion	98
6.5	Conclusion	103
6.6	Appendix	104
Chapter 7: Conclusion		105
7.1	General Remarks	105
References		119

LIST OF TABLES

4.1	list of all six different types of collisions which are possible in the supersmarticle theoretical model	69
4.2	Supersmarticle theoretical model parameters	71
5.1	Smarticle chain simulation parameters	77
6.1	Parameters for CA Simulation	104

LIST OF FIGURES

1.1	Granular media at various size scales	2
1.2	GM comparison between theory and experiment	4
1.3	Example robots used in robophysical studies	6
1.4	DEM collision schematic	7
1.5	3 Smarticle systems	9
1.6	Kinematic mounting surface feet	11
1.7	Supersmarticle, and single smarticle front and back views	15
1.8	Smarticle coordinate system	16
1.9	Smarticle circuit diagram	17
1.10	smarticle PCB layouts	18
1.11	Unequal workload in seen in quasi-2D ant experiment	19
1.12	Size, location, and nest information of fire ants	19
1.13	Fire ant morphology	20
2.1	Granular shearing leading to compaction, dilation, and the critical state	24
2.2	Illustration and experimental version of scallop robot	25
2.3	Experimental setup schematic	26
2.4	Scallop robot experiment procedure definition	29

2.5	Eliminating established reversibility	35
2.6	Forward and backward stroke displacements in plastic particles	36
2.7	Effect of stroke angular speed	36
2.8	Position as a function of time at various compactions	37
2.9	Scallop asymptotic behavior of displacement at varied compactions	38
2.10	Scallop position after 6 strokes at varied compactions	39
2.11	Displacement versus compaction for the second full cycle and first half cycle	40
3.1	Illustration of square and diamond gait	43
3.2	Smarticle walker experimental setup	44
3.3	Experimental crawling system and gait schematic	45
3.4	Crawl speed as a function of gait size, for different l/w	48
3.5	Local connection and CCF of smarticle crawler	49
3.6	Diamond gait comparison for simulation, theory, and experiment	50
3.7	Square gait comparison for simulation, theory, and experiment	52
4.1	Smarticle robot and dynamics	57
4.2	Smarticle cloud cooling and diffusion	60
4.3	Collective confined diffusion	62
4.4	Supersmarticle drift and model	64
4.5	Supersmarticle phototaxis	67
4.6	Unrotated trajectories for different mass ratios	68
5.1	System entanglement procedures	75

5.2	Smarticle chain experimental setup	78
5.3	Comparing energy usage between procedures	81
5.4	Comparing entangling procedures	83
5.5	Force versus time for different systems	84
5.6	Single fracture trial for n=2 and n=6 smarticles	86
5.7	Auxetic behavior in smarticle chain	87
6.1	Lorenz curve and Gini coefficient	92
6.2	Schematic of the tunnel in CA	94
6.3	Average number of ants involved in a clog C in simulation	95
6.4	Ant cluster analysis	96
6.5	Diagram illustration of genetic algorithm	97
6.6	Measured Gini coefficient versus assigned Gini	99
6.7	Ant experimental results and CA calibration	100
6.8	GA applied to CA	102

SUMMARY

Particle shape and coordination in granular materials (GM) can impact the material properties of an aggregate. GM are generally described as collections of particles which are macroscopic, discrete, a-thermal, and dissipative. While seemingly simple to understand the dynamics of systems containing only a handful of particles, larger aggregations can have complex and emergent dynamics. Materials with dynamic properties can be made if the constituent particles are capable of altering their shape and coordination. In this thesis, to elucidate principles in GM systems, we study systems both biological and robotic where particle shape and coordination on the single particle scale alters macroscopic system dynamics. We start by studying how grain shape affects reversibility for a robotic swimmer performing reciprocal strokes in GM. We find that although displacement on initial strokes for a such a swimmer are affected by the initial compaction of a GM, a bifurcation in the displacement response leads to a final displacement and eventual asymptotic reversibility independent of initial compaction. We then shift to the study of active particles, with a special focus on a robotic system featured heavily in this dissertation: smarticles. Smarticles are a shape changing 3-link robot designed in our lab. We start by examining single smarticle crawling dynamics. We apply geometric mechanics, a theoretical framework which relates body speed and shape speed for swimmers in viscous-like environments and discover it can be used for this hybrid dynamical system. Another project examines how shape change can be used as a rudimentary control scheme for swarm robotic systems without a centralized control or communication. In our final smarticle system, we reveal how material properties of a collective can be transformed by modifying entanglements between particles. Lastly, inspired by biophysical studies of ants, we use simulation to gain insights into traffic flow for densely packed, confined, task-oriented, active GM systems. Our results reveal features necessary to avoid traffic jams when faced with certain constraints such as confined conditions, minimal communication, and an over-sized workforce.

CHAPTER 1

INTRODUCTION AND BACKGROUND

1.1 Overview and motivation

Granular media (GM) is a collection of a-thermal, discrete, macroscopic particles which interact through dissipative contact forces [1]. GM is ubiquitous and exists at all scales, examples include asteroid belts, planetary rings, deserts, and beaches to name a few see fig. 1.1. Aside from the natural world, granular systems are extremely common even in artificial circumstances: it is estimated that more than 50% of sales in the world involve commodities produced using GMs, making GM one of the most used materials in industry, second only to water [2]. Perhaps even more surprisingly, it is estimated that the processing of GMs accounts for 10% of the worlds energy consumption [3].

GM contains a wealth of interesting and complex phenomenon, despite being composed of relatively simple elements. On the scale of aggregations, interactions of the constituents in a GM lead to complex and sometimes non-intuitive outcomes [3, 4, 5]. GM exhibit many emergent behaviors, jamming [6, 7], shear banding [8], and Reynolds dilatancy [9] to name a few. Since granular systems, and the physics associated with them, can exist on a variety of length scales, the principles gleaned from a system at one particular scale can often be applied to systems on separate scales. In this dissertation, we will be studying granular systems on the mm and cm scale in robotic and biological systems.

Smart materials is becoming a popular field in the field of microrobotics, especially with the creation of microelectromechanical systems or MEMS [10]. Smart materials are defined as those which can sense and react, in intelligent ways, to external stimuli. We posit such materials would likely contain many robotic elements making it essentially granular in nature, or in the robotics and biological community, a swarm system. Many current arti-

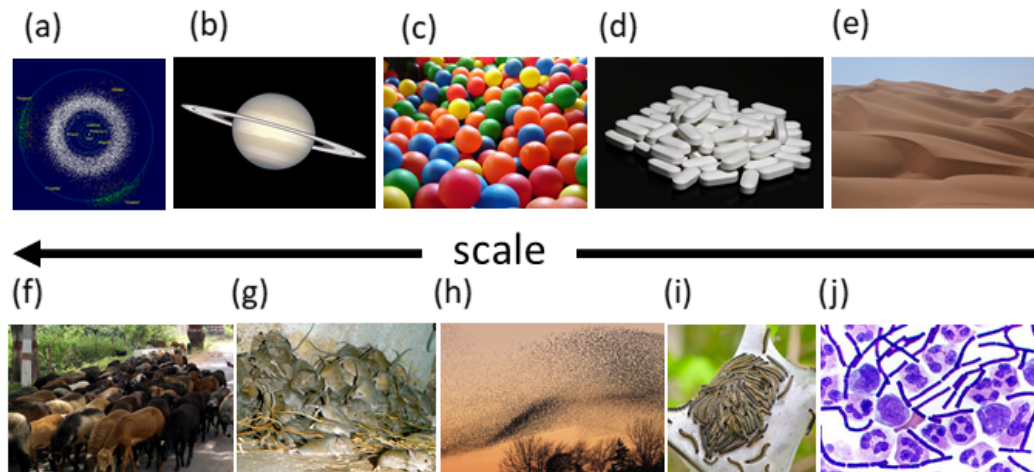


Figure 1.1: **Granular media at various size scales** (a-e) Passive GM: (a) asteroid belt (b) planetary rings (Saturn pictured) (c) children’s ball pit balls (d) pharmaceuticals (calcium supplements shown) (e) sand in a desert in UAE. (f-j) Active GM: (f) herd of sheep (g) mischief of rats (h) murmuration of starlings (i) army of tent caterpillars (j) culture of bacteria (anthrax shown).

ficial swarm systems share the characteristic of collision detection and avoidance. [11, 12, 13, 14]. Indeed, for many state-of-the-art-systems, motion is highly coordinated and communications are used to ensure collisions are rare or even non-existent. Many biological do not share the same aversion interactions fig. 1.1(f-j), some of these highly interactive biological systems are even called active granular systems [15, 16]. In this thesis, we combine robotics and GM research: bridging a gap between the two.

1.2 Geometric Mechanics

When developing robots with locomotion capabilities, it can be difficult to determine how to properly sequence the limbs, flippers, or even the entire body, of a robot such that the motion produced is desirable. Rather than using trial and error for each new project, for certain systems, there exist theoretical frameworks which can guide the development. In this section we will introduce one such theory, which will be used in chapter 2 and chapter 3.

1.2.1 Introduction

In low Reynolds number fluids ($Re \ll 1$), viscosity dominates inertia. For an incompressible fluid, Navier-Stokes is defined by

$$\frac{\partial \mathbf{u}}{\partial t} + \mathbf{u} \cdot \nabla \mathbf{u} = -\frac{\nabla P}{\rho} + \nu \nabla^2 \mathbf{u} \quad (1.1)$$

where \mathbf{u} is the flow velocity, t is time, P is pressure, ρ is the density and ν is the kinematic viscosity. By eliminating the inertial terms, eq. (1.1) simplifies to,

$$\nabla P = \nu \nabla^2 \mathbf{u} \quad (1.2)$$

which is both linear and time independent. Motions inside a low Reynolds number are reversible[17, 18]. Reciprocal motions are motions sequences of motions which appear the same when viewed forwards or backwards in time, in low Reynolds systems, such movements produce zero net displacement. Although GM cannot be described by Navier-Stokes, it does share some similarities with low Reynolds number fluids.

In GM, friction between grains, and along the body of a body of a swimmer, dominate inertia. When a swimmer stops actuating its body, the body velocity should instantaneously go to zero, a feature of low Reynolds number systems. In one particular study performed previously in our lab, sand swimmers, like the sandfish lizard *Scincus scincus*, were observed in natural GM to reach steady states within a fraction of a cycle [19]. As a result, it was hypothesized granular swimmers could be analyzed in a similar way as swimmers in low Reynolds fluids. To analyze such systems, or any where body velocity is linearly related to shape velocity, is by employing a theory called “geometric mechanics”. While flow in GM is not strictly reversible, a requirement for the theory, the theory has been successfully used to describe motion through GMs resulting from body deformations [20, 21, 22].

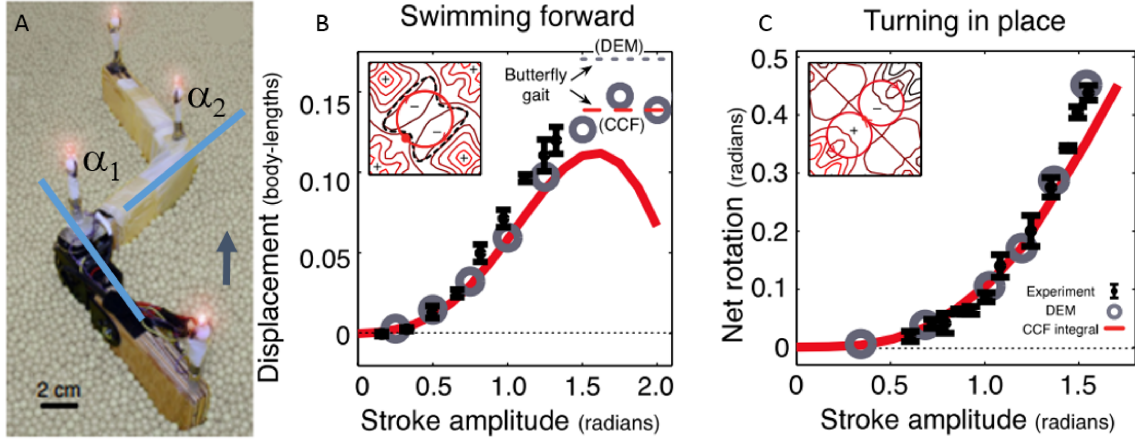


Figure 1.2: **Comparison of geometric mechanics and a robophysical sandswimming robotic model** (A). The experimental robotic version of the 3-link swimmer. The robot inside a bed of 6 mm diameter plastic spheres. (b) Comparison of translational performance between curvature constraint function (CCF) prediction, DEM predictions, and robotic results for a 3-link swimmer (red, gray, and black respectively) performing a butterfly gait shown in top left inset. Using a similar colorscheme as (b), (c) measures rotational performance for a figure-8 gait shown in the inset. [25]

For highly dissipative environments, a framework was developed by Shapere and Wilczek [18], relating displacements in the world frame to deformations in the body-frame. This framework requires self-deformations which are kinematic, or rate dependent. The key contribution was applying gauge symmetries or equivalencies in the system dynamics over different configurations, simplifying systems by reducing the effective dimensionality of the system. By utilizing the gauge symmetries, the dynamics of the system can be understood in terms of geometric concepts like area, lengths, and curvatures. This geometric approach was further developed [23, 24, 20] allowing analysis of certain locomotors' dynamics in comparably lower dimensions than the configuration space of the swimmer itself.

Recent work from our lab showed that a 3-link robot swimming through symmetric, low friction, spherical GM has some similarity to low Reynolds number swimmers and therefore can be analyzed using geometric mechanics [25]. In chapter 2 we study the existence of reversibility in two GM systems. Besides the three-link swimmer, many other granular locomotors have been recently studied using geometric mechanics [22, 21, 26, 27].

Without geometric mechanics, the study GM swimmers can be quite challenging as there is no generalized formula for granular flows as exists for fluids. Geometric mechanics is used again in chapter 3; we examine the extent to which the theory can be used to describe the crawling performance of a hybrid-dynamical crawling robot. In both chapters, robotic systems are used to explain and test this theory.

1.2.2 Robophysics

When probing the fundamental physics of a system, there are many ways to attack a problem. One style of experimentation, useful for understanding physical principles in locomoting systems, is called “robophysics” [28]. Robophysics is defined as “the pursuit of principles governing movement and ... control of self-deforming entities interacting with a complex environment” [28]. Recently robophysics has become a common tool for examining various systems in our lab [22, 29, 16, 30, 31, 32, 21, 25].

When systems are reconstructed in a robotic form, we are free to abstract away non-essential features, something not always possible when using biological specimens. This is useful for many reasons: robots, unlike animals or biological specimens, do not get tired, are highly controllable, and perhaps most importantly, allow for high repeatability in testing because of the features listed above. In our lab, robots were used to study limbless locomotion [33], the importance of tail usage for climbing up sandy slopes [21], and even principles relating to jumping performance on hard-ground and in GM[34].

In robophysics, robots are used as a tool to measure, probe, and discover physical principles. A theme of robophysics is it allows discovery of new principles not always deducible from those previously known. In such cases, these principles may be difficult to discover in simulation or theory alone*. A mistake or unexpected result in an experiment may be the motivation of an entirely new study (see chapter 4). As such, a robot failing to perform effectively can be as valuable as, if not more than, the successes. Insights should

*See Ablowitz’s “The Theory of Emergence” for a short but beautiful discussion of emergent versus resultant properties [35]

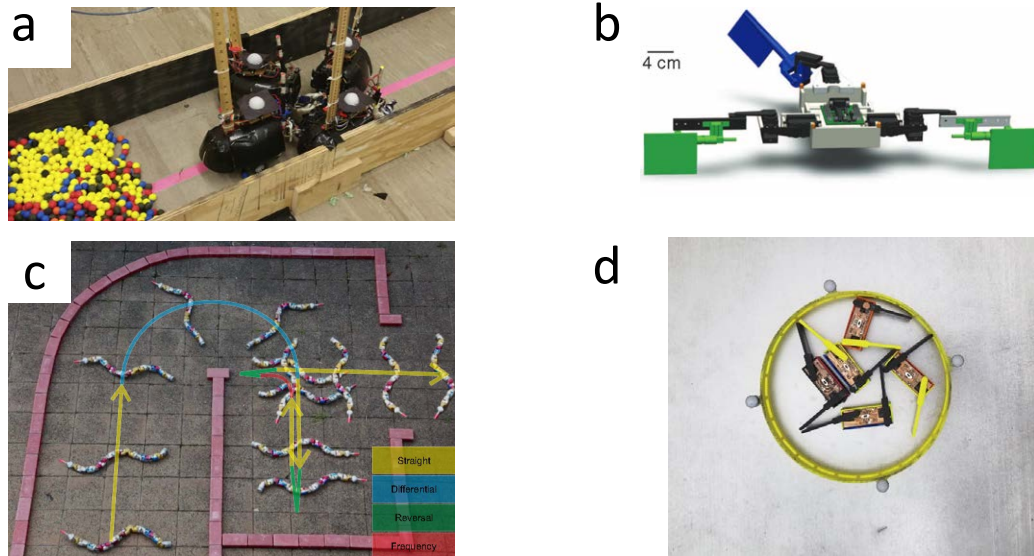


Figure 1.3: **Example robots used in robophysical studies** (a) Ant robots used to discover principles behind traffic in fire ant nests [16]. (b) Mudskipper robot used to discover principles behind tail usage when climbing sandy slopes (figure reproduced from [21]) (c) Sidewinder robot used to help understand the complex side-winding behavior seen in certain snakes (figure reproduced from [33]). (d) Supersmarticle robot, or robot made of robots, discussed in detail in chapter 4 is used to discover interaction based control schemes

be broad and useful for both already existing or future robotic systems, rather than for useful for optimizing only a single robotic instantiation. The majority of this dissertation takes either a robophysical approach to study the dynamics of many bodies systems, or uses simulation to model robophysical experiments.

1.2.3 Modeling granular media systems

Since GM systems have no comprehensive set of equations describing their dynamics, another popular method of studying GM systems is through numerical simulations. Interactions between grains can be modeled by repulsive dissipative contact forces. One style of modeling such interactions is known as discrete element method or DEM. DEM can recover and reproduce many granular phenomena seen in real life systems.

In DEM, the dynamics of a system is simulated by computing the movement of every particle by calculating the interaction forces between each pair of grains in contact [36,

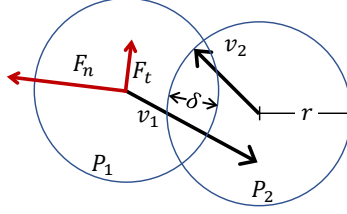


Figure 1.4: **DEM collision schematic** Two particles, P_1 and P_2 , with radius r interact with velocities \mathbf{v}_1 and \mathbf{v}_2 respectively. The force between particles, \mathbf{F}_n and \mathbf{F}_t , is computed and is a function of the virtual overlap δ . δ approximates the elastic deformation which can happen between colliding bodies.

37]. These contact forces are broken down into a normal, F_n , and a tangential, F_t , component [38, 39, 40]

$$F_n = k_n \delta^{3/2} - g_n v_n \delta^{1/2} \quad (1.3)$$

$$F_t = \mu F_n$$

δ is the virtual overlap, k_n is the particle stiffness, v_n is the normal component of the relative velocity, g_n is the viscoelasticity dissipation coefficient, and μ is the friction coefficient.

For the normal component, when particles collide in DEM, they interpenetrate one another, the amount of penetration is known as the virtual overlap, or δ seen in fig. 1.4. This virtual overlap is meant to represent particle deformation or strain present during interactions and the the stiffness scales the strength of the resultant force expelling the interpenetrated particles. Energy lost during a collision is represented by the second term in F_n , and it scales with g_n . The two coefficients together, k_n and g_n , produce the velocity dependent coefficient of restitution. For the tangential forces in eq. (1.3) we use the normal Coulomb friction model. The values used for all previously mentioned coefficients are found from experiment.

To simulate systems where non-granular components perform actions on granular systems, we coupled multibody simulators with DEM. A multibody simulation is a type of numerical simulation where the dynamic behavior of interconnected bodies is computed. Such systems include those with many complex-shaped and articulated rigid bodies. Multi-

body simulations have a wide range of uses, not only in academia but also in industry. For example, they have been used for product development [41], to model vehicle dynamics [42, 43], in the medical field to analyze injuries sustained by the human body under various conditions [44, 45, 46], and even used in robotics research [47, 48]

Multibody engines solve the Newton-Euler equations:

$$\begin{pmatrix} M & 0 \\ 0 & I \end{pmatrix} \begin{pmatrix} \dot{v} \\ \dot{\omega} \end{pmatrix} + \begin{pmatrix} 0 \\ \omega \times I\omega \end{pmatrix} = \begin{pmatrix} \mathbf{f} \\ \boldsymbol{\tau} \end{pmatrix} \quad (1.4)$$

here M and I are the mass and moment of inertia matrices, v and ω are the translation and rotational velocities, and finally, f and τ are the external forces and torques. When rigid bodies are connected with joints, these create kinematic constraints which can be dealt with in various ways. One such way is by using Lagrange multipliers, the other is by eliminating by reformulating the problem using generalized coordinates [49, 50]. While all multibody simulation engines solve eq. (1.4), they do so with different methods. Different methods are used for a variety of reasons such as allowing easier adoption of the engine, or faster computation. The multibody engine we used in this dissertation is known as ProjectChrono [43, 42]. It is an open source multi-physics dynamics engine. ProjectChrono uses a novel method to simulate systems with large numbers of contacts and joints between rigid bodies. The fine details of their methodology go beyond the scope of this dissertation however, for more information see [51, 42, 43].

1.3 Smarticles: shape changing particles

Entangling happens all around us: from headphones forming into knots in our pockets, tangling polymers [52], or even in highly packed colonies of active biological systems like nematodes [53], sperm cells [54], or bacteria [55, 56] where entanglement is defined as the interpenetration between concave particles. “Smarticles”, or **Smart** active **particles** are a three-link robophysical experimental platform used to study how shape change affects

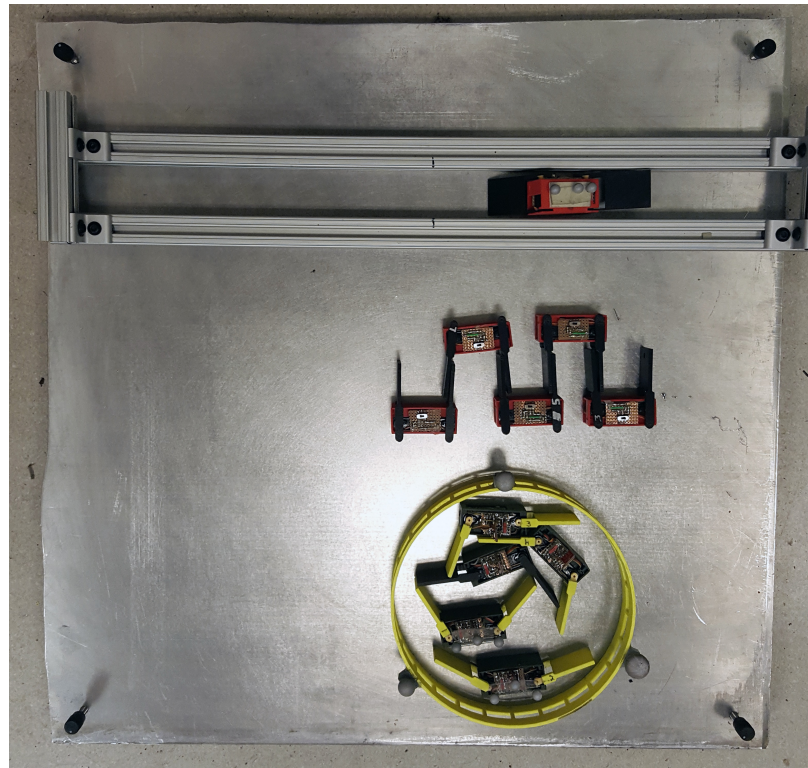


Figure 1.5: **3 Smarticle systems** All three planar smarticle experiments shown, from top to bottom: crawling smarticle, smarticle-chain, and the supersmarticle.

dynamics and rheology of granular systems. Experiments containing smarticles account for 3 separate chapters in this dissertation, chapters 3 to 5 (see fig. 1.5). In this section, we introduce the smarticle system.

1.3.1 Smarticles

In order to explore what emergent phenomena can result from collections of entities with limited mobility and sensing, we developed an experimental platform we call “smarticles.” Smarticles, or smart particles, are small 14 x 2.5 x 3 cm robots which can change their shape in situ, but depending on their orientation, may not be capable of individually generating translation or rotation. Each smarticle is a three-link, two revolute joint, planar robot where only the center link is in contact with the ground. Each smarticle consists of two Power HD-1440A MicroServos, a MEMS analog omnidirectional microphone, two photoresistors, a

current sensing resistor, and a re-programmable Arduino Pro Mini 328-3.3 V/8 MHz. The Arduino handles the ADC and servo control. Two servos control the smarticles' two outer links, allowing the smarticle to fully explore its two-dimensional configuration space. The microphone and pair of photoresistors are sensors which can be leveraged as a means of rudimentary communication, through which we can send basic commands. For the microphone, information is delivered via tone of specific frequencies. The tones are processed by an FFT library on the Arduino to determine the specific frequencies. The smarticle can recognize frequencies up to 1800 Hz with a fidelity of ± 10 Hz. The photoresistors measure light intensity: light incident on the photoresistors changes the resistance of the element. When used in series with a resistor with a constant resistance, the light intensity is determined via a voltage drop across the photoresistor. A current sensing resistor detects the current drawn by the servos, which is proportional to the torque experience. This allows each smarticle to sense its own stress state. The links of the smarticles were 3D printed, ensuring uniform construction between all smarticles.

1.3.2 Kinematic Mount

Since a main feature of the smarticles interactions is friction dependent (with the ground), it is imperative to reduce any asymmetries in the friction between the ground and smarticles as possible. Therefore, for the majority of smarticle experiments, it is imperative that they be performed on a flat surface. Many building floor surfaces are not perfectly flat and any gradients on the surface could cause an asymmetry in the friction skewing results. A kinematic mount was designed and built to serve as the experimental surface used by the smarticles. Kinematic mounts give both precise control of all rotational and translational degrees of freedom, and as a result, are robust against small external perturbations.

Kinematic mounts work by giving the user control over which degrees of freedom, rotational or translational, they wish to modify. An already flat surface (ensured by proper machining techniques) is threaded for screws. Each of the screws has a hemispherical

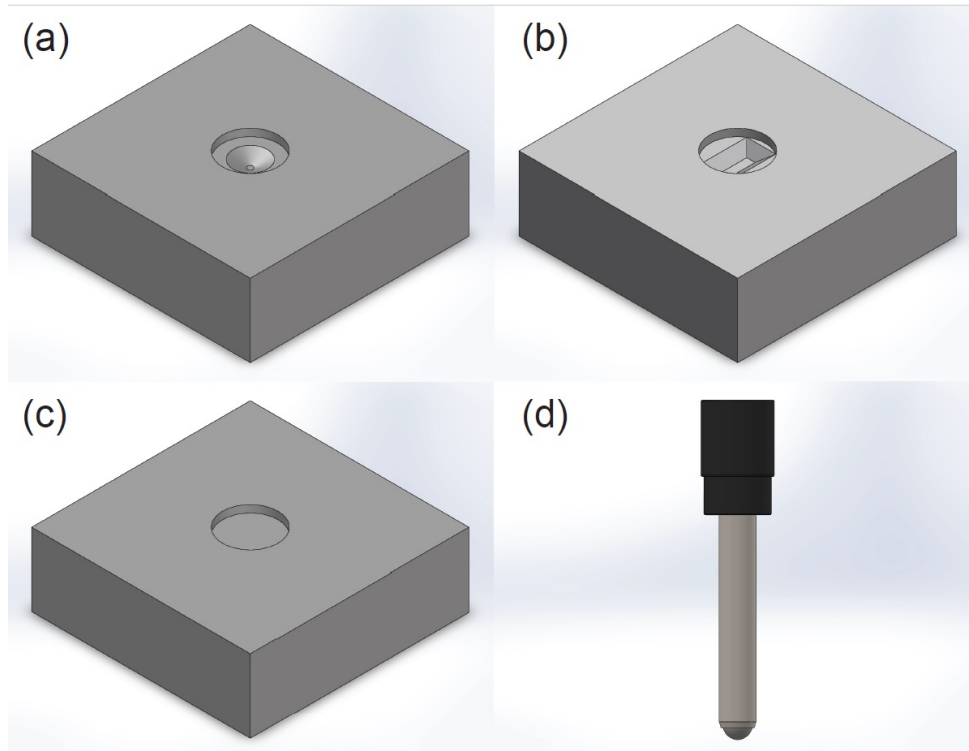


Figure 1.6: **Kinematic mounting surface feet** Illustrations of the 3 different necessary mounting holes which limit all degrees of freedom for the kinematic mount surface.

bottom surface below the threads as shown in fig. 1.6(d). The hemisphere aligns with a hole of a particular geometry which serves to limit certain degrees of freedom dependent on the geometry of the hole. Three different hole geometries were used to limit all 6 degrees of freedom. The first hole geometry as seen fig. 1.6(a) is cone-shaped. When the hemisphere is seated in this hole, it limits all translational degrees of freedom. The second hole geometry as seen in fig. 1.6(b), called a “v-groove”, limits one rotational degree of freedom on its own (either pitch or roll). When coupled with the cone shape, the v-groove limits a second rotational degree of freedom, the yaw of the system. The final hole geometry is a flat plate as seen in fig. 1.6(c). When coupled with the other two feet types, it limits the last rotational degree of freedom. Since a square surface was used, a fourth foot was added

and used a redundant flat foot geometry. All four feet were rigidly connected to the ground and the leveling screws were adjusted to ensure the surface normal was parallel with the gravitational vector. For this particular instantiation, we used aluminum for the "feet". All the feet were designed and machined in our lab. For the flat surface, we used a 60×60 cm² aluminum plate. The screws, (Thorlabs; Newton, NJ), were 1/4x80 steel mounting screws. The threading allowed for fine control, 0.3175 mm/rev. The platform was leveled to $< 0.1^\circ$, measured at various points along the plate.

1.4 Biological active granular matter

In this section, we discuss how ants distribute their workload to ensure the high-efficiency tunnel excavation, particularly during the incipient tunnel phase. We introduce the motivation for the study, describe the biological system, and finally discuss the theory behind the simulation used in the study.

1.4.1 Introduction

In the animal kingdom, there are many species which collect, swarm or flock together, such groups can be classified as active materials. In many of those cases, cooperation between animals in the group is imperative for the success and longevity of the assemblage, as the grouping behavior can be necessary for performing tasks. A great deal of attention has been focused on the "bottom-up" approach to studying such systems, for example, the different rules leading to the swarming behavior itself [57, 58, 59, 60]. Comparatively less attention has been paid to the "top-down" approach, or how to direct an active material to perform tasks or behaviors [61, 62].

In chapter 6, we show how fire ant, *Solenopsis invicta* fig. 1.13, colonies actively modulate the distribution of ants working to improve their tunnel excavation efficacy. This study was originally motivated by previous experiments from our lab [15] where a major discrepancy was observed between the number of worker ants working and the total number of ant

workers in the colony. In fig. 1.11 a snapshot from one such observation is shown.

In prior experiments, colonies of *S. Invicta* frequently had only a small percentage of ants working. The workers not engaged in the excavation were observed to be milling about, such that their activity had no clear connection to the excavation process. From videos and single snapshots in time, we knew the workload distribution was extremely unequal. This motivated further experiments tracking workload distribution evolution over time. We hypothesized that the distribution may become equal when taking into account data spanning many hours or even days.

1.4.2 Model organism: the fire ant

The *Solenopsis invicta* Buren, despite their size, fig. 1.12(a), are robust given the extent of areas they inhabit fig. 1.12(b), and are phenomenal architects fig. 1.12(c). Originally from the Pantanal wetlands of Argentina and Brazil[65], they are an invasive species in the Southern United States. Fire ants are the most well studied of all the various ant species [66]. The social structure or hierarchy of fire ants consists of a queen, male drones, and sterile females. The queens are responsible for reproduction, males responsible for reproduction and mating with the queens on a nuptial flight, and sterile females for performing the excavation work in the colony. The workers, the population which we will be focusing on in this dissertation, range in size from 2-6mm in length (3.5mm average), and have a head-width ranging from 0.4-1.2 mm (0.6 mm average) [67]. The workers can move at speeds greater than $9 L/s$ where L is a body-length [68]. The workers tend to live for around six weeks and queens for around three years [65].

1.5 Organization of the thesis

1. In chapter 2, a scallop-like like robot is used to probe into the question of reversibility for swimmers in granular media.
2. In chapter 3, we introduce the first smarticle system. Here prove the effectiveness of

geometric mechanics to explain hybrid dynamical systems.

3. In chapter 4, we examine a system where shape modulation in individually immotile robots creates a controllable “robot made of robots”. This chapter is based on [69, 47].
4. In chapter 5, we examine a smarticle system capable of modulating its material properties in response to an external stimulus.
5. In chapter 6, ant excavation is studied via a cellular automata (CA) model to determine the optimal workload distribution for excavation in fire ant populations. This chapter is based on [16]

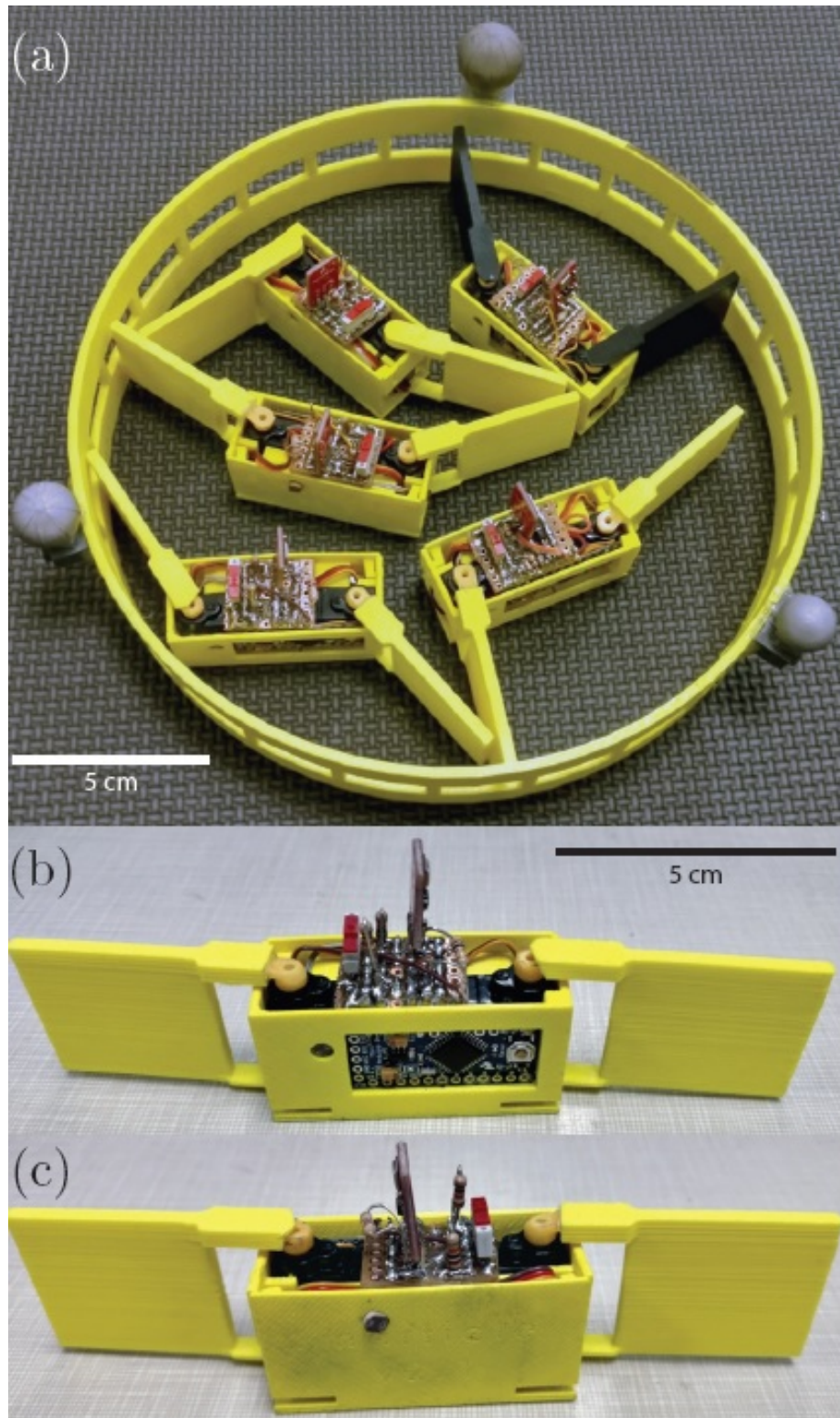


Figure 1.7: **Supersmarticle, and single smarticle front and back views** (a) Supersmarticle with 5 smarticles inside the ring (b) front-view of a single smarticle (c) rear-view of a single smarticle

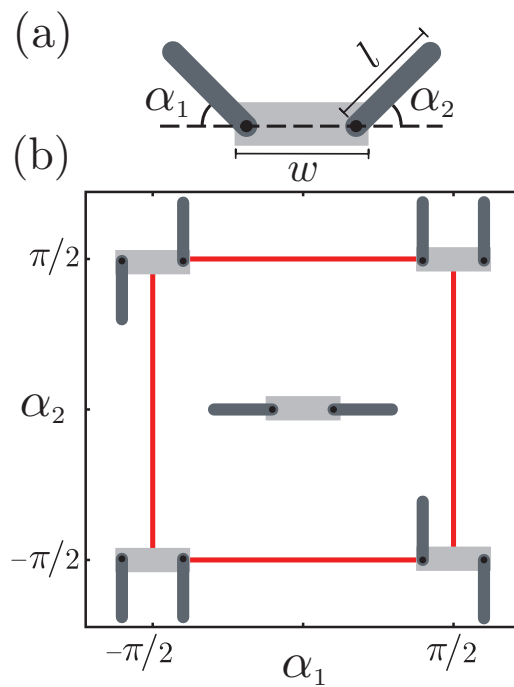


Figure 1.8: **Smarticle coordinate system** (a) Configuration space of a single smarticle defined by the angles α_1 and α_2 between the outer and inner links. (b) The square gait with certain configurations from the trajectory illustrated.

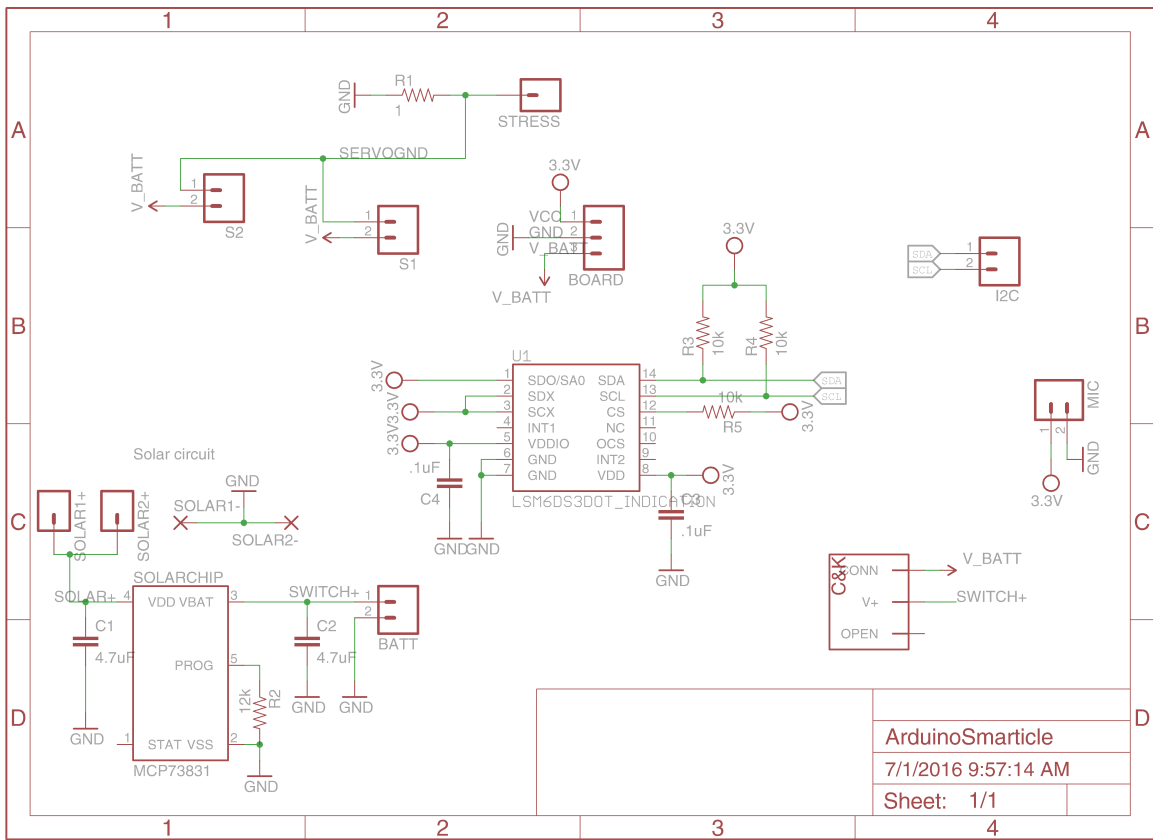


Figure 1.9: Circuit diagram for smarticle.

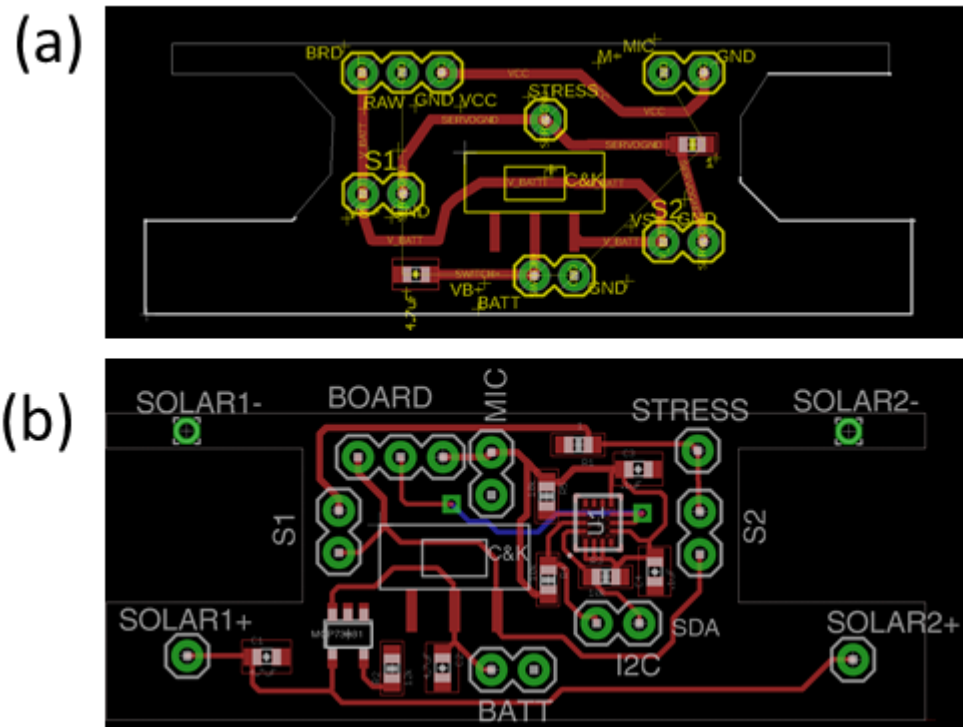


Figure 1.10: **smarticle PCB layouts** (a) Smarticle PCB design used for the smarticles we used in experiments for chapters 3 to 5. (b) layout for our most advanced working smarticle. This version included a 6-axis gyro, solar panels, microphone, stress sensing, and photosensing.

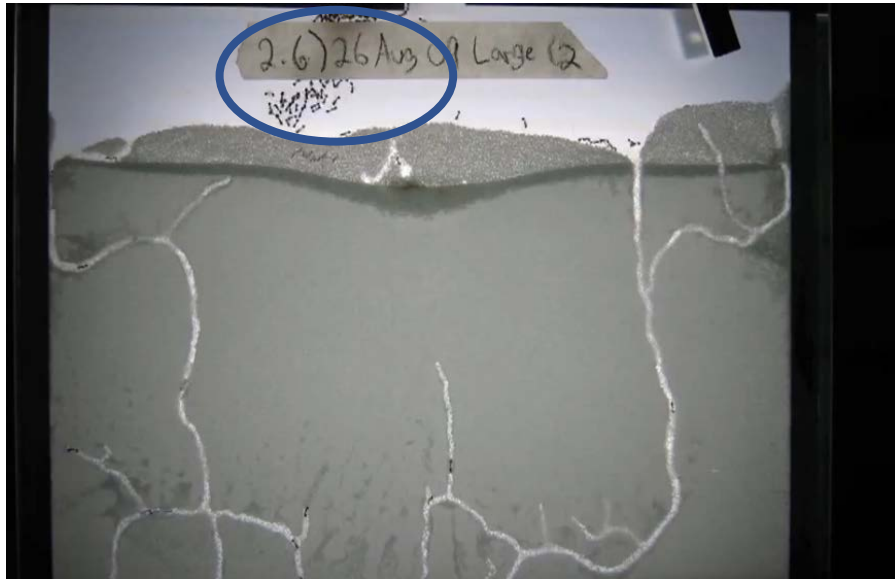


Figure 1.11: **Unequal workload in seen in quasi-2D ant experiment** Snapshot taken from videos of “ant farm” nest excavation by a group of fire ants. The particles used were 0.25 mm diameter wetted glass particles (15% water by mass) in a quasi-2D 24x31x0.3 cm³ arena. Taken from supplemental materials from [15]. At a given time-step the majority of the ant colony stays above ground (see blue circle): only a small percent of the ants excavate at any given time.

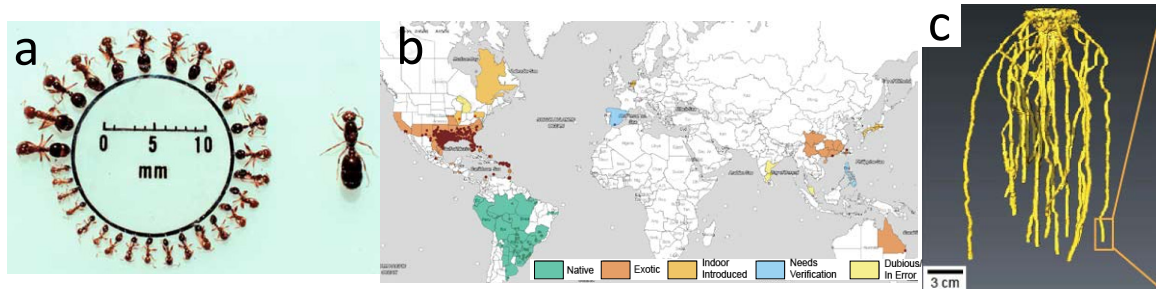


Figure 1.12: **Size, location, and nest information of fire ants** (a) Worker size range of the red imported fire ant, *Solenopsis invicta* Buren. Photograph by Sanford D. Porter, USDA, Gainesville, FL. (b) Fire ant habitats around the world for [63, 64]. (c) X-ray reconstruction of fire ant excavation in a container filled with 240-270 μm glass beads, reproduced from [16].

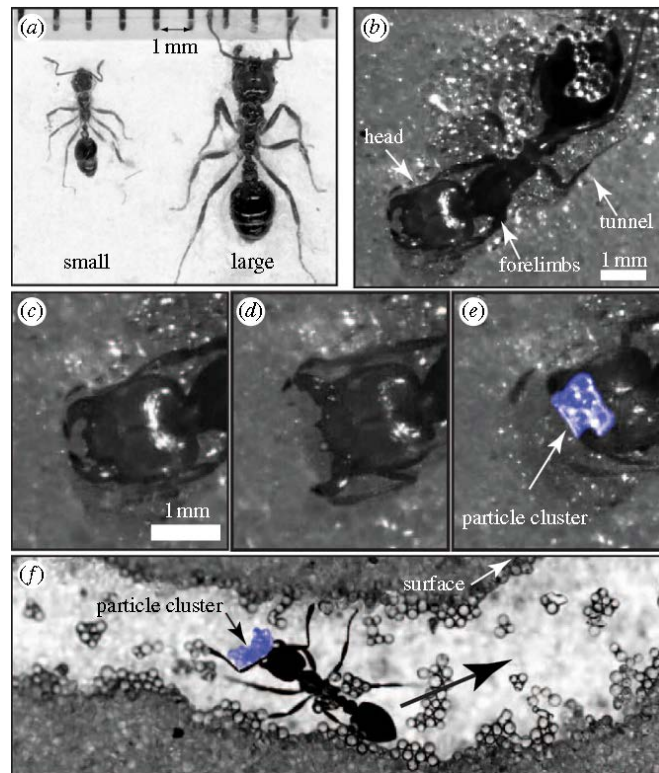


Figure 1.13: **Fire ant morphology** figure taken from [15]. *Solenopsis Invicta* workers digging tunnels. (a) Comparison of size difference between small and large workers. (b) Ventral view of a tunneling worker. (c,e) The mechanics of tunnel excavation involve loosening, carrying and transporting substrate (0.25 ± 0.04 mm diameter wetter glass particles) from the tunnel face to the surface. Excavated material is loosened and manipulated using the mandibles. (f) Excavated material is held in the mandibles and carried to the surface (direction designated by black arrow).

CHAPTER 2

REVERSIBILITY IN GRANULAR MATERIALS

2.1 Summary

In granular systems, swimmers undergoing reciprocal motion will have a displacement independent of initial ϕ , indicating asymptotic reversibility regardless of initial conditions. We study the locomotion of a non-inertial robotic swimmer, an analog to the Purcell 3-link scallop, in GM. Geometric mechanics predicts no net displacement for a 2-link system performing periodic gaits in GM, approximated as a frictional fluid. We test the validity of this theory with a 2-link robot. We see how depth in media, arm speed, as well as ϕ affects reversibility, a key requirement for geometric mechanics to work in two types of granular systems. In a GM of plastic spheres, we find that reversibility is affected by burial depth, but we find no dependence on arm speed in the regime tested. In a granular system composed of poppy seeds, we find swimming is affected by ϕ for the initial strokes, and that displacement is always maximum, regardless of initial ϕ , for the first cycle. The distance displaced on the first cycle, as well as subsequent displacement between cycles, depends on the initial ϕ . Despite this, after a many cycles, displacement will asymptote towards the displacement made by a system with an initial ϕ equal to the critical volume fraction, $\phi = \phi_c$. $\phi(t = 0) < \phi_c$ systems, which are characterized by low initial stroke displacement, continue to translate further after the first stroke to reach the position reached by $\phi_c(t = t_f)$. Alternatively $\phi > \phi_c$ systems tend to lose displacement after their initial strokes to to reach the same position as $\phi_c(t = t_f)$. Final displacement is independent of the initial ϕ , indicating asymptotic reversibility regardless of initial conditions.

2.1.1 Introduction

Dry granular materials (GM) are collections of macroscopic particles (sizes typically larger than $100 \mu\text{m}$) which interact dissipatively through short-range contact forces such as friction. GM is a major field of study because of its abundance in nature and in industry: research of granular physics has shown to have both biological as well as engineering applications [70, 71]. GM can display a large range of possible behaviors: it can have aspects of solids, gases, and liquids [1]. GM can act like a solid by jamming and resisting shear [72], when externally driven through vibrations, it can act like a gas [73], and on a slope beyond the angle of repose, GM will flow like a fluid. In this chapter, we will focus on its fluid-like properties.

Like swimmers in low Reynolds number fluids, a GM swimmer can exhibit reversibility, however only under certain circumstances. Reversibility can depend on the grain shape, depth of the swimmer, and speed moved through the GM. Qualitatively, it is quite simple to illustrate irreversibility in GM: one only needs to imagine what happens when they move their hand back and forth atop a mound of sand on a beach. After a single period of movement, the state of the sand has been irreparably disturbed. The new state of the sand is a function of previous movements; subsequent swipes will be different because of interactions with tracks left from earlier hand movements.

For locomotion schemes utilizing periodic motion and which operating in GM, the success, measured by displacement, can depend heavily on the grain properties. For low friction and spherical grains, significantly less, or zero displacement may result from periodic motion as we will show. For different grains, however, we find that displacement is possible—for example in a bed of poppy seeds. We posit that difference lies in the frictional nature, and a-thermal aspects, of natural granular material. Natural granular materials are less mono-disperse; there are size differences between grains. Aside from the difference in sizes, the shapes tend to be may be non-symmetric, with jagged edges, giving rise to small concavities helping to increases particle friction. For systems with more natural type GM,

reversibility in locomotion is not as well documented. Furthermore, a large class of animals like turtles exhibit locomotion patterns similar to a 3-link type system [74], but they move on the surface rather than underneath the surface.

For these natural systems where a swimmer may not be completely buried, much of the physics is contained in the craters formed due to movement of the links or arms [70]. The shape of these craters and mounds which form is dependent on volume fraction ϕ [75]. Here we define $\phi = \frac{V_{grains}}{V_{total}}$, where V_{grains} is only volume of grains themselves and V_{total} is the volume which contains all the grains. In previous studies, when dragging an intruder through GM and measuring the drag, the force as a function of displacement behaves differently for high ϕ rather than for low ϕ [76], therefore the behavior of GM under shear heavily depends on ϕ . For loose grains, (low ϕ), GM will compact under shear, for tightly packed grains (high ϕ) GM will dilate under shear fig. 2.1. Interestingly, despite the initial value of ϕ after a certain shear distance, drag forces asymptote towards approximately the same value. ϕ locally begins to asymptote towards a singular value, known as the critical state (fig. 2.1) [77, 76] ϕ_c [78].

Despite some of the differences between granular and low Reynolds number swimming, there is a precedent of using geometric mechanics (section 1.2) to successfully describe motion in granular systems, despite this seeming disconnect with the reversibility requirement. There are a few ways to mitigate the GM effects which differentiate it from swimming in low Reynolds number fluids. One method is demonstrated by the way mudskippers and turtles locomote [21]. Both animals can be modeled with geometric mechanics: they lift their limbs above the material between steps; at each step the animal is not interacting with previously disturbed GM. Other studies [25] were able to prove the usefulness of geometric mechanics in a GM system where the grains were interacted with more than once—by the swimmer—by burying the robotic GM swimmer deep beneath the surface.

While geometric mechanics has had many successes, it is not yet clear if the framework can be applied to situations where the environment has time-dependencies or has hysteretic

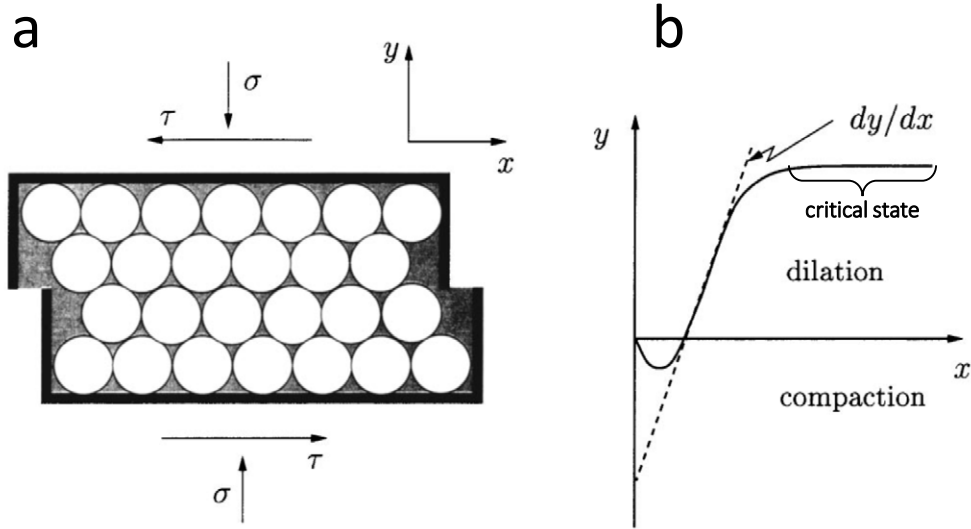


Figure 2.1: **Granular shearing leading to compaction, dilation, and the critical state.** (a) A box of granular materials being sheared and (b) how the height of the box varies with shear distance. For a box of initially loose grains, $\phi < \phi_c$, the grains will compact and the height of the box will decrease. When the system is more compacted $\phi > \phi_c$, the grains will compact, tightly packed grains will expand the box height, and once the critical state is reached, the box height should stay constant. Figure reproduced from [77] with critical state information added.

effects [79]. We are interested in the robustness of reversibility (and therefore geometric mechanics) for systems where the extent of reversibility may change as an experiment continues. It is the purpose of this study to probe into why, despite the technical incongruities, this theory still seems to work for certain granular systems.

Unlike in a previous study performed in our lab where granular flow resulting from unidirectional movement of plates through media[75] was examined, here we study specifically granular flow resulting from periodic motion. The key difference is how, after the first movement, all subsequent movements interact with previously plowed GM. Movement through an area of grains is dependent on the organization of the grains; the previous movement affects the grains current state and therefore the performance of the future cycles. In this experiment by varying number of strokes, stroke frequency, stroke amplitude, and wait time between strokes, we study reversibility or lack of it, in real GM. Furthermore, from this insight, we hope to better understand the strengths and limitations of using geometric

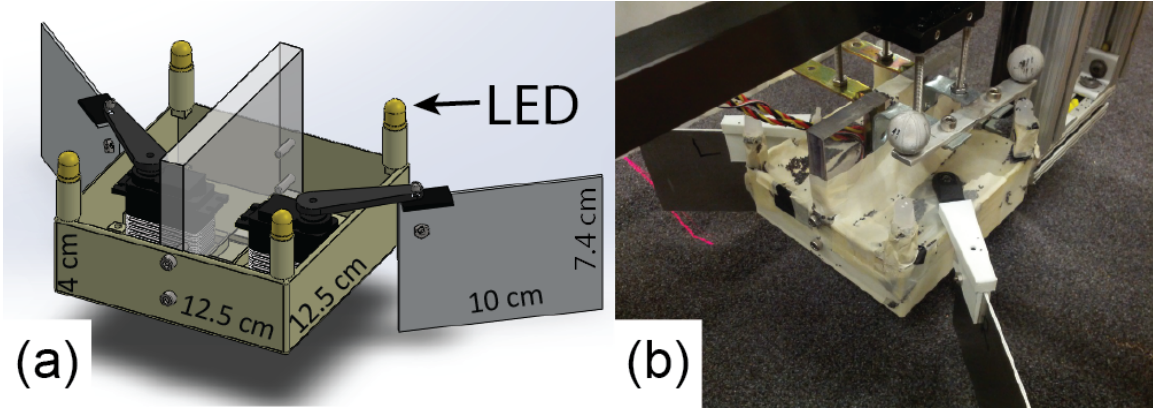


Figure 2.2: **Illustration and experimental version of scallop robot** (a). 3D rendered model of the scallop robot. (b) The robot in experiment.

mechanics with GM. To perform this study we will be using a biologically inspired, yet abstracted, robotic scallop to probe into the fundamental physics of the system.

2.2 Materials and methods

2.2.1 Robotic design

The two-link swimmer, or scallop robot, consisted of a 3D-printed square body ($12.5 \times 12.5 \times 4$ cm) which housed two HS-M7990th (Hitec; Poway, Ca.) servos connected to two aluminum rectangular flaps. In fig. 2.2 the robot is shown in both a 3D model (a) as well as in the actual experiment (b). The flaps move simultaneously, such that, despite technically being a 3-link system, it acts as a 2-link system.

The servos are controlled via LabVIEW, which communicates with the servos via a Lynxmotion SSC-32 servo controller (Lynxmotion; Swanton, VT). The robot is constrained to move in a single axis (see fig. 2.3(a-b)). Two vertically oriented linear roller bearings constrain the vertical linear degree of freedom, and a square horizontally oriented linear air bearing eliminates the rotational degrees of freedom (pitch, roll, and yaw), as well as one other linear degree of freedom. The vertical position of the robot is controlled by two linear actuator motors (Firgelli; Victoria, BC, Canada) connected to the horizontally oriented linear air bearing. Both LEDs and IR markers were used in tracking the robot. The

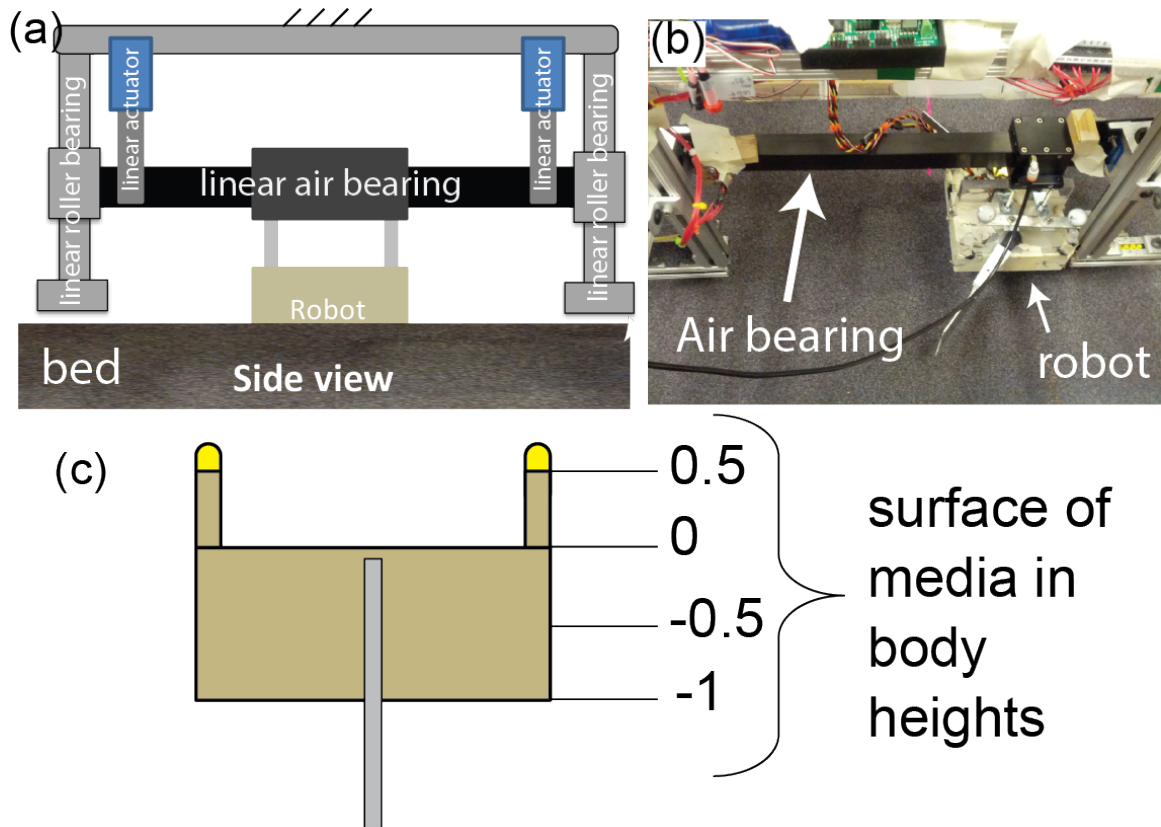


Figure 2.3: **Experimental setup schematic** (a). Cartoon side view of system showing the locations of the various bearings which limit movement to a single degree of freedom. (b) Experimental picture from above. (c) Schematic detailing different burial depths related to body height

LEDs were tracked using a digital camera (Point-Grey; Richmond, BC, Canada) and the IR markers could be tracked using OptiTrack(NaturalPoint; Corvallis, OR). All systems, both actuation and data collection, were controlled via LabVIEW. In the plastic particle system, described in detail below, the camera recorded the positions of the four LEDs, the average of which was used to determine the displacement of the robot.

2.2.2 Plastic particle system

Our first few tests determined the transition to reversibility in a bed of 6 mm ABS plastic particles. These particles have been used frequently in our lab in the past since, due to their uniformity and spherical shape, these particles can be simulated more easily [39, 25].

Experiments were performed where the displacement of the robot, undergoing periodic motion, was measured at varying depths inside the media. Since the outer flaps extended below the body of the robot, tests could be performed at various heights: from a height where only flaps touched the grains, up to the lights posts used for tracking of the robot body fig. 2.3(c). Each run began with the robot being lifted above the media while the granular “state” was reset: all mounds and tracks from previous experiments were hand-smoothed between trials. The linear actuators ensured the robot was inserted into the media to the desired depth fig. 2.3(c). Once placed in the material, the robot would perform n number of strokes (see fig. 2.4) or $n/2$ cycles where a cycle is defined as two strokes. For the experiments detailed in this chapter in the plastic particle system, we performed $n = 30$ strokes. The flaps would start -40° from the mid-line of the robot and stroke forward 80° , then backward 80° . Between each stroke, the robot would remain still for a single second to allow any particle movement to settle before performing the next stroke. After all strokes were completed, the robot was lifted above the media, the tracks erased, and the robot placed in its starting position.

In the plastic particle system, we did not have precise control over the volume fraction of the material. Furthermore, the low friction, coupled with spherical particles, tended to keep the particles at a higher compaction. In the plastic particle system, we performed experiments where we varied depth of intrusion and angular speed of the arm flaps.

2.2.3 Poppy seed system

To study how compaction played a role in the movement of the scallop robot, robot swam in a bed containing poppy seeds with diameter $D \approx 1$ mm—compared to the aforementioned plastics particles. Poppy seeds were chosen for this experiment due to their high frictional nature, arising from their surface roughness, which can be seen when viewed up close [80]. The surface roughness is one reason why poppy seeds are capable of achieving a higher range of possible packing fractions $\phi \approx [0.58 - 0.63]$. Aside from the ϕ benefit, poppy

seeds have another benefit as a model granular system for robots: beach sand is extremely hard and can damage motors if caught between gears, whereas poppy seeds will harmlessly grind away. Another side effect of the frictional nature and density of the poppy seeds is that we cannot bury the robot as deep as in the plastic spheres experiments. The material is too compact and dense for the servos to operate without damaging the servos.

Unlike in the plastic particle system, the poppy seeds can be fluidized via a fluidized bed built by Chen Li et al. [71]. In the air-fluidized bed, the air was blown up through the poppy seeds from below via an array of three air blowers below the bed. The bottom of the bed is made of a porous material, called a distributor plate, which distributes the airflow evenly across the bed. When the air which passed through the porous material provides enough force to lift the grains, the media is considered fluidized. Fluidization allows the tracks from previous experiments to be erased, resetting the system state.

Once the surface of the media was fluidized to the point where the surface tracks were erased, the air flow was decreased to a bubbling state [81]. A bubbling state is characterized by airflow velocity just below fluidization. This amount of airflow allows the robot to be easily intruded into the media ($H = 0.25$). During the bubbling state, intrusion of the robot required an order of magnitude less force to insert it to the desired depth. After intruding to the correct depth, the airflow is halted. The height of the poppies in the bed was read from a camera from a separate location on the bed. Using a previously calibrated scale, ϕ was calculated from the bed height. With ϕ recorded, the robot would begin its movement program, the same as was performed in the plastic particle system. In the poppy system, the strokes were performed at $f = 30^\circ/\text{s}$ and for $n = 50$ strokes.

To increase the range of accessible ϕ , we varied the fluidization procedure depending on the desired compaction state [82, 76]. To generate a low ϕ state, the airflow was lowered to the bubbling phase, and was slowly decreased until airflow ceased. To create a high ϕ state, a combination of both pulsing of air and a vibrating motor to shake the bed was used after the fluidization had ended. With the fluidization of the media possible, the only step

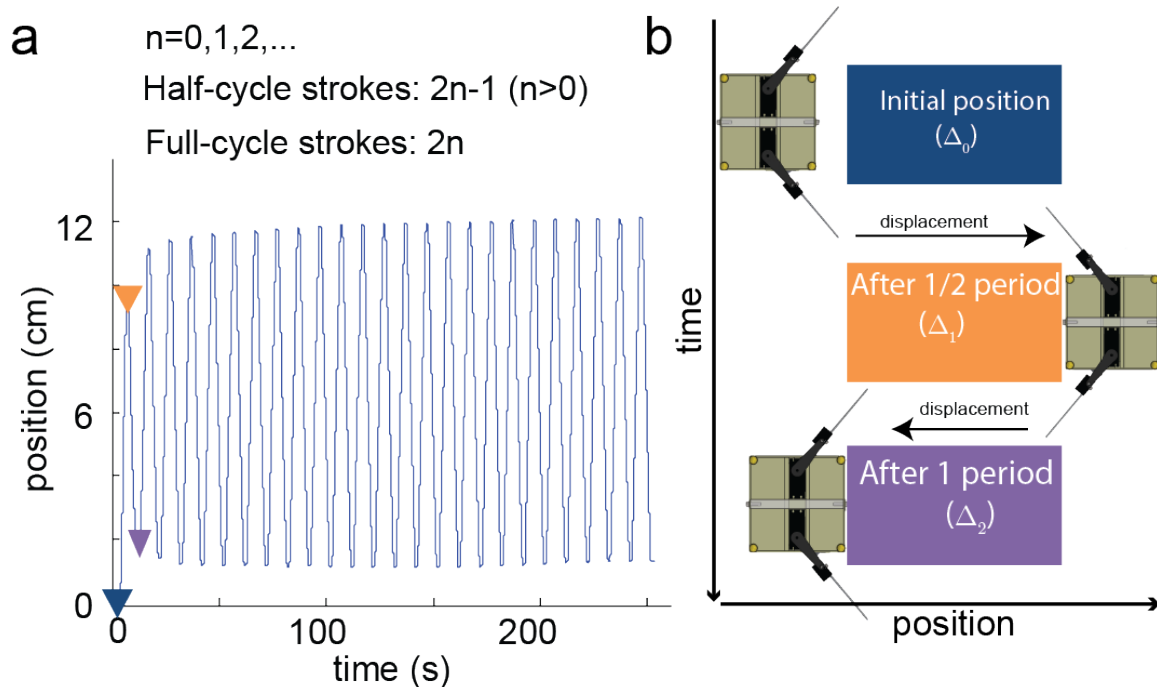


Figure 2.4: **Scallop robot experiment procedure definition** (a) Example of raw data showing position as a function of time. Blue, orange, and purple markers are shown at the first three peaks and are diagrammed in (b). This example trial was taken in in poppy seeds at $f = 30^\circ/s$ for 50 strokes. (b) Diagrams of what the robot looks like, and direction of displacement, at the points specified in (a). Here we define the position variable Δ_n , where n designates stroke number

performed by hand in the plastic particle system, hand-smoothing the tracks, could now be automated. As a result, the entire system was made to be completely autonomous. The position of the robot was determined by taking the average position of two IR markers shown in fig. 2.2(b).

2.2.4 Illustrative example data

An example of raw data taken from a poppy seed experiment is shown in fig. 2.4(a). Here we show position as a function of time. The markers in (a) are colored to correspond to the different colored diagrams in (b) which delineate certain positions with a naming convention appearing in fig. 2.4(b).

To illustrate reversibility more concretely, we show two experimental trials seen in fig. 2.5(a-

b). Here the robot was placed at $H = 0.34$ body depths and was allowed to flap back and forth at $f = 50^\circ/\text{s}$. On the forward stroke, the limbs would propel particles behind the system and the front of the robot would plow the particles ahead of it. On the backstroke, the particles encountered will have been affected by the plowing action of the front of the robot. This qualitative picture explains the different forms for the displacement on the forward and backward strokes—seen by the guiding dashed line in fig. 2.5(a). After 30 flaps, the experiment in fig. 2.5(a) shows a nearly reversible system. Another trial was run directly afterward without disturbing the system, and (a) clearly shows nearly zero displacements made on either the front or backstrokes for the entire second run.

Another experiment was performed which demonstrated how the holes dug out of the media are closely related to the reversibility. Holes form in granular systems since GM can flow only with a non-zero yield-stress: unless the sides of the pile are angled greater than the angle of repose, an undisturbed pile will not flow. In fig. 2.5(b) we perform a run the same procedure mentioned in the previous paragraph, however on the subsequent run, we fill in the holes made by the flapping in the previous trial seen in fig. 2.5(c). The reversibility is clearly affected by the first stroke. Interestingly, the system asymptotes far quicker than on the first run. With this example, we have demonstrated how different depths could affect reversibility: different depths can generate different tracks.

2.3 Results and discussion

2.3.1 Reversibility as a function of depth in media

In our previous study where we tested geometric mechanics in the same plastic particles[25], the robot was completely submerged in the particles. As a result, irreversibility due to mound effects was not an issue. The yield-stress necessary to have grains flow in and fill any craters was generated by the weight of the particles on top of displaced particles below the surface. The primary focus of the robot in the plastic particles is to examine the transition between irreversible to reversible behavior by varying burial height and arm

speed.

For this experiment, we start with the hypothesis that a more deeply buried robot should behave in a more reversible manner. The “history” of previous strokes, the tracks left, should be less prominent for trials more deeply buried. Any plowed particles would be more readily replaced by other particles. The hypothesis does not hold seem to hold for the forward-strokes fig. 2.6(a), at least at the burial depths measured here. While it does not follow our hypothesis, we do see a trend: the deeper the robot is buried, the farther the robot displaces. Moreover, at a certain burial depth, the robot actually goes backward. It is important to note the scales however, after 30 strokes, even the farthest displacements only amounted to 0.5 cm, which is only 4% of the body size. Coupling this negative displacement with the positive displacement on the back-stroke we see the robot’s range traveled increases upon increasing cycles(a-b).

Since the robot performs a reciprocal gait, we should expect the displacement after full cycles, fig. 2.6(b), to be lower as the robot’s depth increases. Indeed, the larger depths tend to produce the least amount of displacement for a given number of strokes. For all burial depths, the asymptotic behavior after the backward stroke indicates the robot will eventually cease any forward displacement, representing reversibility. The robotic system, regardless of burial height, seems to make very little displacement in the plastic particle system. When measured by its full cycle strokes, the system follows our hypothesis regarding burial height and reversibility.

2.3.2 Reversibility as a function of frequency

To determine if the reversibility was affected by the angular speed of arms, we varied the arm speed $f = [30^\circ/\text{s}-50^\circ/\text{s}]$. The results are shown in fig. 2.7 (a-b). While the speed of the arms does seem to affect the final displacement of forward (a) and backward strokes (b), the relationship between the two is unclear. At all speeds, the functional form of the curves looks similar. While three trials were performed, the difference between curves seems quite

small: for the speeds measured, we conclude that gait speed does not play a major role in the displacement as long and the particles do not become inertial. This result aligns with what geometric mechanics predicts about low Reynolds number swimmers as well.

2.3.3 Reversibility as a function of volume fraction

Since the flow of GM has strong dependencies on ϕ , we examine here how reversibility may be varied by changing compaction. If we look at the example in fig. 2.4(a) we can see that the first few strokes are the most interesting. After the first six strokes, the distance traveled becomes negligible: $> 90\%$ of final translation is achieved, (92% of final peak translation and 99% of final valley displacement). Furthermore, while the robot is moving in a natural GM, and despite it not being intruded all the way in the media, it still does indeed become asymptotically reversible. However, it does not return as close to its initial position compared to the experiments performed in the plastic particles. The displacement made on the first few strokes remains, or said differently, the irreversibility caused by the first stroke is preserved. In fig. 2.4(a), we only see information plotted for a single value of ϕ . To get more information about how ϕ affects position we need to plot the same plot but for multiple values of ϕ , as in fig. 2.8.

We can immediately see similarities in all runs independent of ϕ . Firstly, the change in position is greatest always for the initial stroke. Furthermore, all curves approach a universal curve, in other words, reversibility occurs independently of ϕ . The variance in position decreases as stroke or cycle number fig. 2.9 increases. Here we can see more clearly how displacement varies with ϕ . Despite the initial granular ϕ state, at later strokes all runs tend to approach the distance traveled at $\phi = \phi_c \approx 0.6$, shown in black in fig. 2.9(c-d).

Looking more closely at the first 6 strokes in section 2.3.3, the effect of ϕ becomes more obvious. For high volume fractions, the slope representing a change in position for low ϕ is negative, indicating that after the first stroke, displacement is lost for loose media.

For more compact media, further displacement is made after the first stroke. The slope of zero represents zero displacements or reversibility, a feature that we have shown all other compactations asymptote to eventually. By plotting the half-cycle and full-cycle displacements as a function of ϕ (fig. 2.11) the crossover point, representing reversibility, happens near the critical state ϕ_c

2.4 Conclusion

For the plastic particle system, the results indicated burial depth does seem to affect volume fraction, as hypothesized. Furthermore, as geometric mechanics predicted, there was not a large enough effect to conclude that the frequency of arm movement affected displacement in any real way.

For future experiments, we believe reversibility could perhaps be reached faster with a different geometry for the robot body. The forward facing cross-section of the robot in this study was quite large. For the three-link robot in [25], the perpendicular cross-section with respect to the grains was on the order of the grain size. This meant particles could flow around it quite easily and rather than being dragged for large distances as in the experiment. Furthermore, due to the frictional nature of granular materials, piles, and valleys tended to form in front of, and in the wake of, the robot. Each stroke would interact with a granular structure whose shape depended on the previous strokes. We would recommend a robot with a geometry not quite as wide in the direction of the travel. Furthermore, we recommend a robot which can be buried even deeper than the one shown here, such that no mound or valleys form. In this experiment, the torque on the arms, a consequence of both the weight of the plastic particles and the arm length, was too great to bury the system any deeper without damaging the servos.

For the poppy seed system, we found that even in GM where a larger range of accessible ϕ is available, the system still behaves reversibly. Reversibility happens after multiple strokes, and the way in which reversibility is reached varies with ϕ . We posit that the rea-

son why reversibility eventually happens regardless of initial packing fraction is explained by the critical packing fraction phenomenon whereupon continuous shearing all granular material will reach its $\phi = \phi_c$.

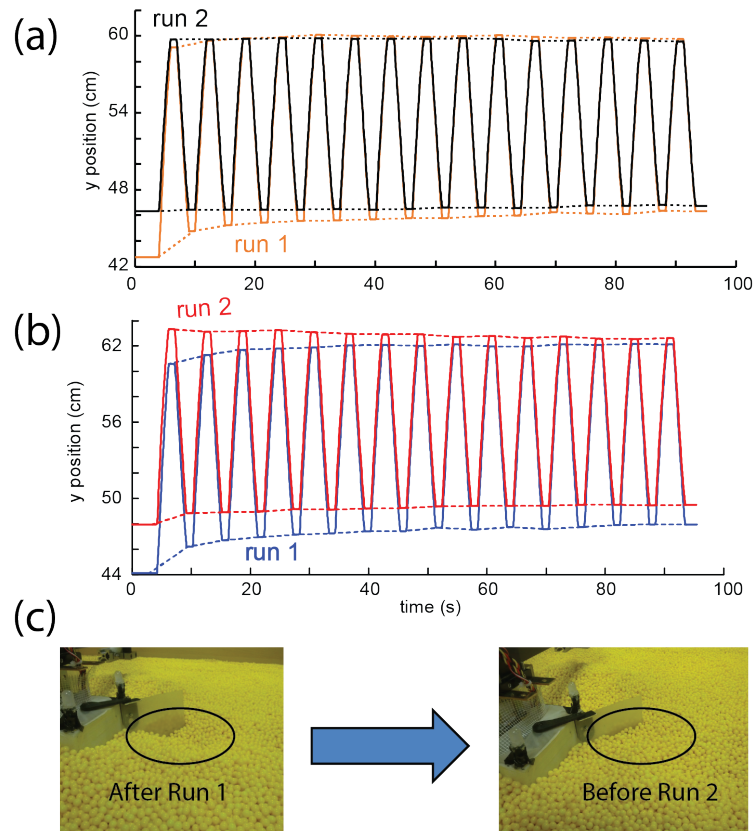


Figure 2.5: **Eliminating established reversibility** (a) and (b) represent two runs where the reversibility can be attained after many strokes. After the end of the first run, run 2 is started without disturbing the system. The system behaves reversibly for the entire run. In (b), before run 2 is started, the holes created by run 1 were filled in (c). Although reversibility is destroyed initially in (b), after the first stroke, the reversibility is re-established for both experiments (a) and (b) on run 2. In (a) and (b) the solid lines represent the displacement and the dashed lines are meant to help guide the eye.

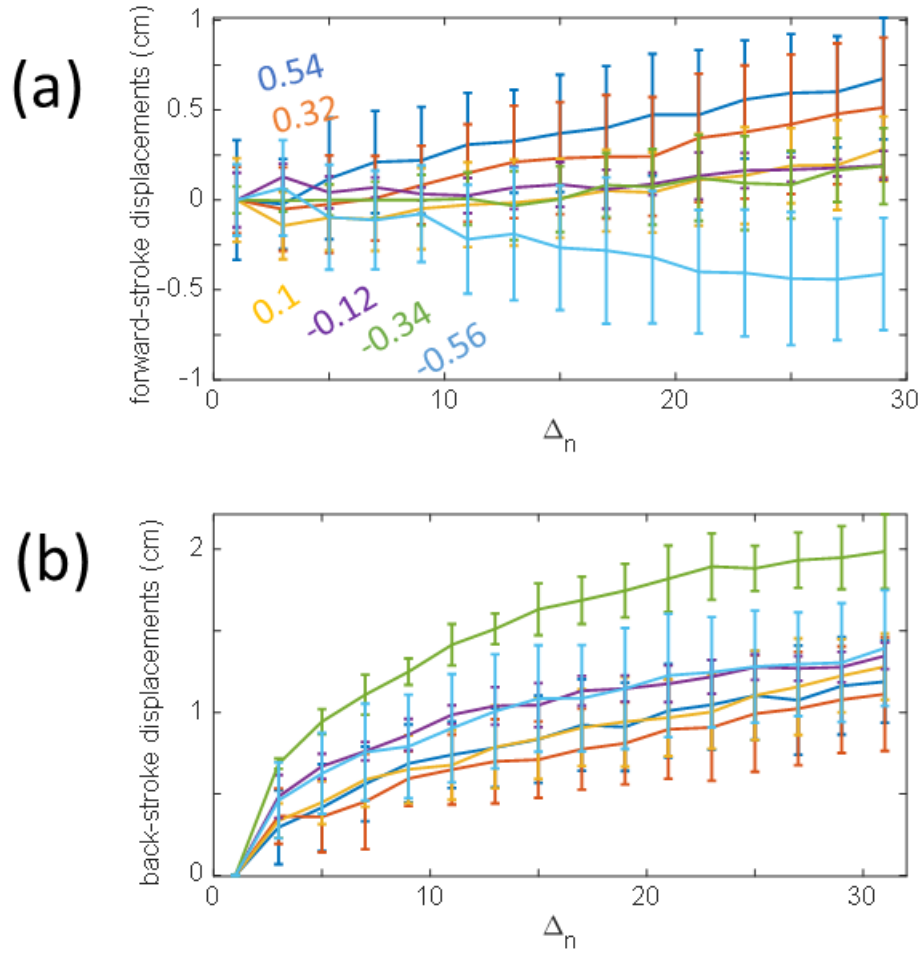


Figure 2.6: **Forward and backward stroke displacements in plastic particles** Displacement of robot in the forward strokes (a) and backward strokes (b) for many $n = 30$ stroke experiments. Each line represents a mean of 5 trials each.

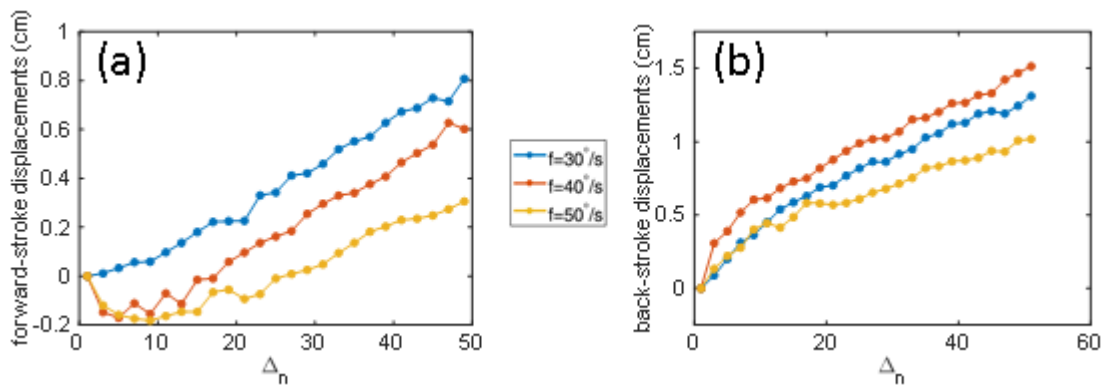


Figure 2.7: **Effect of stroke angular speed** Forward (a) and backward (b) stroke displacement as a function of stroke number for three different speeds. The lines are the mean of three trials

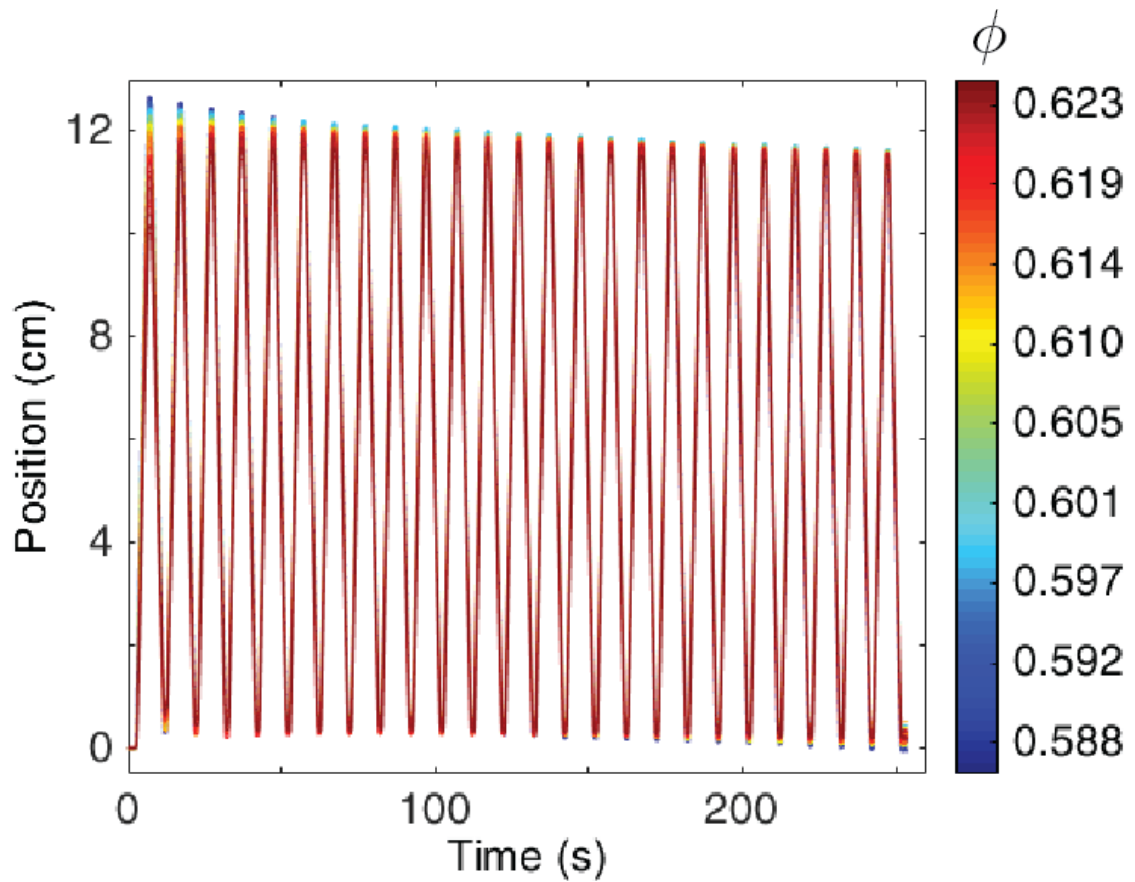


Figure 2.8: **Position as a function of time at various compactions** Many $n = 50$ stroke trials for different values of ϕ in poppy seeds. Variance in position decreases as stroke number increases.

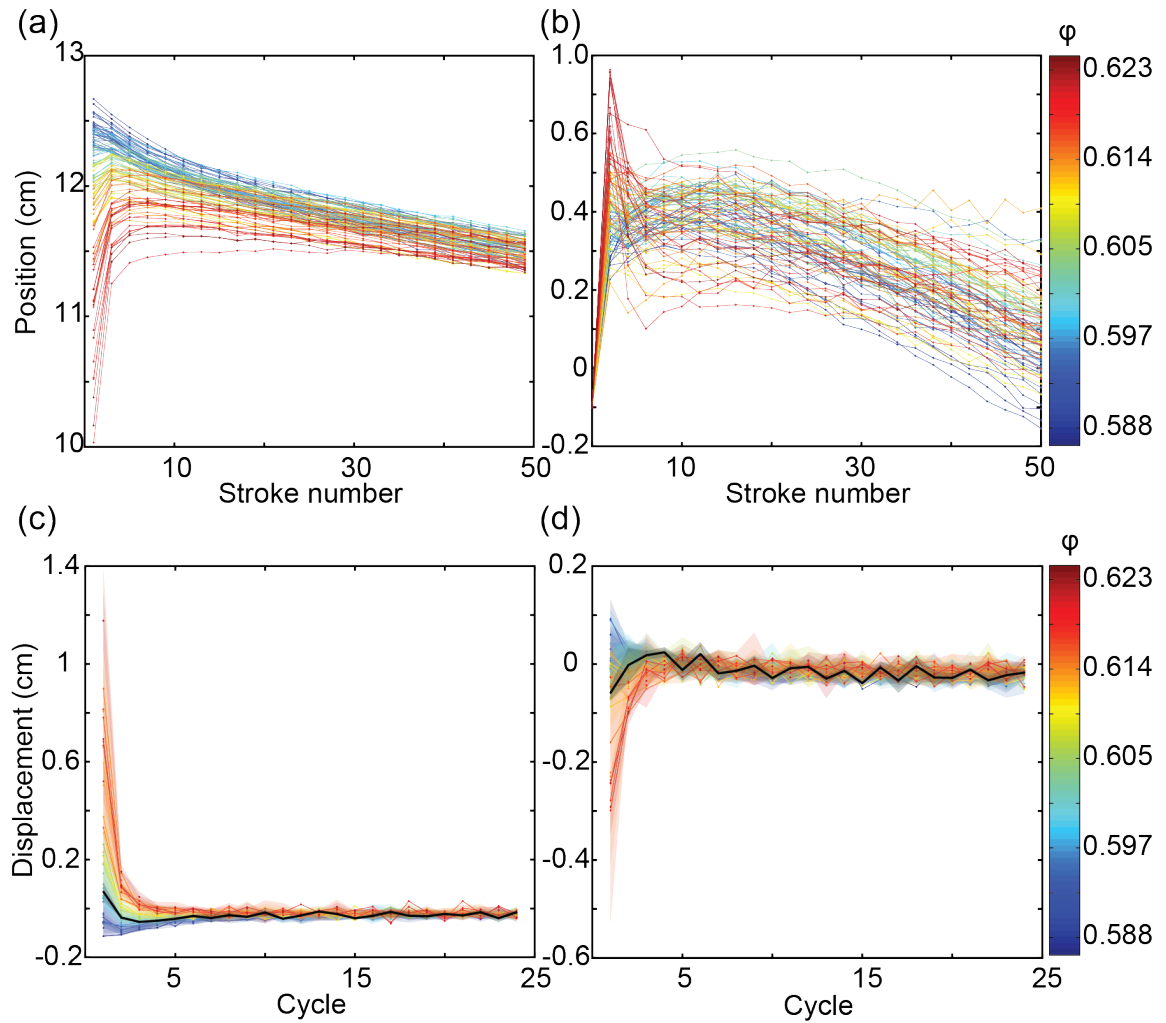


Figure 2.9: **Displacement as a function of cycles for various ϕ** Distance versus time data for $n = 50$ stroke runs at half-cycle strokes (a) and full-cycle strokes (b) in the poppy seed system. The ϕ of a run is indicated by line color indicated by the colorbar on the right for both plots. (c) and (d) show the same data as in (a) and (b) but as a function of the half (c) and full(d) cycles instead. The black line highlights the trial at the critical volume fraction $\phi(t = 0) = \phi_c$. Here a cycle is two strokes

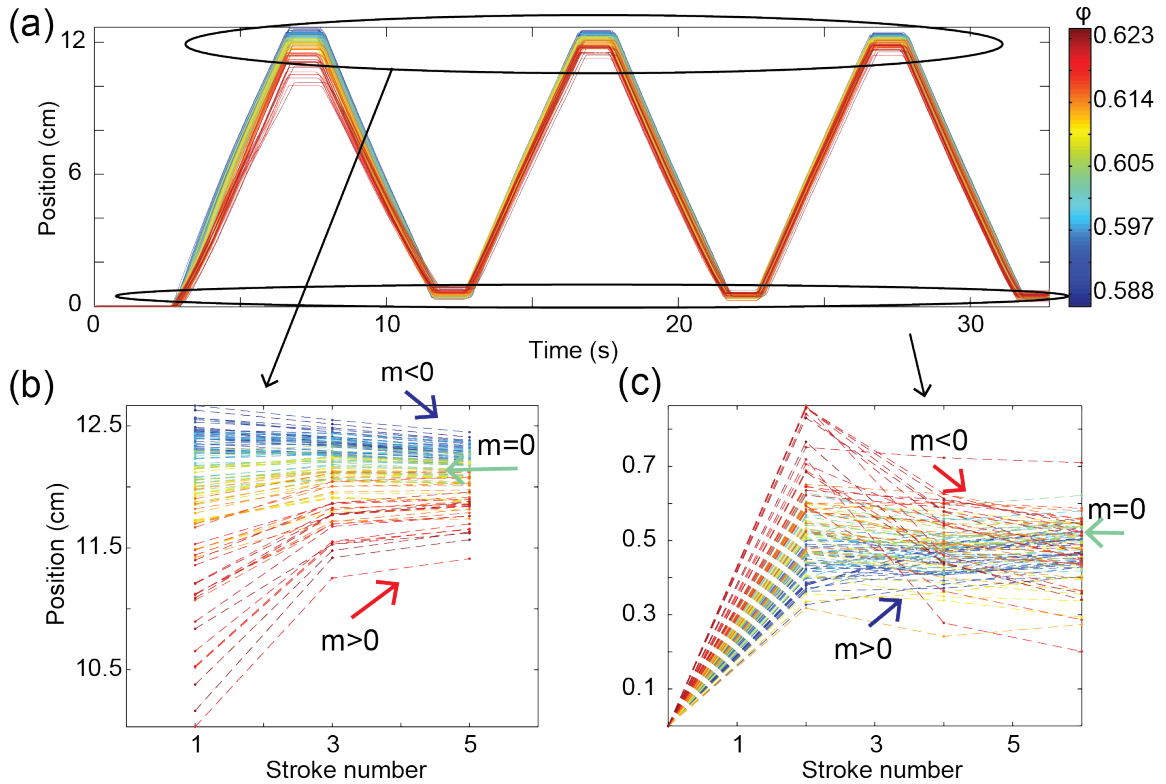


Figure 2.10: **Scallop position after 6 strokes at varied ϕ** Multiple 50 stroke runs, cut off at stroke six to emphasize initial stroke behaviors. (a) The majority of the convergence towards reversibility happens in the initial few strokes. (b) Positions of the robot after half-cycle strokes. $\phi(t = 0) < \phi_c$ make a larger initial displacement and lose distance on subsequent strokes, converging towards the distance made for $\phi(t = 0) = \phi_c$. Similarly, for $\phi(t = 0) > \phi_c$, lower initial displacement is made, but it continues to increase at subsequent half-cycle strokes. We see the same convergent behavior but with reverse slopes for the back or full-cycle stroke positions in (c). Position as a function of stroke number for full-cycle stroke. Trials with $\phi(t = 0) > \phi_c$ tend to lose position achieved by the initial full-cycle stroke stroke, whereas trials where $\phi(t = 0) < \phi_c$ steadily displace forward. In both (b) and (c), m refers to the slope of the ϕ with color matching the arrow used. Colors in all plots reference the trial's $\phi(t = 0)$

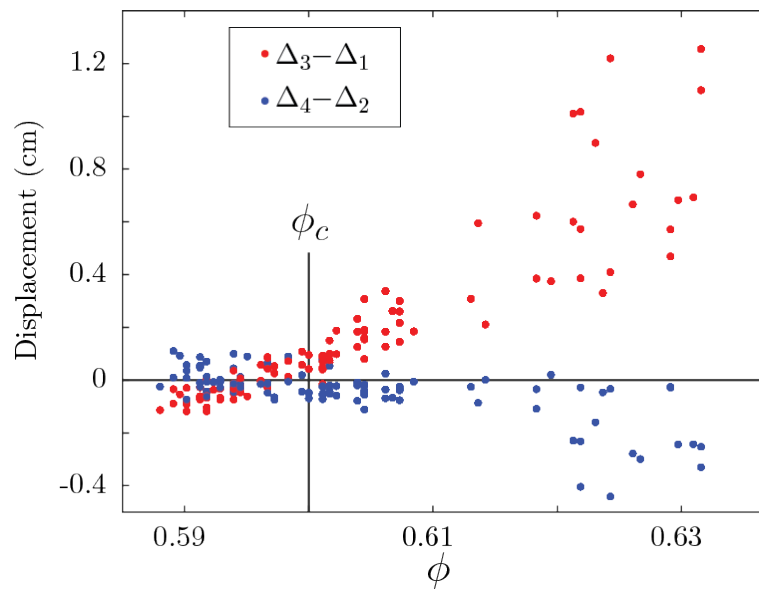


Figure 2.11: **Displacement versus ϕ for the second full cycle and first half cycle** Red represents half-cycles and blue represents the full cycles from various runs. The crossover between the red and blue happen at the approximate value of the critical volume fraction $\phi_c \approx 0.6$.

CHAPTER 3

APPLYING GEOMETRIC MECHANICS TO THE HYBRID DYNAMICAL SMARTICLE CRAWLER

3.1 Summary

A three-link robot can translate along a surface by performing a gait, or a periodic sequencing of its links. Different gaits will have different translational efficiency. A three-link crawler is a hybrid-dynamical system that contains both discrete and continuous dynamic behaviors; such systems can be difficult to study because frequently analytical solutions cannot be found. As a result, optimization for such systems can be difficult or impossible. In this study, we apply a theoretical framework, known as geometric mechanics, to this system. To test its efficacy we start by examining how arm length l to barb width w affects movement speed for two specific gaits. The two gaits we studied were a square and diamond gait (named for the shape they trace in the 2D configuration space). We find that aspect ratio does not affect all gaits the same via results from an automated smarticle crawling experiment. For the square gait, l/w improves performance for small gait sizes (where gait size is defined by the degrees from the origin to an edge, or vertex, for a centered gait shape) but decreases performance for larger ones. Furthermore, the diamond gait was unaffected by changing l/w . Next, for a constant l/w , we use geometric mechanics to explain the functional form of the results we found for the crawling speed as a function of gait size. To our knowledge, this is the first application of geometric mechanics to a hybrid-dynamical system.

3.2 Introduction

A great deal of interest in three-link systems followed Purcell's "Life at low Reynolds number" [17]. Many of the works on three-links, however, examine the three-link system as a swimmer [24, 83, 84, 85], or, such systems are examined only theoretically [86, 87]. Here we wish to study closely a three-link crawling system on hard ground moving such that contacts with the ground are created and broken. This is a hybrid-dynamical system, there are both discrete and continuous dynamic behavior. As the links move they may break contact with the ground; however, while in contact with the ground, assuming no slipping, the body will translate in proportion to the motion of the arms. The combination of discrete and continuous behavior coupled with the frictional aspect of this problem can make it difficult to study analytically.

Despite the difficulties involved in studying this system, it still represents the simplest possible geometry capable of performing crawling motion. Disregarding variable friction systems, three links are the minimum number of links necessary to perform a crawling motion. On the opposite end of the spectrum, a great deal of research has been done on the dynamics of both biological and robotic soft crawlers, which represent infinite dimensional system [88, 89, 90]. This type of locomotion is useful to study because it can handle terrain with uncertain geometry, by lifting part of the body off the ground [91].

Here we investigate the most fundamental crawling system where shape change produces movement. We measure how the length, l , to width, w , aspect ratio l/w affects the crawling performance for certain periodic shape change sequences or gaits. The specific gaits we will study are the square gait and diamond gait fig. 3.1. For living systems where shape change produces movement, it is important to know how best to sequence limbs to optimize that movement. To that end, we look into adapting a theoretical framework called geometric mechanics, to this system. Through this framework, we hope to understand and optimize arbitrary three-link crawlers under certain conditions.

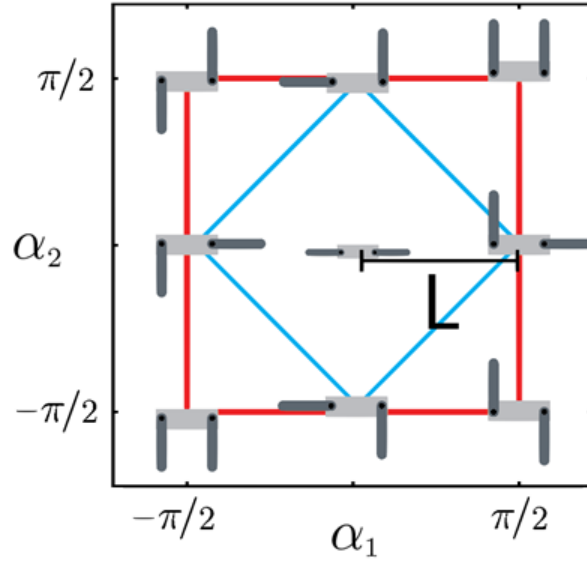


Figure 3.1: **Illustration of a square gait and diamond gait** The square gait (red) and diamond gait (blue) named for their shape. The gait size L is defined as the center to edge (or vertex), distance along the $\alpha_2 = 0$ line.

3.3 Materials and methods

The smarticle in this system was designed the same as explained in section 1.3. The center link of the smarticle was kept at, $w = 5.32\text{cm}$, and the length of the outer links can be changed out, $l = [2.13, 3.19, 4.25, 5.32, 6.38]$ cm (fig. 3.2(c)). In all crawling experiments, the smarticle was on an aluminum plate leveled flat to $< 0.1^\circ$. The smarticle's crawling motion was constrained to a single dimension by parallel aluminum extrusion bars fig. 3.2(a-b). The distance between the two bars was 3 cm, only slightly greater than the thickness of the smarticle (2.9 cm). At both ends of the confining area, embedded in the bars, were beam-break sensors (Sparkfun; Niwot, CO.). The beam-break sensors detected when the smarticle crossed its path (fig. 3.3(c)).

Upon crossing either beam-break sensor (fig. 3.3 (a-d)), an external Arduino Uno (Sparkfun; Niwot, CO.) connected to beam-break sensor would signal the computer to stop the current run (since the smarticle reached the end of the system), stop the smarticle, send the parameters for the next trial to the smarticle, and to resume movement again by re-

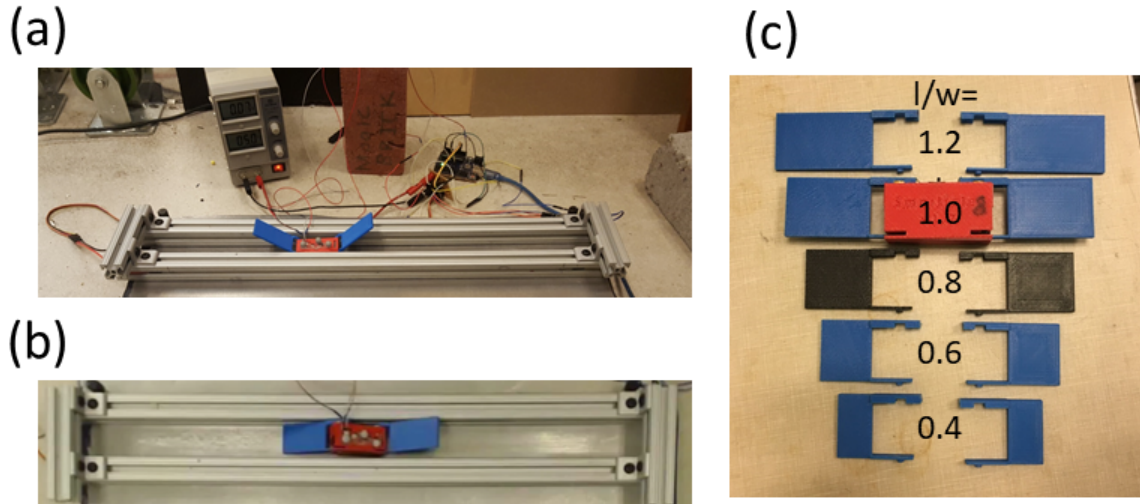


Figure 3.2: **Smarticle walker experimental setup** (a-b) Two views of smarticle walker experiment. (c) various arm lengths l/w shown.

versing the gait direction. Unlike the rest of the smarticle experiments in this dissertation, the smarticle crawler was connected directly to a power supply rather than a battery. The power supply served two purposes: it kept the voltage and motor speed steady and allowed the system to run for as long as necessary without necessary intervention or power loss concerns.

In experiments, smarticle positions and rotation were tracked using an infrared video recording hardware/software suite (OptiTrack; Corvallis, OR). The three IR sensors (shown in fig. 3.3(e)) were tracked as a rigid body, allowing orientations and rotations to be recorded. This data was used to ensure the system was periodic and to determine the beginning and ending of cycles.

For trials where the gait-length L was varied, each angle was repeated 10 times for each travel direction in 2° intervals. The range of the angles used depended on which gait was being measured. For square gait trials, $L = [31^\circ - 87^\circ]$, and for the diamond gait trials, $L = [65^\circ - 87^\circ]$.

Next, we used a DEM simulation to help understand the mechanism behind the crawl-

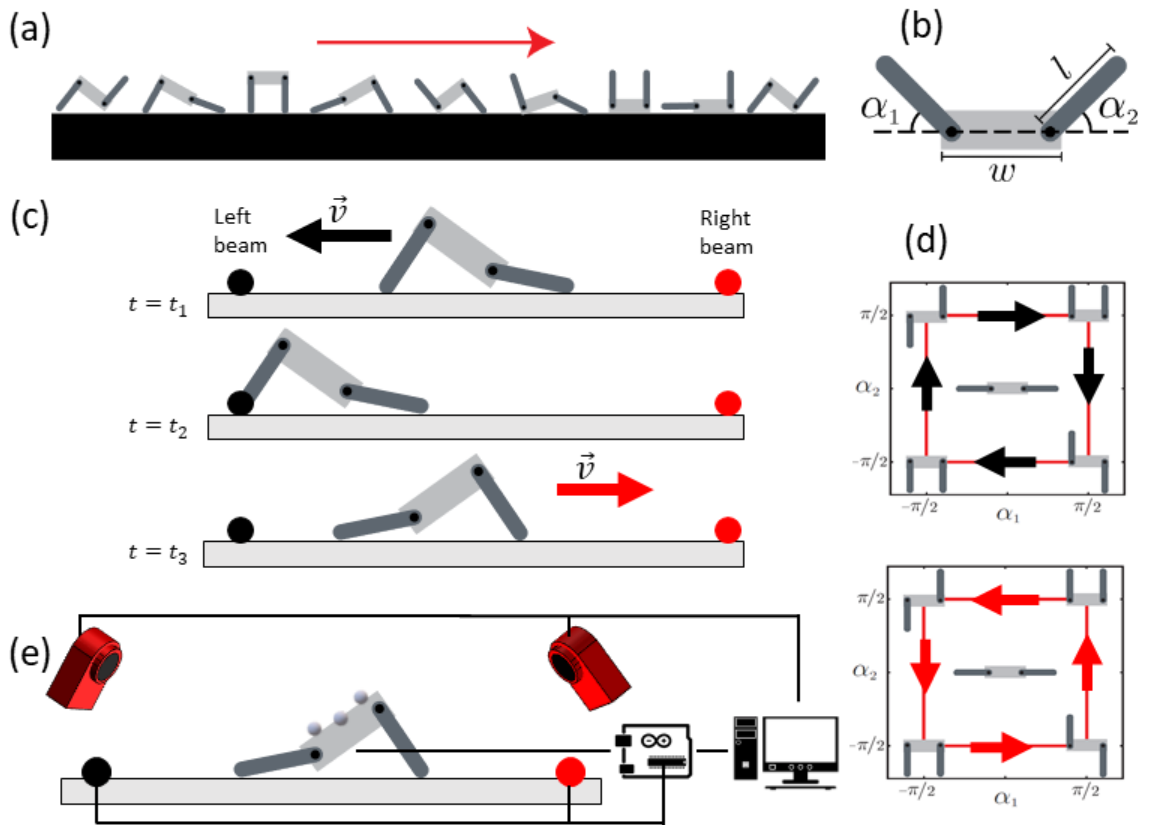


Figure 3.3: **Experimental crawling system and gait schematic**(a) 9 phases of a CCW square gait (b) a schematic of the coordinate system used (c) 3 key stages shown: once a smarticle a beam-break sensor, it reverses its gait direction and moves in the opposite direction. (d) CW and CCW gaits with positions at the vertices illustrated. (e) experimental setup schematic, the beam sensors transmit detection pulse to a computer which tells cameras to stop/start recording and tells the smarticle to change its gait direction

ing motion. The simulation was developed by a fellow lab member, Shengkai Li, which modeled the smarticle walker undergoing one-dimensional movement. In the simulation, the interaction between the smarticle and the ground is decomposed into the directions parallel, F_{\parallel} , and normal (or perpendicular), F_{\perp} , to the ground. The normal force uses the spring-dashpot model: the elastic force is linear and the dissipation is proportional to the velocity. For the parallel direction, the Hertzian friction acts antiparallel to the contact point considered's relative speed. The magnitude of the friction coefficient also depends on the relative speed of the point of contact. If it is larger than some threshold, the frictional force has the form $F = \mu_k F_{\perp}$, otherwise, $F = \mu_s F_{\perp}$, here μ_k is the kinetic friction coefficient, μ_s is the static coefficient. The friction coefficients used were measured from experiments using a force gauge, with $\mu_s = 0.43$ and $\mu_k = 0.37$. The values of the coefficients used for the normal force and the speed threshold, which distinguished static and kinetic friction, were designed such that the resultant behavior was minimally affected by different values.

Geometric mechanics theory to the smarticle crawler system[25]. For the theory to work, it assumes an ansatz based on the given shape where the joint angles are specified by the vector $\alpha = (\alpha_1, \alpha_2)$, the body velocity ξ is proportional to the shape velocity $\dot{\alpha}$. This is summed up in the relation

$$\xi = \mathbf{A}(\alpha) \cdot \dot{\alpha} \quad (3.1)$$

where $\mathbf{A}(\alpha)$ is referred to as the *local connection* (or Jacobian) matrix. For our two degree of freedom system crawler confined to one dimension of movement, $\mathbf{A} = (A_1, A_2)$ and eq. (3.1) simplifies to:

$$\xi = A_1 \dot{\alpha}_1 + A_2 \dot{\alpha}_2 \quad (3.2)$$

The values for \mathbf{A} we obtained by finding the best-fit planes for each shape α . These planes were generated by performing simulations which made small variations in movement around each α . \mathbf{A} can be visualized as a vector field on the shape space called a

connection vector field. By taking line integrals on the connection vector field along the paths the system traces, the crawler’s motion can be estimated. To further simplify the calculation, however, Stokes’ theorem eq. (3.3) can be applied to the local connection vector field. This produces what is called a curvature constraint function (CCF).

$$\int_{\partial D} \xi dt = \int_{\partial D} \mathbf{A}(\boldsymbol{\alpha}) \dot{\boldsymbol{\alpha}} dt = \iint_D \nabla \times \mathbf{A} da \quad (3.3)$$

Area integrals over the region the gait enclose in the CCF’s shape space gives information about the crawlers movements: both the magnitude and net displacement over a cycle. This theory is used to explain the functional form of the experimental gaits used.

3.4 Results and discussion

To find the effect of the geometry of the three-link has on crawling speed, we vary the limb sizes l and measure the speed for two different gaits. In fig. 3.4(a), at smaller L , speed increases with increasing l/w . For $l/w > 0.6$ at the larger gait sizes $L \geq 52^\circ$, the speed experiences a rapid drop. This was an issue with the experimental system: although the arm speed $\omega = 6$ rad/s for the servos was constant for all l/w , this meant that the linear velocity at the tips would increase as l/w increased. The rapid drop-off was a result of inertial effects in the system. This behavior only was seen only for the square gait. The diamond gait had smoother transitions where contact was pointed were typically farther from each other. We found the diamond gait to be insensitive to l/w .

We next calibrated the simulation with the experiment, using parameters from the experimental system, and used it as an input for the geometric mechanic’s framework. Geometric mechanics allows us to find optimal gaits in the shape space by performing integrals over the area contained inside the gait shape in the CCF. We start by computing the local connection for this system as described above and we retrieve the vector field $\mathbf{A}(\boldsymbol{\alpha})$ as shown in fig. 3.5(a). Although building up the local connection from experimental trials

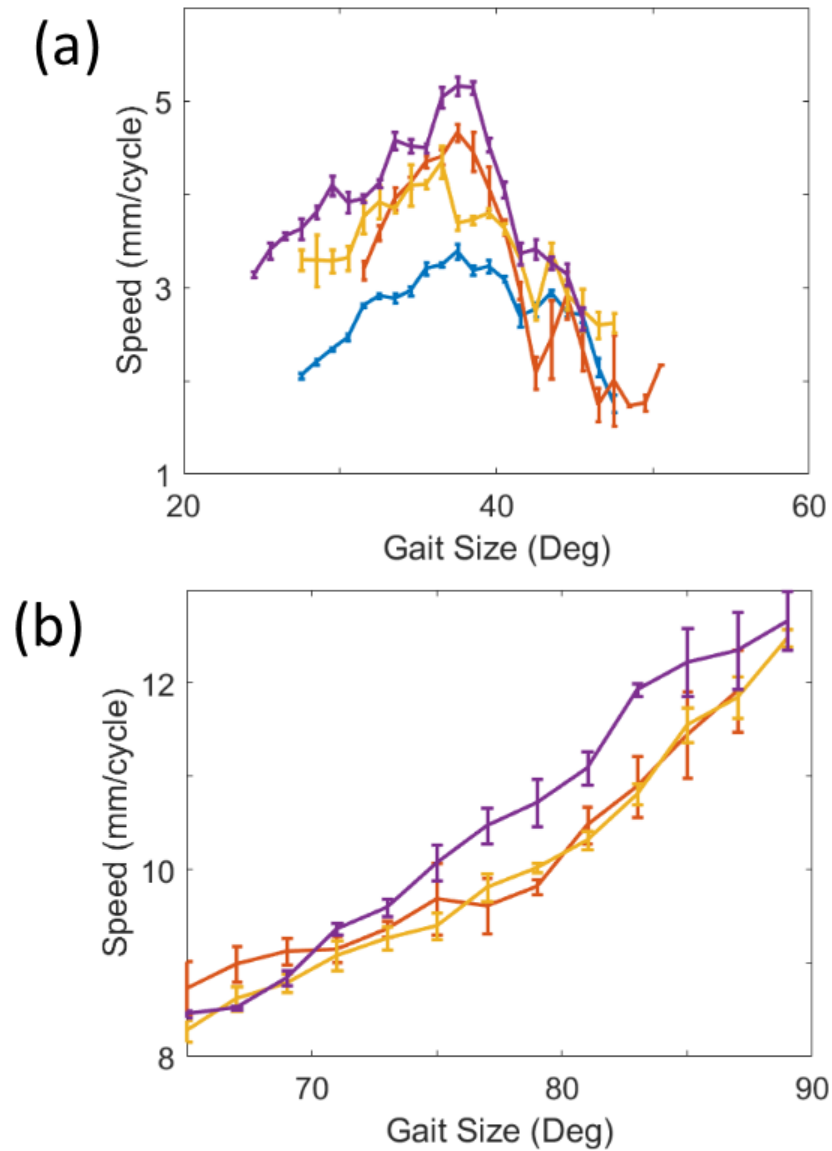


Figure 3.4: **Crawl speed as a function of gait size, for different l/w** (a) Square gait and (b) Diamond gait. Colors correspond to different l/w , blue, orange, yellow, and purple represent $l/w = [0.6, 0.8, 1.0, 1.2]$. Only CW gaits shown.

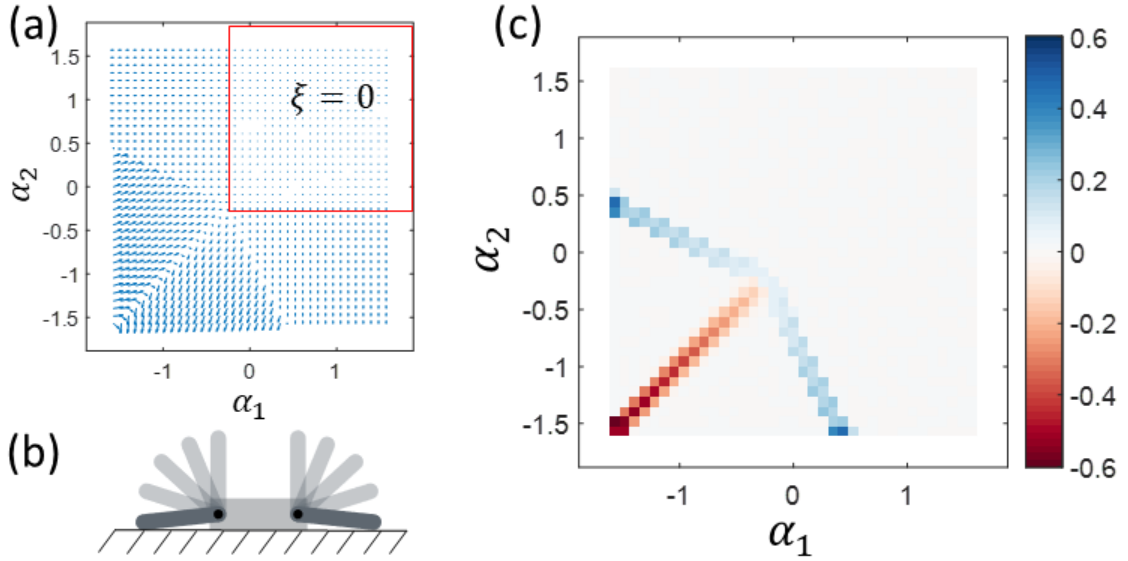


Figure 3.5: **Local connection and CCF of smarticle crawler** (a) local connection vector field (b) shows orientations represented inside the red box in (a) which gives a value of zero for ξ . (c) CCF of the smarticle crawler calculated from (a)

have been proven [26], with a simulation available it can be achieved much faster. Because of the uniqueness of our system due to its hybrid-dynamical nature, the local connection has a peculiar vector field. In an area slightly larger than the top right quadrant of the shape space $\xi = 0$ everywhere. This is a result of the thickness of the central link. This area corresponds to the situation shown in fig. 3.5(b); the outer link never can never interact with any other bodies (i.e. the ground) when traversing this area, therefore, no body motion is produced from $\dot{\alpha}$.

The local connection vector field was transformed to a CCF using eq. (3.3) giving us fig. 3.5(c). Net displacement tracks the area enclosed, with a sign dependent upon the direction traveled around the gait.

When comparing the experimental diamond gait fig. 3.6 to the simulated and geometric mechanics results, for a $l/w = 0.6$ and relatively slow speeds, the experimental results match well with simulation. Low speeds keep the system from becoming inertial, a necessary condition for geometric mechanics. While the magnitude is not exactly correct the functional form is quite close.

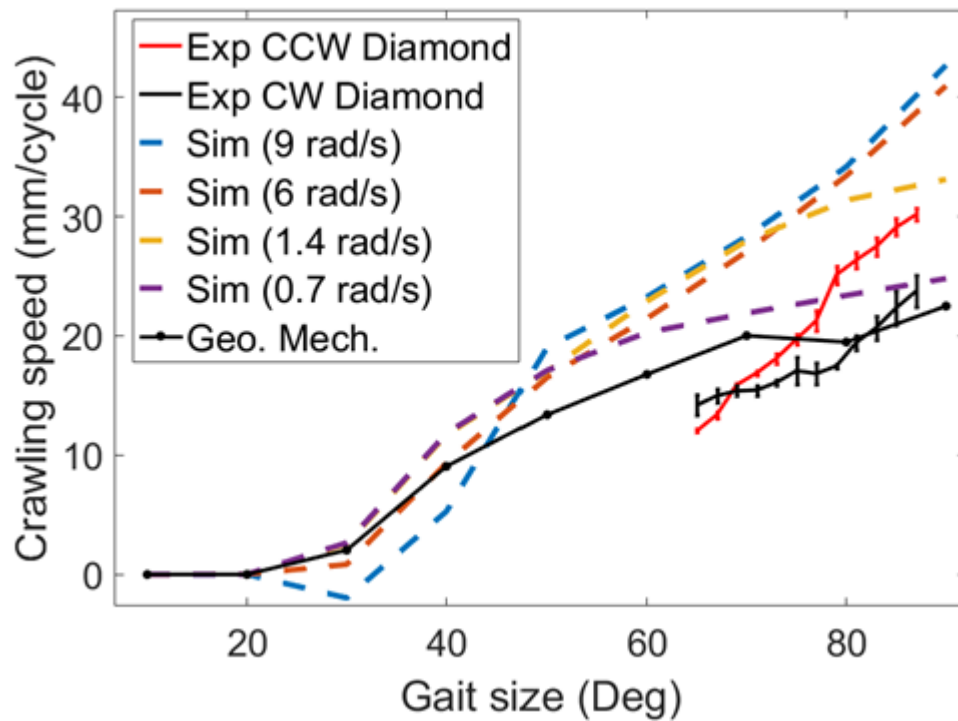


Figure 3.6: **Diamond gait comparison for simulation, theory, and experiment** Comparison between simulation theory and experiment for a diamond gait. The geometry used for the crawler used is $l/w = 0.6$. To allow comparison, we put the experimental CW gait in the frame of the CCW gait

Unfortunately, the motors used in this system had a fixed speed and could not be matched to simulation, therefore we could not properly compare test gait speeds which would presumably match most closely with the geometric mechanic's result. The experimental system (which moves at $\omega = 6$ rad/s, underperformed the simulation for this particular gait. We believe asymmetries which exist in the smarticle system, (the weight distribution, and imperfections in the shape) lead to differences in the speed between the CW and CCW gaits, which should, in theory, give the same result. Finally, we also note that the error between the simulation and theory increases with increasing L , as predicted in [20].

The square gait fig. 3.7, as with the diamond, showed good agreement between simulation and geometric mechanics at the smallest ω tested. Interestingly though, the experimental system's square gait had a closer agreement, in both functional form and magnitude, to the simulation (with the same parameters as used in the experiment). The experiment had a better agreement between both directions of travel as well. We suspect this is due to a smaller l/w as mentioned earlier.

Finally, geometric mechanics gives us another way to analyze and understand the functional forms of the two gaits we chose as a function of increasing L . In fig. 3.5(c), the red (positive) area has a higher magnitude nearer the origin than the individual blue strips (negative area). The addition of both blue areas will generate a larger total sum than that of the red. For the diamond gait, as the diamond grows, it adds more blue area than red area. From $L = 30^\circ - 40^\circ$ the crawling speed grows faster, then slows. This change in speed corresponds to the areas enclosed changing as an origin centered diamond expands in area. The vertices in the $\alpha_1 < 0$ and $\alpha_2 < 0$ are continuously enveloping more blue area. Near $L > 0.5$ rads, the vertex, which grows proportionally faster than the edges by a factor of $\sqrt{2}$, is no longer enclosing blue area as it increases in size, only the edges do. As a result, the speed slows for $L > 40^\circ$ as shown in fig. 3.6.

In the case of the square, as previously stated, the red has a greater value nearer the origin. But as the square grows, the speed, which initially increases with L , eventually

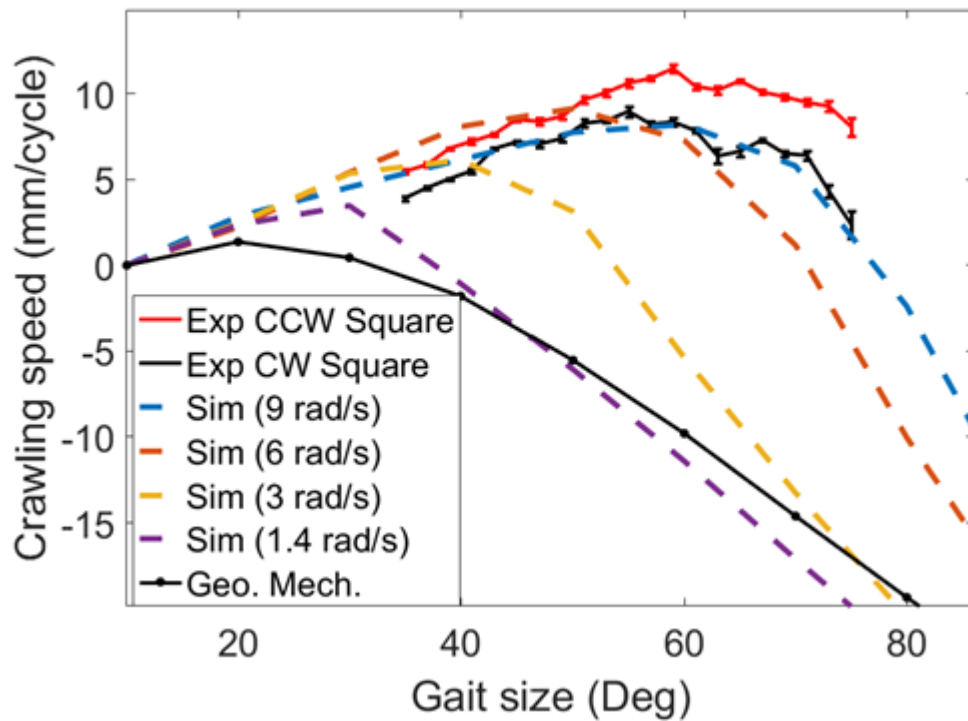


Figure 3.7: **Square gait comparison for simulation, theory, and experiment** Comparison between simulation theory and experiment for a diamond gait. The geometry used for the crawler used is $l/w = 0.8$. To allow comparison, we put the experimental CW gait in the frame of the CCW gait

begins to decrease. The area of the two blue regions grows faster than the area of the single red region. As L increases for this system past the turning point, it seems to decrease linearly. As the area goes from $(2L)^2$ to $(2(L + dL))^2$ because of the geometry of the space and of a square, the amount of enclosed area will grow linearly as well. This line of reasoning matches the actual geometric mechanical system's result fig. 3.7 decreases in speed at a linear rate.

Finally, we mention that for our system the, optimal gaits which the framework could properly estimate would be those which surround only the blue areas. From [20], the largest errors in velocity estimation happen the $\alpha_1 = \alpha_2$ line and away from the origin. Therefore, the lower left area in red would have a large error and should be avoided.

3.5 Conclusion

We were able to identify that different gaits would not be affected in the same way. For a square gait, we found at certain gait sizes an increase in aspect ratio would improve crawling performance but it could have a deleterious effect on efficiency at larger gait sizes. For the diamond gait, we found no strong effect with regard to changes in aspect ratio.

We then used experimentally calibrated our simulation to help apply geometric mechanics to our hybrid dynamical system, the first application of this kind to the authors' knowledge. For small enough link speeds, geometric mechanics had very good agreement with our simulated system. Although geometric mechanics did not generally agree with the experiment, with respect to the magnitude, for our particular instantiation of a three-link robot, it does indicate it may be possible. Our particular robot had asymmetries, and the speed was too fast to allow a proper comparison. Despite these differences, geometric mechanics still captures both the general form and magnitude for the DEM simulation.

Finally, we believe for future studies it would be interesting to see if geometric mechanics could be further utilized to help optimize not only gait type but system morphology as well.

Further studies are planned for smarticles which will be used as a task-oriented active matter. These planned experiments will focus on walking or crawling. The results from this experiment will help to inform future smarticle shapes and limb sequences to ensure efficient movement.

CHAPTER 4

SUPERSMARTICLE

4.1 Summary

Most active matter systems are composed of elements that can self-propel; ensemble dynamics like flocking are therefore summations of individual locomotors. Here we study immotile robotic smart active particles (smarticles) in which the ensemble can emergently locomote only via stochastic mechanical interactions among shape-changing individuals. When enclosed in a rigid ring, a group of smarticles displays persistent emergent diffusion; light-triggered deactivation of a single smarticle can be used to generate a controlled phototaxis. A statistical model explains the observed drift, giving insight into design and control of robustly task-capable active materials.*

*This chapter was adapted from a journal article submitted to *PRL* entitled “*Motion from no motion: emergent transport in self-deforming and colliding immotile active matter*”

4.2 Introduction

Self-propulsion [18] is a feature of living and artificial systems across scales – from crawling cells to swimming spermatozoa [92] and micro-swimmers [93] and nano-swimmers [94], to running cockroaches [95] and robots [27, 40]. It is generally assumed that self-propelling systems require carefully orchestrated integration of many diverse components to perform the seemingly simple behavior of spatial translation. Thus, artificial locomoting systems typically consist of a central controller, a set of actuators and some sensors to perform feedback control; such designs have led to progress in machines that robustly and nearly-autonomously roll [96], fly [97] and walk [98] in relatively predictable environments.

We posit that future robots might generate self-propulsion using systems in which a delineation of such components is not so clear. That is, suppose that the elements composing a locomotor are not arranged in a careful scheme, nor even coupled deterministically. We can draw inspiration from the fields of modular and swarm robotics [99, 11] and active matter which have made progress in control of collectives (e.g. [100, 11, 101, 102, 103, 104, 105]) and have even generated collective self-propulsion via rectification [106, 107] of stochastic motion of individuals. However, collective locomotors will invariably encounter environments in which individuals might be incapable of self-propulsion, or interactions with the environment so complex and unpredictable that modeling and design become impractical.

In this chapter, we seek to discover principles by which a collective could overcome such locomotor limitations via purely mechanical interactions among the individuals. We study a simplified robophysical [28] system of controllable “smarticles” (smart, active particles) that are immotile but can change their shape. Although individually immotile, an enclosed ensemble (a “supersmarticle”) can self-propel diffusively by utilizing the interactions arising from shape modulation of smarticles. Moreover, despite the stochastic nature of the interactions between elements, the supersmarticle is capable of directed motion via selective shape immobilization of individual smarticles; we demonstrate the utility of this

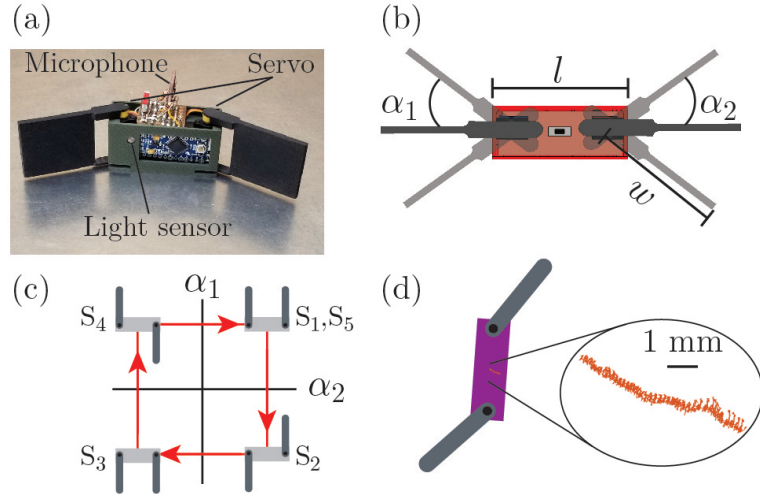


Figure 4.1: **Smarticle robot and dynamics** (a) Smarticle at rest and (b) top view schematic $l = 5.3$ cm and $w = 4.9$ cm. (c) Clockwise (CW) square gait, with key configurations enumerated. (d) Drift of a single smarticle on a flat surface, executing a square gait over 60 s or 38 gait periods.

scheme through exogenous and endogenous drift induced by light sources.

4.3 Material and methods

Smarticle individual and collective motility – Each low-cost smarticle (mass $m = 34.8 \pm 0.5$ g) is a robotic instantiation of Purcell’s three-link swimmer [17, 25], see fig. 4.1(a,b). The outer case and arms of the smarticle are 3D printed. The arms are controlled by HD-1440A servomotors to a precision of ($< 1^\circ$) and with an accuracy of $\pm 6^\circ$. All processing and servo control are handled by an Arduino Pro Mini 328 - 3.3V/8MHz (Sparkfun; Niwot, CO.) which allow smarticles to move to specific configurations and gaits, the latter defined as periodic trajectories in the configuration space, see fig. 4.1(b-c). The system is powered by a 3.7V 150 mAh 30C lithium polymer battery (Venom;Rathdrum, ID.) enabling hours of testing. In experiments, smarticle positions and rotation were tracked using an infrared video recording hardware/software suite (OptiTrack; Corvallis, OR). All experiments were conducted on a 60×60 cm aluminum plate leveled flat to $< 0.1^\circ$, shown in fig. 4.2(a).

Just like Purcell’s three-link swimmer [17], smarticles undergoing a self-deformation

pattern (e.g. a “square gait” depicted in fig. 4.1(c)) can self-propel when immersed in a continuous media, like a viscous fluid, or an approximately-continuous media, like granular media [25]. However, outside of any media, when resting in an orientation where the links’ axis of rotation is parallel to the normal of the surface it rests on (fig. 4.1(a)), smarticles are incapable of translation or rotation see fig. 4.1(d). This is because the moving components, the outer links, rest above the central link and never interact with the surface.

4.4 Results and discussion

4.4.1 Smarticle cloud

Despite their inability to self-locomote in the upright orientation, we discovered that an ensemble of self-deforming smarticles (a “cloud”) could display rudimentary collective locomotor capabilities. The cloud experiment begins with seven active smarticles tightly packed in a random orientation; we track the positions of the individuals in the collective as they interact with their neighbors over time. Each smarticle performs a square gait fig. 4.2(a). As time evolves smarticles both repel and “attract” their neighbors. Collisions which generate attraction between particles (via arm entanglement as in [108]) are a result of interactions which are only possible because one or more of the agents are concave at the time of the collision. Unlike single smarticle experiments, we find that the center of mass of the cloud can diffuse over scales comparable to the size of a smarticle (fig. 4.2(b)). However, after sufficient time, the mobility slows as smarticles separate and no longer interact strongly. We quantified the mobility using the cloud’s “granular temperature,” defined as $\langle V^2 \rangle = \langle \langle v^2 \rangle_n - \langle v \rangle_n^2 \rangle_N$, where $v = \sqrt{\dot{x}^2 + \dot{y}^2} + (2w + l)\sqrt{\dot{\theta}^2}$ sums the translational plus rotational velocity of n smarticles and averages them over N trials.

Both $\langle V^2 \rangle$ and ϕ the area fraction typically decreased over time as in fig. 4.2(c,d), with the granular temperature approaching the noise floor [109] after sufficient time. Here $\phi = \frac{A_c}{nlw}$, where A_c is the area of convex hull of the smarticles (bodies and arms) in the cloud (fig. 4.2(a)), where n is the number of smarticles in the system. The decrease of

granular temperature of the ensemble was connected with the decrease in the area fraction of the collective. The decrease in ϕ was a robust result seen in 20 experiments, all smarticles started with random initial positions and orientations, but packed tightly such that all smarticles were in contact with a high initial ϕ . Surprisingly, the decrease in ϕ was not always monotonic; in certain trials, increases in ϕ occurred, as in fig. 4.2(a,d). Although all interactions are repulsive because the smarticles can change transform into concave shapes the collective was capable of “compressing” the smarticles collective at some points. Compression can be interpreted as a type of “geometric cohesion” (as in [108]) as smarticles configure themselves into concave geometries allowing them to pull on neighbors during a gait cycle.

4.4.2 Supersmarticle dynamics

On long timescales, the cloud’s granular temperature, and therefore its potential for locomotion approaches zero. Given the correlation between ϕ and $\langle V^2 \rangle$, we expected we could sustain locomotor capabilities at long timescales by constraining ϕ of the collective. To achieve this, we confined five smarticles within a ring, creating a “supersmarticle”. Each smarticles in the supersmarticle starts at a random phase and continuously performs a square gait inside an unanchored rigid ring of radius $R = 9.6$ cm and variable mass m ($m \in [9.8\text{g}, 207\text{g}]$), fig. 4.3(a). The ring size diameter was chosen such that ϕ and $\langle V^2 \rangle$ remained high, yet there was enough ring area that jamming was rare and always self-resolvable.

The ring confinement maintained ϕ at approximately that of the value observed at the initiation of the cloud trials, fig. 4.2(d). Similarly, the granular temperature of the supersmarticle system fig. 4.3(b) remained at approximately the value found only at the highest ϕ seen in cloud trials (fig. 4.3(d)). This led to persistent diffusive transport of the supersmarticle. Within the ring, individual smarticles displayed complex interactions (fig. 4.3(c)), often displacing an amount comparable to, or greater than, the displacement of the ring

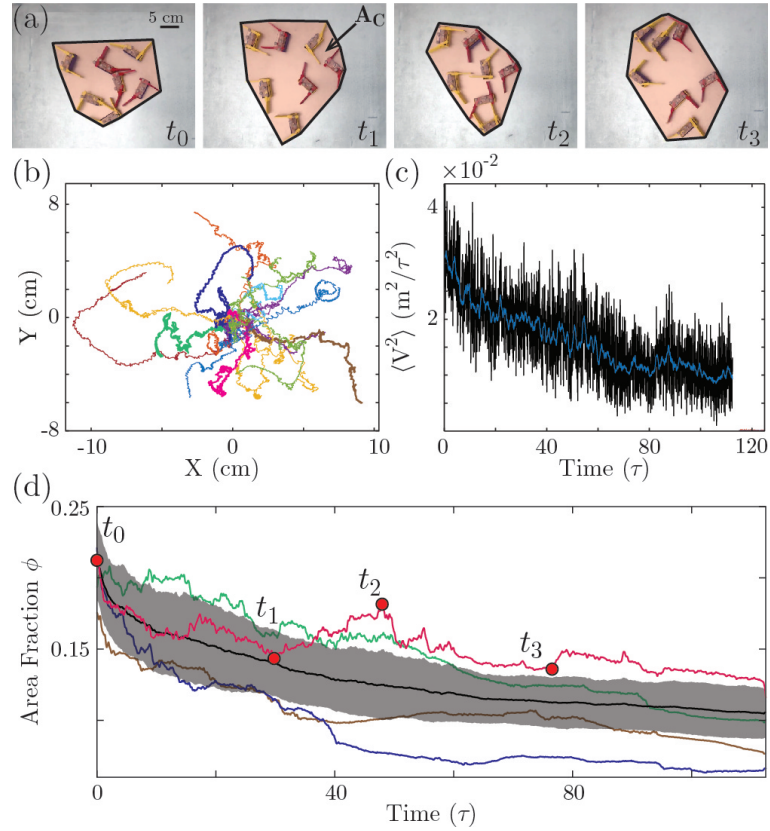


Figure 4.2: **Smarticle cloud cooling and diffusion** (a) Snapshots of smarticle “cloud” system, the transparent red overlay represents the convex hull area A_C used to calculate ϕ . Time of snapshot is indicated by t_n corresponding to a particular time in (d) below. (b) Center of mass trajectory of the cloud system, each line represents a different trial. The shared colors in (d) represent the same trial shown here. (c) The average granular temperature of the same 20 trials shown in (b). Raw data is in black, where the blue line is moving mean with a window size of 1 gait period. Pink is a sample of granular temperature noise of an experiment with seven moving, but non-interacting, smarticles. (d) The evolution of ϕ for three separate experiments in blue, red, and green. The average ϕ evolution over all 20 trials is black, with the gray shaded region representing standard deviation. For the trial in pink, ϕ does not strictly decrease. On small timescales, periods where the cloud compresses are defined by an increase in ϕ . Here gait period $\tau = 1.6$ s.

itself.

Tracking the ring’s motion (fig. 4.3(c)) for a ring of mass $m = 68\text{g}$ revealed no correlation between final angular position from trial to trial (e.g. fig. 4.3(d)). Since in a given trial the supersmarticle’s trajectory is stochastic, we used $\sigma^2(t)$, the mean square displacement (MSD) of the ring, to characterize the motion: $\sigma^2(t) = \langle x^2(t) \rangle - \langle x(t) \rangle^2$ where $\sigma^2(t) \propto t^\gamma$. The supersmarticle exhibited different types of motion depending on the timescale observed. The short timescale regime was consistent with $\gamma = 1$ (fig. 4.3(e)) indicating normal diffusive motion. The long timescale regime were best fit with $\gamma \approx 1.45$ representing directionally invariant superdiffusive motion.

We discovered that if a smarticle near the boundary became “inactive”, by maintaining a fixed straight shape (fig. 4.4(a)), the supersmarticle displayed directed drift on short time-scales. Since the angular position of the inactive smarticle around the ring was not fixed, in the lab frame, drift in a constant direction was not observed on longer timescales, see fig. 4.6. However, when trajectories were examined in the frame (fig. 4.4(b)) of the inactive smarticle, fig. 4.4(c), the bias in drift (in this case, toward the inactive smarticle) became clear. Like the fully active supersmarticle, the dynamics of the supersmarticle containing an inactive smarticle were also superdiffusive, and at short timescales at ($\gamma \approx 2$) approximately ballistic.

4.4.3 Statistical model

To understand the supersmarticle diffusion and drift, a kinetic theory-like model was developed by Zachary Jackson. We imagine the active smarticles rattling inside the ring, and consider the ensemble of collisions of an active smarticle with the ring and/or inactive smarticle. The mean displacement of the ring is $\langle \Delta \vec{R} \rangle = \int P(\vec{Y}) \Delta \vec{R}(\vec{Y}) d\vec{Y}$, where \vec{Y} specifies the microstate of the system just before a collision, and $\Delta \vec{R}$ is the ring displacement due to the collision. In principle, \vec{Y} comprises the initial position, orientation, and heading of the active smarticle as well as the initial position and orientation of the inactive

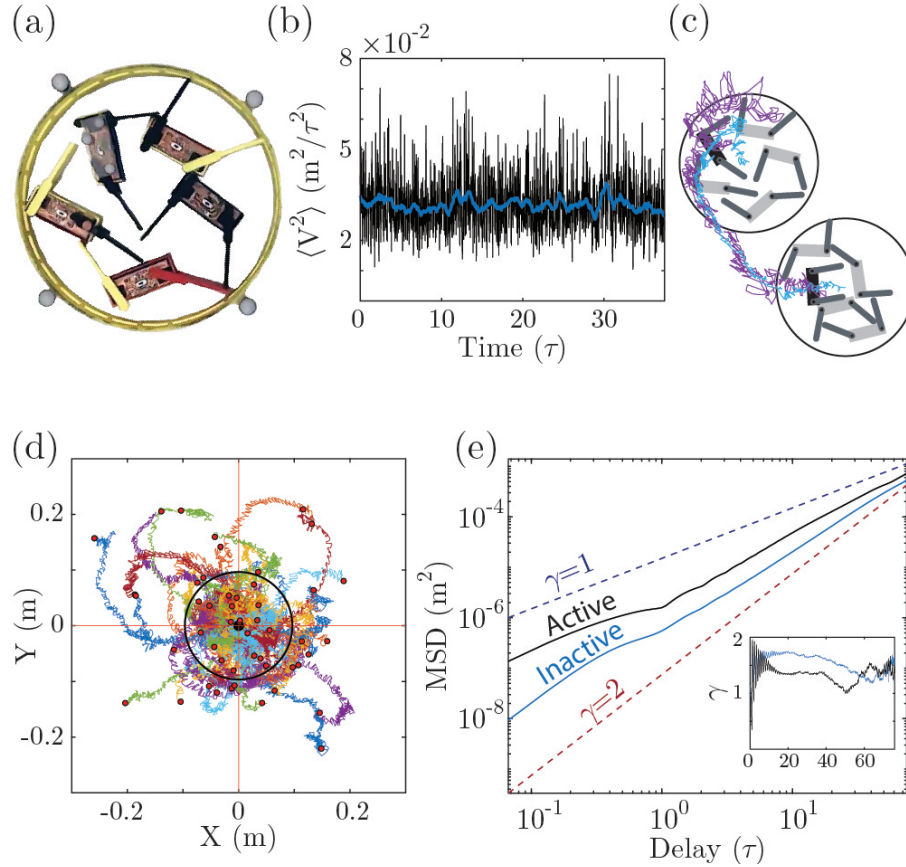


Figure 4.3: **Collective confined diffusion** (a) Supersmarticle top view with all particles active, ring has an inner radius of 9.6 cm. (b) The granular temperature of 5 active smarticles confined in a ring. The black line is the raw granular temperature, blue is a moving window mean with a window size of a single gait period. (c) A schematic showing the trajectory from a single trial. The purple line is the trajectory of a smarticle inside the ring, the blue line represents the ring's COM trajectory. (d) Multiple experimental tracks from an all active supersmarticle system where $m_{ring} = 68$ g. The black ring represents the size and original position of the ring (e) The MSD averaged over 50 and 80 trials for the active and inactive systems respectively all lasting two minutes. The inset shows the average change of γ for active(black) and inactive(blue) systems. The oscillation seen in both the MSD and γ is related to the gait period τ (Here $\tau = 1.6$ s)

smarticle. We partition the space of \vec{Y} into six distinct collisions, defined by two independent factors: (a) whether or not the inactive smarticle is in contact with the ring, and (b) which of three regions the active smarticle makes contact (denoted by Roman numerals in fig. 4.4 (e), see also table 4.1. For example, in two of the six “collision types” the active smarticle is incident on region III of the ring, resulting in either a three-body collision (if the inactive smarticle is in contact with the ring) or a two-body collision (if it is not). By symmetry, the mean displacement of ring, averaged over all collisions, is horizontal, and $\langle \Delta X \rangle = \sum_{r=1}^6 \langle \Delta X_r \rangle$.

We calculate the individual ring displacements using the simple 1D model depicted in fig. 4.4(d). The active smarticle comprises a torso m_2 connected via an actuated piston to an arm m_1 ; the arm, in turn, pushes on the target m_b , which consists of the ring and/or the inactive smarticle, depending on collision type. It is straightforward (if a little tedious) to find the ring displacement for each of the six collision types (see appendix).

The theory correctly predicts the observed drift direction of the supersmarticle. In fact, the theory predicts that this direction will be *reversed* for large enough ring mass: directionality depends on the mass ratio $\mathcal{M} = m_{smarticle}/m_{ring}$ between the inactive smarticle and the ring, with a reversal at a critical value of $\mathcal{M} \approx 0.8$. To test this prediction, we conducted experiments for a series of different ring masses. The results are summarized in fig. 4.4(f). The theory does an excellent job predicting the mean velocity, including direction reversal.

The model elucidates the physics behind this behavior. Consider first the high- \mathcal{M} limit. The three collision types involving the (light) ring but not the (heavy) inactive smarticle dominate the net motion. Both of the forward collisions (region II) are of this type, as is one rearward (region III) collision, resulting in a relatively large positive $\langle \Delta X \rangle$. Conversely, in the low- \mathcal{M} limit, five of the six collision types give rise to nearly equal magnitude ring displacements, the exception being the forward collision (region I) of the active smarticle with the inactive smarticle when the latter is not in contact with the ring, in which case the

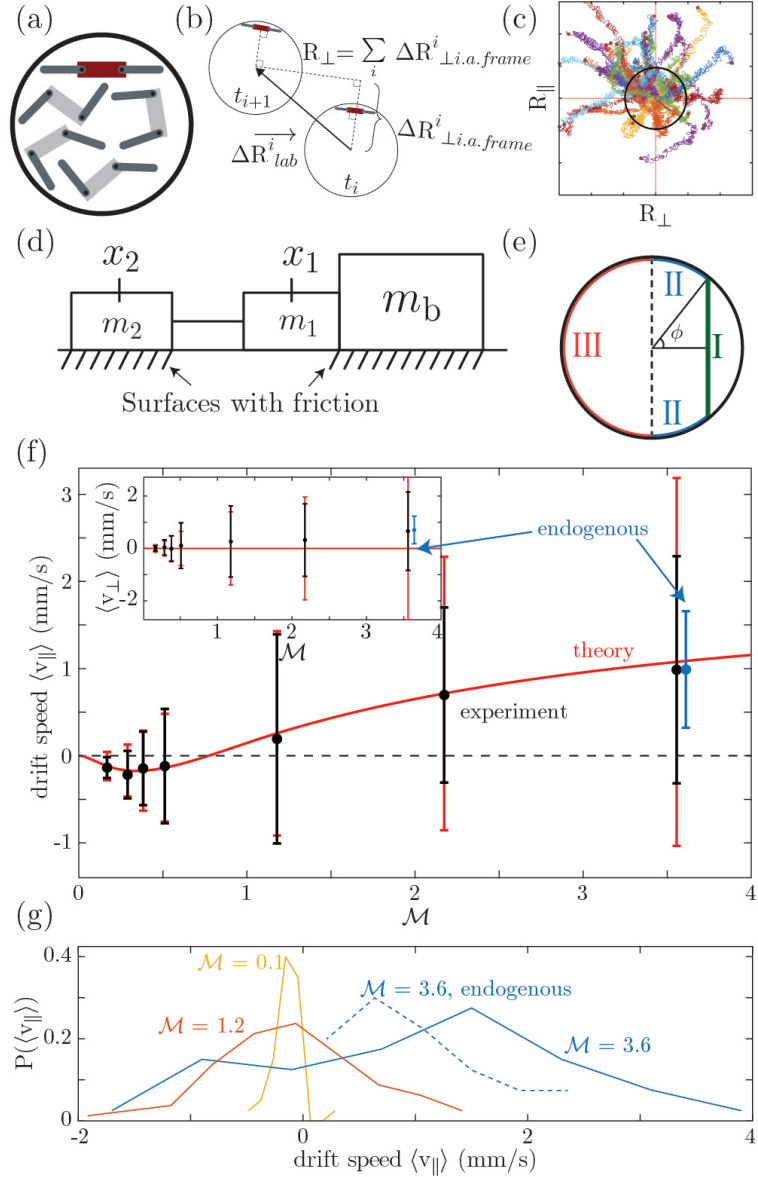


Figure 4.4: **Supersmarticle drift and model** (a) Supersmarticle schematic, with the inactive smarticle in red. (b) Supersmarticle trajectory frame transformation from lab frame to inactive smarticle frame. (c) Supersmarticle trajectories $m_{ring} = 9.78$ g for separate experiments rotated into the inactive smarticle frame. Black ring denotes the initial position and size of the ring ($\varnothing = 19.2$ cm). (d) Schematic of the theoretical collision model. (e) Regions used to classify distinct collision types for the theory as described in the text. (f) Theoretical (red) and experimental (black, blue) data for velocity vs. mass ratio \mathcal{M} , showing mean and standard deviation. The blue line is offset in \mathcal{M} for visibility and represents an experiment where the inactive particle was endogenously chosen by light (see text) for 40 trials. (g) Histograms of $\langle v_{\parallel} \rangle$ for different \mathcal{M} regimes. The sharpness of the distributions depends on \mathcal{M} . The blue dashed line, $\mathcal{M} > 1$, was endogenously light-driven with 40 trials taken. Multiple experimental trials, between 40 and 100, were taken for each ring mass with each experiment lasting for a time t ($t \in [90s, 150s]$).

ring displacement is exactly zero. This deficit in the forward-directed ring displacement results in a (small) negative value for the net displacement.

The excellent agreement between theory and experiment for the mean velocity is perhaps surprising: with only $N = 4$ active smarticles, it is not clear that a purely statistical kinetic theory approach should work. In fact, the theory overestimates the observed fluctuations, an indication of substantial correlations in the smarticle swarm. Including the dynamical origin leading to these correlations is an ongoing theoretical challenge.

To create a supersmarticle capable of directed motion visible in the lab frame, the angular location of an inactive smarticle must be controlled. By designing smarticles responsive to light, the location of the inactive smarticle could be held constant. A smarticle becomes inactive when it senses an amplitude of light, from its photosensor, above a certain threshold. If the light is shone on the system, in the same plane as smarticle's light sensor, then, as a smarticle shifts to the inactive orientation it will occlude light from neighbors behind itself, fig. 4.5(a-b). If the illuminated location is controlled, the location of the inactive smarticle (in the ring) is *exogenously* controllable, leading to a (roughly) steerable supersmarticle. As a proof of concept, by using a flashlight, we were able to direct the supersmarticle through a simple maze (see fig. 4.5(c)) by continuously targeting the appropriate inactive smarticle (typically closest to the desired direction).

Such exogenous forcing requires external feedback (in this case from the experimenter) to control direction. However, we discovered that the supersmarticle would also drift toward a static light source via *endogenous* forcing, that is, where smarticle immobilization was selected for by nearest proximity to the light source, see fig. 4.5(d). The mechanism by which the endogenous control was effected was via the switching of inactive particles most affected by light. Since collisions in the ring can cause the inactive smarticle's position to shift, when the currently inactive smarticle is dislocated from its lighted position, it will switch to an active state. Further, an active smarticle may simultaneously shift into a position where it may receive enough light to become inactive.

The endogenously forced system drifted in a preferred direction in the laboratory frame with a similar speed (fig. 4.4(f)) to that of the non-light driven system, whose drift was only observable in the frame of the inactive smarticle. This is remarkable given the complex switching dynamics of the inactive smarticle (fig. 4.5(e)): for example, depending on the distance to and orientation relative to the light, it was possible for multiple smarticles to be simultaneously inactive as depicted in fig. 4.5(e). Thus while crude, the endogenously drifting supersmarticle result demonstrates that the collective can perform a task/behavior [16] such that locomotor control of the system is decentralized and offloaded completely to mechanical interactions [110]. Concepts from distributed computing [111] could be used to improve tracking (increasing drift relative to diffusion).

4.5 Conclusion

We have used custom-made, low-cost, robophysical devices to discover how collective self-propulsion can be generated from stochastic interactions among individually immotile but shape changing smart-active-particles (smarticles). While a cloud of smarticles displayed transient drift and diffusion of the center of mass, an enclosed group of smarticles (a supersmarticle) displayed persistent diffusion; changes in the activity of an individual led to drift. A statistical model captured aspects of the drift, pointing toward methods to steer the supersmarticle. We implemented such control via exogenous and endogenous activity changes of individual smarticles.

We posit that further study of the importance of mechanical aspects of collective self-propulsion (in essence, so-called “morphological computation” [112]) could lead to novel designs of robots, perhaps improving the robustness of artificial locomoting systems to changes in terrain. Such robustness enhancements could be valuable in robots and swarms across scales, from medical applications at nano/micro scales [113, 114, 115] to search-and-rescue devices on macroscales [116]. Perhaps future reliable robots could be constructed from unreliable components, providing a physical analog to Shannon’s reliable

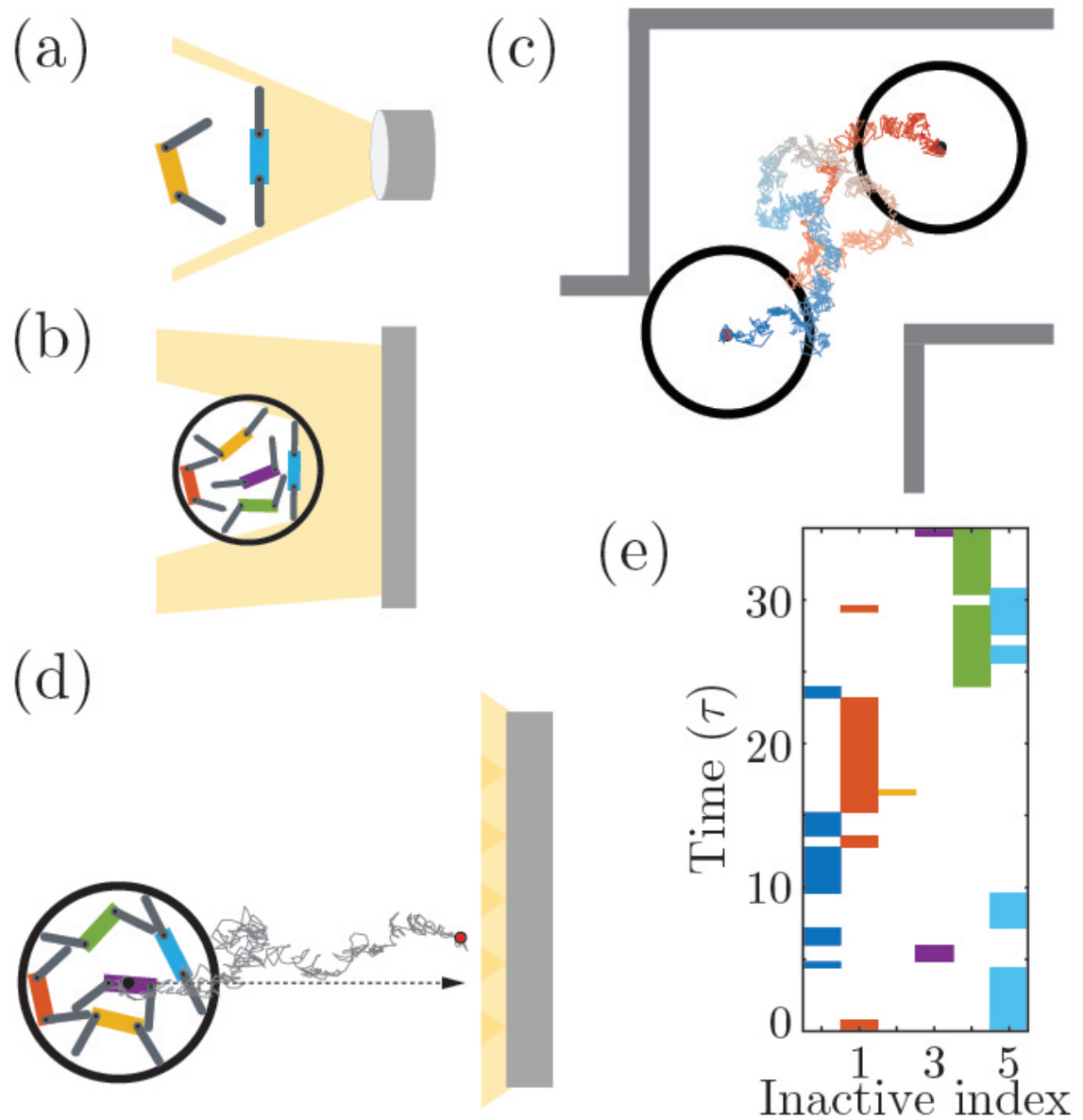


Figure 4.5: **Supersmarticle phototaxis** (a) Depiction of occlusion of light by the inactive smarticle to its trailing neighbors. (b) Overhead view of supersmarticle phototactic setup. (c) A photophilic trajectory of supersmarticle where system followed a light (exogenous forcing) through a maze. Trajectory evolution transitions from red to blue as time increases, black rings represent size (outer diameter of ring $\varnothing = 21.5$ cm) and position of the ring at initial and final positions in trajectory. (d) An endogenous photophilic supersmarticle trajectory tracking a static light source. Smarticle positions and configurations shown are true to the experiment at the frame shown. (e) Map depicting which and when smarticles endogenously inactivate in response to the fixed light.

circuits from unreliable components [117].

4.6 Appendix

The supersmarticle trajectory before being rotated into the lab frame appears similar to the results from the all active system. As seen in fig:unrotTrajs there is no clear directional bias for any of the mass distributions.

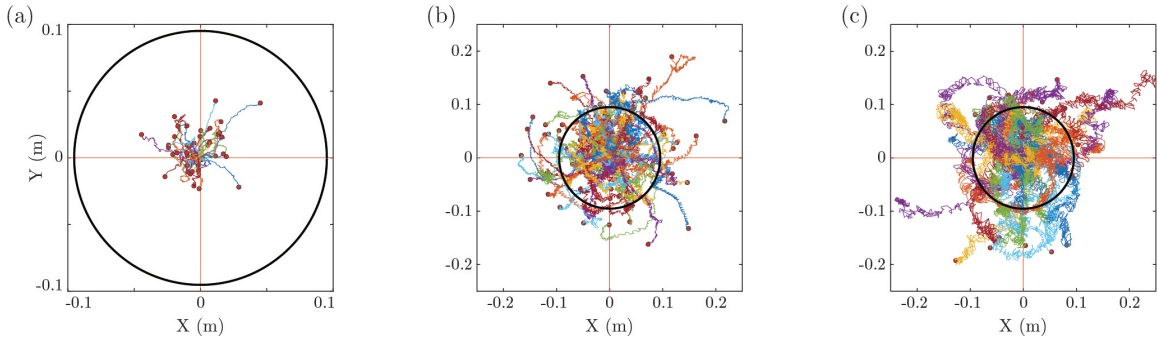


Figure 4.6: **Unrotated trajectories for different \mathcal{M}** Unrotated trajectories for different \mathcal{M} (displayed in the lab frame) supersmarticles for three different mass ratio rings. (a) $\mathcal{M} < 1$ (experiments ran for 120 s) (b) $\mathcal{M} \approx 1$ (experiments ran for 120 s) (c) $\mathcal{M} > 1$ (experiments ran for 90 s)

A GitHub repository containing all of the files necessary for building a smarticle can be found at <https://GitHub.com/wsaveoie/ArduinoSmarticle>.

We represent the active matter system with a stochastic two-dimensional model consisting of a ring, a group of active smarticles, and inactive robot in a straight, fixed position. The active robots act on the ring with a series of small nudges. Each nudge has a uniform probability to act in any direction. In addition, the inactive robot can either be in contact with the ring or not. This leads to a model with two random variables. The first is an angle Θ which represents the direction of an individual nudge and takes a value between 0 and 2π . The second is a binary variable β which represents whether or not the inactive robot is in contact with the ring, 1 for yes and 0 for no. A schematic of the system is shown in fig. 4.4(a). Depending on the value of these two random variables, an individual nudge can either move just the ring, just the inactive robot, or both the ring and the inactive robot.

The different types of collisions vary in how they affect the ring's movement. The collisions may be with the ring directly, with the inactive smarticle, which could either be, or not be, in contact with the ring, and which of the 3 regions of the ring (depicted in fig. 4.4) the nudge acts on. These possibilities for ring movement are summarized in table 4.1.

Table 4.1: list of all six different types of collisions which are possible in the supersmarticle theoretical model

Region	$\beta = 1$	$\beta = 0$
I	R_B	0
II	R_A	R_A
III	R_B	R_A

We use R_A to denote the distance that a nudge will displace the ring when moving only the ring, and R_B when moving both ring and inactive smarticle. Denoting the proportion of time that the inactive smarticle is in contact with the ring as λ , the frequency of nudges as f , the amount of time the supersmarticle has been moving as T , and treating each nudge as an independent event, the expected R_{\parallel} component of the average velocity of the ring is

$$\langle v_{\parallel} \rangle = \frac{f}{\pi} [\lambda(R_A - R_B)(1 - \sin(\phi)) - (1 - \lambda)R_A \sin(\phi)] \quad (4.1)$$

and the variance of the \parallel component of the average velocity of the ring is

$$\begin{aligned} \text{Var}[v_{\parallel}] = & -\frac{f}{4\pi^3 T} [\pi^2 \sin(2\phi) (R_A^2 - R_B^2 \lambda) + R_A^2 (-2(\lambda - 1) (2\lambda^2 + 1) \phi + \pi (4\lambda^2 + 2) + \pi^3 (\lambda - 2)) \\ & - 4R_A R_B \lambda (2\lambda + 1) (-\lambda\phi + \phi + \pi) - R_B^2 \lambda (6(\lambda - 1)\lambda\phi - 6\pi\lambda + 2\pi^2\phi + \pi^3) \\ & - 2(-\lambda\phi + \phi + \pi)(R_A - R_B \lambda) (4\lambda(R_A - R_B) \sin(\phi) + \cos(2\phi)(R_A - R_B \lambda))]. \end{aligned} \quad (4.2)$$

The result is simplified significantly in the R_{\perp} case:

$$\langle v_{\perp} \rangle = 0 \quad (4.3)$$

and the variance is

$$\text{Var}[v_{\perp}] = -\frac{f}{4\pi T} [R_B^2 \lambda (\pi + 2\phi) - R_A^2 (\pi (\lambda - 2) + 2\phi) + (R_A^2 - R_B^2 \lambda) \sin(2\phi)]. \quad (4.4)$$

In order to establish the relationship between the mass of the ring and its velocity, we model the active smarticles as pistons pushing on a sliding mass. We start with masses m_1 and m_2 with the relative distance between them specified by the movement of the smarticles. m_1 represents the arm of a smarticle and m_2 represents the body. The mass of the boundary they push on is m_b . Both m_2 and m_b have friction between them and the surface they are sitting on. This is shown in fig. 4.5(a). This model gives the equations of motion for x_1 and x_2

$$F_2 - f_s = m_2 \ddot{x}_2 \quad (4.5)$$

$$f_s - F_b = (m_b + m_1) \ddot{x}_1. \quad (4.6)$$

Where F_2 and F_b are the frictional force on m_2 and m_b respectively. f_s is the force between m_1 and m_2 . By specifying,

$$x_1 - x_2 = A_0 \sin(\omega t + \gamma)$$

$$F_2 = (m_2 + 2m_1)g\mu$$

$$F_b = m_b g \mu.$$

these equations can be integrated to find how far m_b moves before coming to a stop. By plugging in for m_b the mass of just the ring, and the mass of the ring plus inactive smarticle we can find R_A and R_B respectively as well as $\langle v_{\parallel, \perp} \rangle$ and $\text{Var}[v_{\parallel, \perp}]$ plotted in fig. 4.4(f).

Table 4.2: **Supersmarticle theoretical model parameters.** List of all parameters used and their values in the theoretical model

Parameter	Value
A_0	0.05 m
ω	$6\pi \frac{rad}{s}$
γ	$\pi/4$
f	5 Hz
λ	0.864
m	34.78 g
m_1	3.48 g
m_2	$m - m_1$ g
μ	0.37
ϕ	$\pi/3.8$
g	$9.81 \frac{m}{s^2}$

CHAPTER 5

SMARTICLE CHAIN

5.1 Summary

Smart materials, or materials able to respond and react to various stimuli, will likely require sensing and actuation on a local scale. We hypothesize that such materials will likely be granular in nature. To discover principles by which smart materials devised of granular particles may behave, we study a system of self-deforming controllable 3-link particles. We find that the number of entanglements, or particle interpenetrations, in an aggregate has a functional consequence: it increases resistance to tensile loading. We compare three methods of controlling entanglements in a collective. To quantify how entanglement changes fracture strength, we perform fracture tests. Finally, we use robotic three-link particles to measure a 2D analog of this experiment and find an emergent aspect of many non-convex particle fractured systems: auxetic behavior upon straining.

5.2 Introduction

In soft condensed matter systems composed of ensembles of particles, it is known that particle shape influences rheological and structural properties like viscosity [118, 119, 120], yield-stress [119, 121], and packing density [122, 123, 124, 125, 126]. Less is known about how structural properties evolve as particle shape evolves, yet we see such transitions often in nature. When we cook eggs, the albumen, mostly consisting of protein and water, changes from a viscous fluid to something more solid. Initially tightly coiled together globs of proteins begin to denature and unwind upon heating. After unwinding, they interact with neighbors and intertwine. On the macroscopic scale, this process creates an interconnected matrix between all of the protein strands, giving the mass solid-like properties. When

agents in a collective can interconnect, the collective can exhibit solid-like properties just like cooked albumen.

In past studies on externally driven “u-shaped” particles, we found we could increase entanglement by adding external energy into the system. Here entanglement is defined by interpenetration between particles in an aggregate. Such aggregations have characteristics typically associated with a solid mass rather than a granular collection[108]. For instance, such a system can support tensile loads, a property of solid systems, and a behavior not present in convex granular systems.

In this chapter, we are studying how a granular aggregate can change its material properties in situ. We draw inspiration from collective biological systems—such as colonies of ants—some of which are capable of altering their rheological behavior based on the input stimulus provided [127, 128, 129]. To learn more about emergent phenomenon resulting from such granular systems, we study a simple 3-link system, in both experiment and simulation, where the grains have 2 degrees of freedom. Using the simulation, we test how types of arm actuation contribute to the non-linear transformations of the final material properties of the collective. Finally, in experiment, we find that such a material, even in the planar system, can exhibit interesting properties.

5.3 Materials and methods

To test the material properties of these non-convex granular materials, we constructed a three-link robot in both simulation and experiment.

5.3.1 Multibody simulation of smarticles

Our simulation consisted of a multibody simulation of many staple shaped particles[108] capable of moving their outer links. The multibody simulation was implemented using a ProjectChrono [43, 42], an open source multi-physics dynamics engine. In the simulation, the model granular particle was a 3-link system see fig. 5.1(b). The size of the staples

used in the simulation were inspired from the work done previous in our lab by Nick et al. [108]. Two outer links are connected to a middle segment by rotational actuators with a single degree of freedom such that the system was planar. The middle link has a width w and the outer barbs were of length l (values given in table 5.1).

The motors controlling the outer links are velocity controlled, with a maximum allowable torque. The arms are set to move with an angular velocity of $\omega = 6$ rad/s. The maximum allowable torque τ_{max} was set to be equal to the torque necessary to lift a mass equivalent to a smarticle of $l/w = 0.7$ a distance w away from the actuator's axis. For $\tau \geq \tau_{max}$, the outer links would cease movement until the first time step when the condition $\tau < \tau_{max}$ was reached. In all simulations, the smarticles were first deposited from above into a hollow cylinder of radius $r = 2w$. During the deposition phase, all outer-links were held static such that $(\alpha_1, \alpha_2) = (90^\circ, 90^\circ)$ (see fig. 5.1(b)). After being deposited in the cylinder, activity was added to the system in one of three ways: an external sinusoidal vibration of the confining cylinder (henceforth called “shaken”), a single large angular change of each particles links (henceforth called “shape-change”), and small amplitude oscillations of the particle links (henceforth called “vibrated”).

For the externally shaken system, after the smarticles were deposited, the bucket would vibrate with $f = 30$ Hz and variable peak acceleration $\Gamma = 2$ (in units of gravitational acceleration g). The cylinder is vibrated for 20 s (600 cycles) (fig. 5.1(a)). For shape-change simulations, after smarticles were deposited, they actuated their outer-links from $(\alpha_1, \alpha_2) = (90^\circ, 90^\circ)$ to $(\alpha_1, \alpha_2) = (0^\circ, 0^\circ)$ waited for one second, actuated back to $(\alpha_1, \alpha_2) = (90^\circ, 90^\circ)$ and waited an additional second before any subsequent procedure started (fig. 5.1(b-c)). All wait times were included to allow systems to settle to a steady state. In the vibration simulations, to ensure the arc length traveled by smarticles of all l/w , after being deposited, the smarticles' outer-links would oscillate with an amplitude equivalent to the the arc length traveled by arm of length l with aspect ratio $l/w = 0.7$ an amount $\pm[5^\circ : 5^\circ : 25^\circ]$ (fig. 5.1(b,d)) from the rotational axis. This ensured for all vibration gaits,

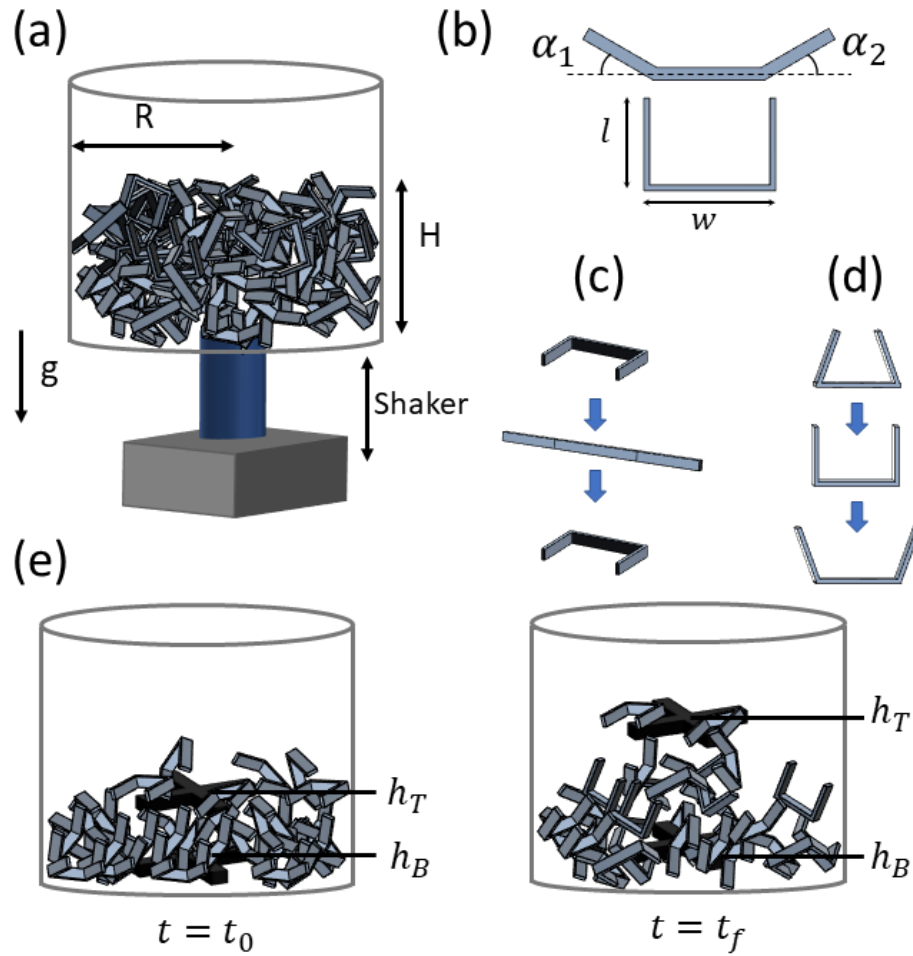


Figure 5.1: **System entanglement procedures** (a) Shaker system, particles packed within a cylinder of radius $r = 2w$. (b) The coordinate system used for the particles. (c-d) Shape-change and vibrated gait respectively. (e) Procedure for measuring force as a function of entanglement.

the arm tip traveled the same arc length for every l/w for a single vibration amplitude. The vibration phase lasts for 5 seconds before any subsequent procedures start.

The first simulation examined how entanglement changed as a function of l/w . After being deposited into an empty cylinder, the smarticles performed either the vibration, or shape-change procedure, and we measured the average number of entanglements $\langle N \rangle$. We measured the difference in $\langle N \rangle$ for a non-actuated system, the shaken system, vibrated system, and the shape-change system. $\langle N \rangle$ was determined as follows: for all particles at a specific time step, the number of links intercepting the plane defined by its own three links of a smarticle was calculated. We then calculate the average over all particles. To ascertain the efficiency of each procedure in terms of energy input and entanglement output, we measure the energy necessary to complete each procedure. This test was done for particles of varying $l/w = [0.4 - 1.1]$, and each simulation was performed 4 times for each preparation style.

To calculate the energy of the internal degrees of freedom, such as the vibrated and shape-change system, the calculation below was performed at every time step

$$E = \int_{\alpha_1(t)}^{\alpha_1(t+dt)} \tau_1 d\alpha_1 + \int_{\alpha_2(t)}^{\alpha_2(t+dt)} \tau_2 d\alpha_2 \quad (5.1)$$

where the subscripts correspond to the links numbers on each smarticle, and τ is the motor reaction torque, on each smarticle on the numbered limb, at each time step. For the shaken system, since the energy is dumped into the system externally, we sum

$$E = \int_{z(t)}^{z(t+dt)} F(t) dz \quad (5.2)$$

over each time step during the shaking process, where $F(t)$ is the reaction force on the linear actuator (which controls the height of the container with the smarticles) motor at time t , and $z(t)$ is the height traveled by the cylinder at each time-step. We removed the mass of the cylinder from the force calculation.

Table 5.1: simulation parameters used

parameter	value
w	1.17 cm
dt	2×10^{-4} s
f	30 Hz
Γ	2
ρ	7850 kg/m ³
τ	1
ω	6 rads/s
t_1	1.27 mm
t_2	0.5 mm
$\mu_{particle-wall}$	0.4
$\mu_{particle-particle}$	0.4
r	$2w$
$H_T(t_i)$	$20t_2$
$H_B(t_i)$	$10t_2$

To determine how entanglement related to the tensile loading ability, we measured the force required to raise a hook embedded in the smarticle systems fig. 5.1(e). In these simulations, two crosses, composed of perpendicular beams of cross section $t_1 \times t_1$ and length w were embedded into a pile of smarticles. After the preparation of the collective, the top cross was raised a distance, $h_T(t_f) - h_T(t_i) = 3w$ at a rate $\dot{h} = w(1/s)$. We examined the force as a function of $l/w = [0.4 - 1.1]$ fig. 5.1(a). Each simulation was performed three times.

5.3.2 Experimental system

To test some of the physical attributes of a configurable chain of non-convex granular materials we built three link robots. These robots, which we call “smarticles”, are shown in fig. 5.2(a-c). The arms are controlled by two servos (Power HD, HD-1440A) to a precision of ($< 1^\circ$) and with an accuracy of $\pm 6^\circ$. All processing and servo control is handled by an Arduino Pro Mini 328 - 3.3 V/8 MHz. The system is powered by a 3.7 V 150 mAh 30 C LiPo battery (Venom;Rathdrum, ID.).

Due to the size of the servos and the thickness of the body, the dimensions of the

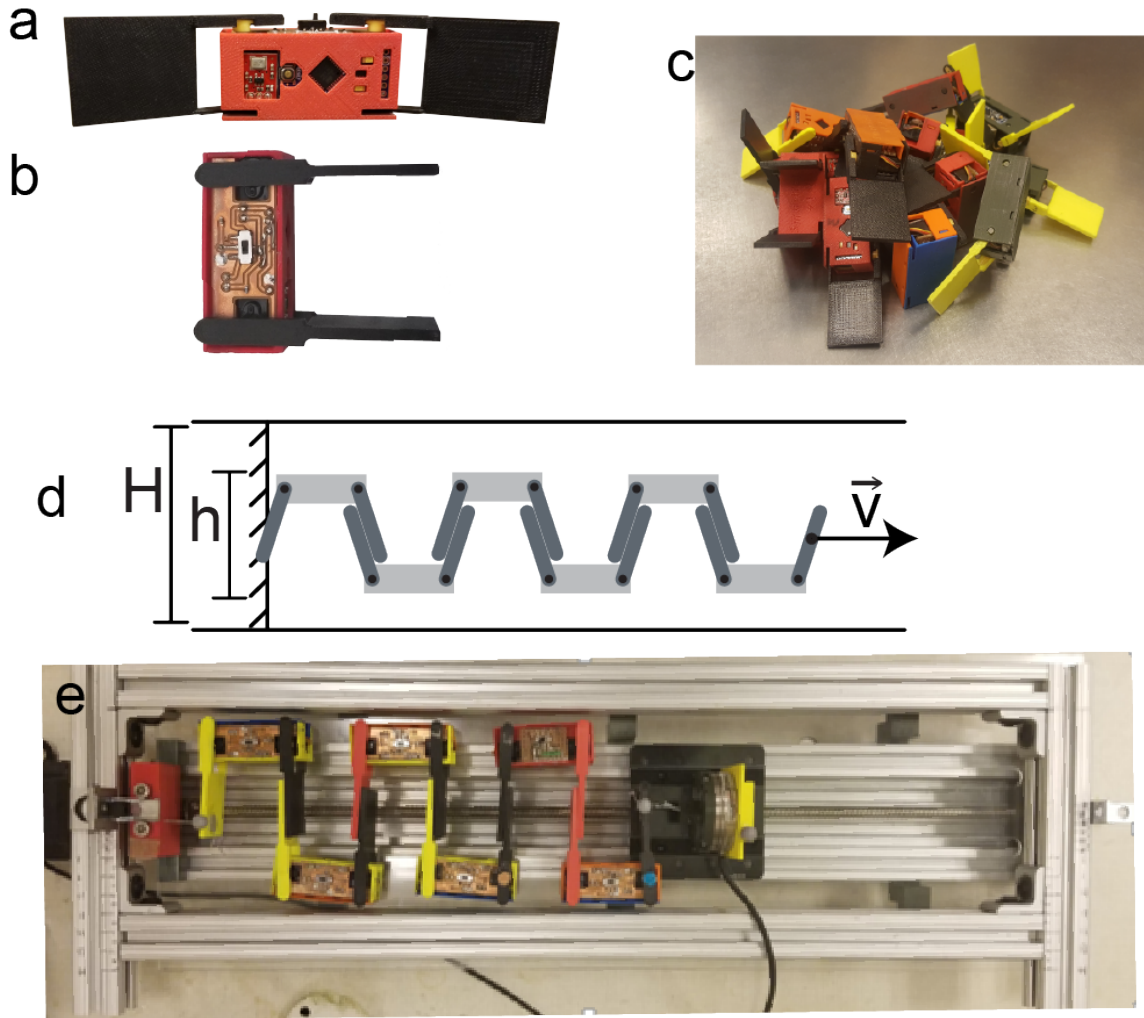


Figure 5.2: **Smarticle chain experimental setup**(a) Front view of smarticle (b) top view $w = 5.3$ cm and $l = 4.9$ cm. (c) Pile of smarticles.(d) Schematic of smarticle chain setup (e) Smarticles in a chain configuration

smarticles incapable of performing the 3D tests from the simulations in section 5.3.1; the smarticles could not reach entanglement numbers $\langle N \rangle > 2$. Despite this shortcoming, we found novel results regarding these particles in 2D tests which depend on the non-convex nature of these particles. We found that u-shaped particles when strained produce auxetic behavior, a result of their concave shape. Furthermore, the fracture of a “chain” of smarticles could be strengthened by varying the amount of confinement on the chain.

In all trials, smarticles were placed such that they were centered between the confin-

ing walls fig. 5.2(e). The positions of each smarticle in the chain were randomized between each trial, to account for any variance in the servos' strength due to manufacturing differences or general wear that may accumulate over time. Experiments are performed with two different numbers of smarticles, $n = [2, 6]$. The chains were arranged as shown in fig. 5.2(d-e) in a repeating u-n-u-n... pattern, (where an "n" is the same shape as a "u" but rotated 180°). This pattern serves to interlock adjacent smarticles together. For chains $N > 1$, stress could be transmitted between smarticles in the chain. The outer links on the ends of the chain, (the links not in contact with an adjacent smarticle) are connected via a string to a rigid structure. On one side, the chain is attached to a force sensor, and to a structure bolted to the apparatus on the other side. The force sensor was connected on the side of the chain where strain is imparted. The force sensor used was a lab built full-bridge strain-gauge, and all force measurements $F(t)$ were sampled at 1000 Hz. The strain was imparted by a slightly modified linear actuator kit (OpenBuilds; Monroeville, NJ.). All strains were performed at a strain-rate of $v = [5mm/s]$. The strain was measured by tracking infrared markers placed on the smarticles, all positions and orientations were tracked using an infrared video recording hardware/software suite (OptiTrack; Corvallis, OR).

We measured strain at fracture as a function of confinement width. In these experiments, we varied the width of the confinement h (see fig. 5.2(d)) and measured the strain before fracture. Each trial was repeated 5 times. We performed this test for two different numbers of smarticles, $n = [2, 6]$, and each trial type was repeated five times, each with different smarticle arrangements. We then changed the confinement width between the outer walls. All trials were repeated 5 times for confinement widths between $h/H = [0.52 - 0.65]$, fig. 5.2(d) and $H = 6.2cm$.

In the second experiment, the peak force before fracture (rather than the force at fracture) was measured. Trials were run with $n = [2 - 6]$ smarticles, and each trial type was repeated five times each with different smarticle arrangements. In the last trial, we mea-

sured peak force at fracture for different confinement widths.

5.4 Results and Discussion

5.4.1 Simulation

To begin the discussion of materials property differences as a function of energy usage, we start by examining the energy cost for each of these system preparations. From fig. 5.3(a), and we find that of the three methods of preparation, shape-change requires the most energy regardless of the aspect ratio. Indeed, the shape-change method requires more than an order of magnitude increase in energy than the vibrated system—the system requiring the lowest amount of energy. For the vibrated system we have only shown a single vibration amplitude for clarity. The energy required to prepare the vibrated system increases, as perhaps expected, with increasing vibration amplitude as shown in fig. 5.3(b) for a singular $l/w = 0.7$ value. With the exception of $l/w = 0.9$ as vibration amplitude increase, the energy required to perform the procedure also increases. Next, we will examine how efficient each system is at producing entanglements given we now know their energy expenditure.

In fig. 5.4(a), we measured entanglement as a function of aspect ratio for the different preparation methods. Included in fig. 5.4(a) is a preparation method with no activation, neither internal nor external, which is labeled “unshaken”. This serves as a baseline for the other methods. With the exception of the unshaken system, where entanglement is independent of aspect ratio, all active procedures that show entanglement does indeed vary as a function of l/w for all types. Furthermore, now with the exception of the shape-change system, all other entangling systems tend to peak around $l/w = [0.7 - 0.8]$ around intermediate aspect ratios. As the aspect ratio gets larger, the outer arms increase in size. An entanglement between two larger aspect ratio shapes will remain more robust to perturbations [108]. There is a trade-off: it is initially more difficult to become entangled. Interestingly, the shape-change system does not have this issue since the entangling action happens during the straight to u-shape transition. During this time, the outer-links are

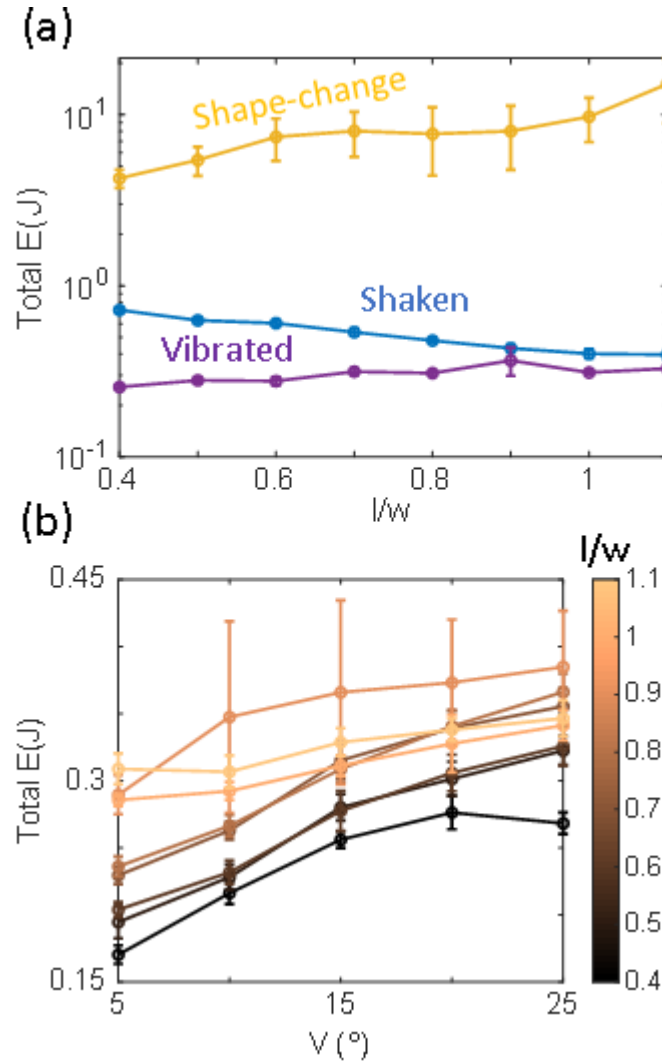


Figure 5.3: **Comparing energy usage between procedures**(a) Comparisons of energy output for different procedures as a function aspect ratio. The vibration data shown has a constant vibration amplitude of $V = 15^\circ$. All data points are averaged from three trials. (b) Energy usage increases with vibration amplitude. With the exception of $l/w = 0.9$, the energy tends to rise as a function of l/w . As vibration increases in amplitude, there is a general increase in energy usage, with the exception of the lowest amplitude $l/w = 0.4$.

not restricting possible entanglements. Larger aspect ratios actually increase likelihood of entanglements happening on the shape-change system, as the area which can allow for interpenetration is larger. Despite its excellent entanglability, it uses the most energy. The vibrated system tends to have higher entanglement despite requiring lower energy.

Now we examine how vibration amplitude and aspect ratio affect the overall number of entanglements in the vibrated system. If we look at how entanglements vary as a function of vibration amplitude $V = [5 - 25]^\circ$ for all l/w in fig. 5.4(b) we see something peculiar. As the aspect ratio increases, the functional form of the entanglement as a function of vibration amplitude changes. At low aspect ratios, $l/w = [0.4 - 0.7]$ the peak happens at $V = 10$, however as the arms get larger the peak happens later. We posit this is related to the argument stated before: at low l/w it is easier for you to become entangled, however it is also easier to become disentangled. The arms can move with too much and break the entanglements faster than new ones are generated, but if the arms are longer, the same vibration arc length traveled will not tend to disentangle an already formed connection since the energy threshold necessary to break pre-existing bonds is larger.

To get a complete picture of how the material properties are actually being affected we performed fracture tests. In fig. 5.5(a) we see that that for the trials shown for the three procedures, the peak force output and the entanglements keep the same order. When comparing the force generated as a function of vibration fig. 5.5(b) we see that there is agreement between fig. 5.4(b), the number of entanglements for a given vibration amplitude, and the force generated.

Using this simulated system, we found a connection between tensile strength through measured through a fracture test and number of entanglements to be correlated. This study also clarified the importance of preparation methods: depending on the parameter you wish to optimize (energy required or force generated) the best preparation method can vary. Next we examine emergent properties arising in a planar fracture setup in experiment.

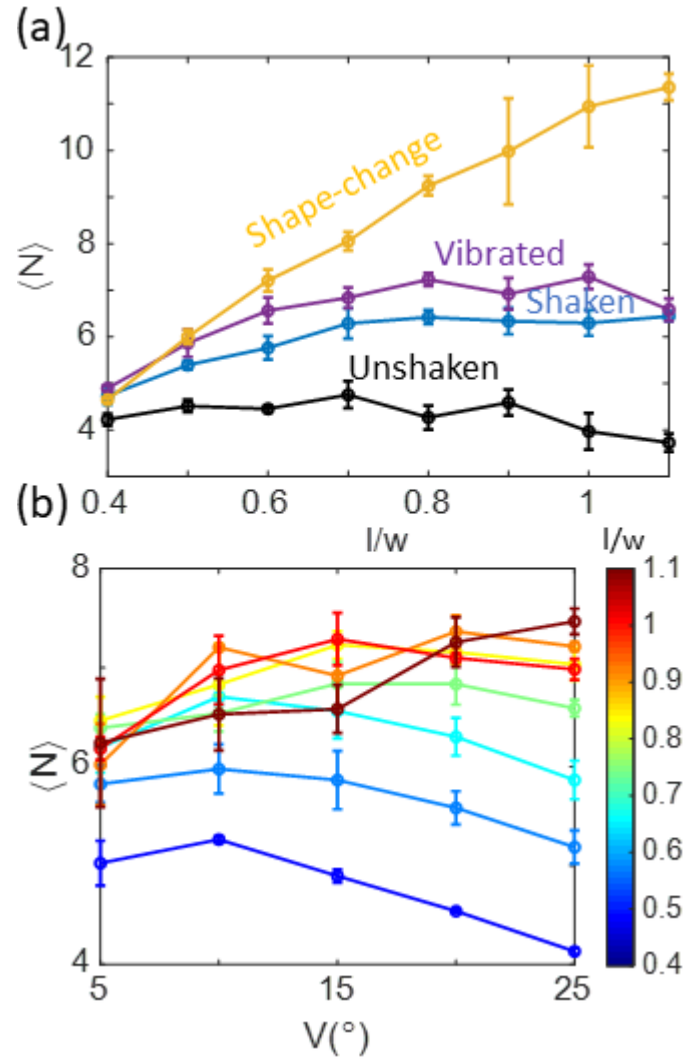


Figure 5.4: **Comparing entangling procedures** (a) Comparisons of entanglements for all procedures at various aspect ratios, each data point was the average of 3 or more trials. The vibration line is at a vibration amplitude $V = 15^\circ$. (b) Entanglement as a function of vibration amplitude, each line represents a different l/w . All data points were averaged over three or more trials

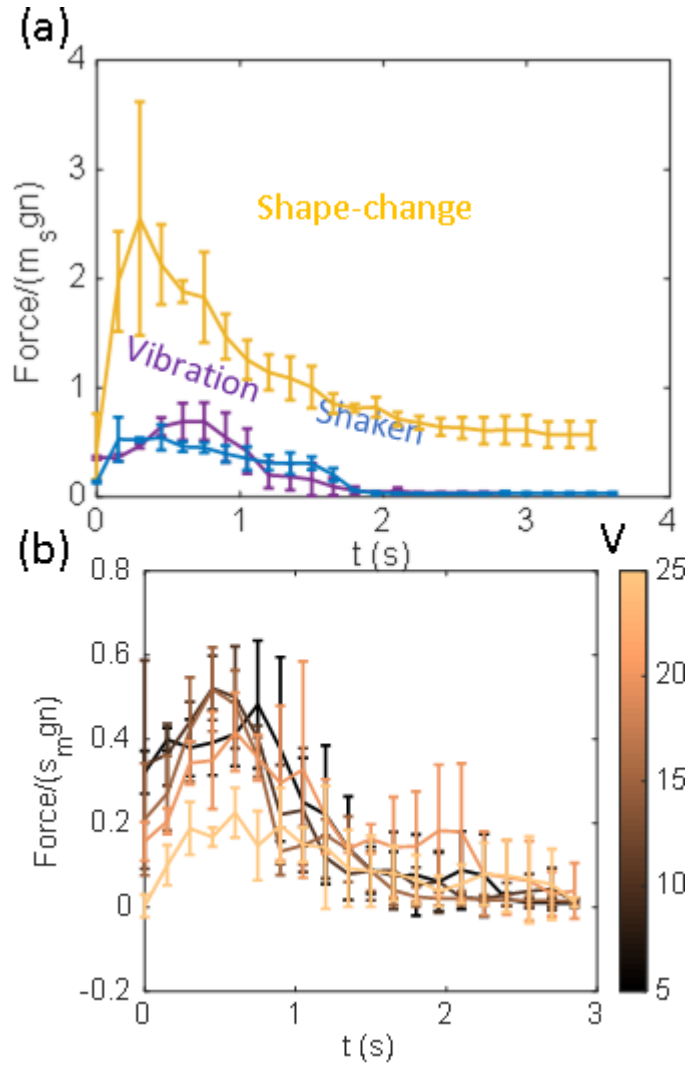


Figure 5.5: **Force versus l/w for different systems** (a) All 3 procedures were run at $l/w = 0.7$ and the force was time averaged with a window mean of 0.1 s and each line is averaged over 3 trials. (b) comparing the force versus time for the various vibration amplitudes, the $l/w = 0.4$ was chosen because of the large change in $\langle N \rangle$ as V changed (see fig. 5.4)(b) we see vibration amplitude and force generated has a general agreement with the entanglement as a function of vibration amplitude from the previous figure. Force shown here is a unitless quantity scaled by mass of smarticle m_s , gravity g , and number of smarticles n .

5.4.2 Experiment

In our first trial, we discovered an interesting emergent property of this smarticle chain fig. 5.6, as n increases, both the force and the elongation increase. If we consider the servos, which are PD controlled, like a spring, we would expect a chain of servos to act as a chain of springs: for a constant strain distance, the force would decrease.

Looking more closely at fig. 5.6, we can see a small dip at a strain of nearly 30 mm for both systems. The effect is larger in the $n = 2$ system, but it is indeed the same mechanism causing the drop. The drop in force happens because there is a sudden rapid increase in chain length. This corresponds to the yield stress, the point at which rearrangement in the chain happens, signifying it has undergone plastic deformation. After reaching this yield stress point, if performing a cyclic strain test, the force as a function of strain will produce a functionally different curve than the previous cycles before the yield point was reached.

In the chain system, the fracture mechanism is related to the arm opening angle and friction. When the smarticle chain is strained, the arms expand from their u-shape. The system fails when the expansion reaches a certain threshold and the static friction slips and the arms lose contact. As the smarticles slip, due to their geometry, they are forced to expand outwards. This expansion in the direction lateral to the strain is called auxetic behavior. For this auxetic behavior, in our system, if the smarticles do not expand to point where the arms slip and a fracture happens, they can eventually come in contact with a confining boundary. Once in contact with the confining boundary, some of the force previously supported by only the arms, is now supported by the walls, effectively reducing the load on the arms since the arms no longer need to strain as much to continue supporting the imposed strain. As shown in fig. 5.7(a). As the confinement increases, the maximal force measured before a fracture changes. That force increases linearly with the confinement fraction. Moreover, the functional form of a $n = 2$ and $n = 6$ smarticle is qualitatively similar, only the magnitude changes. We find similar results in fig. 5.7(b) for the maximum strain at fracture. As confinement increases, maximum possible strain increases as well.

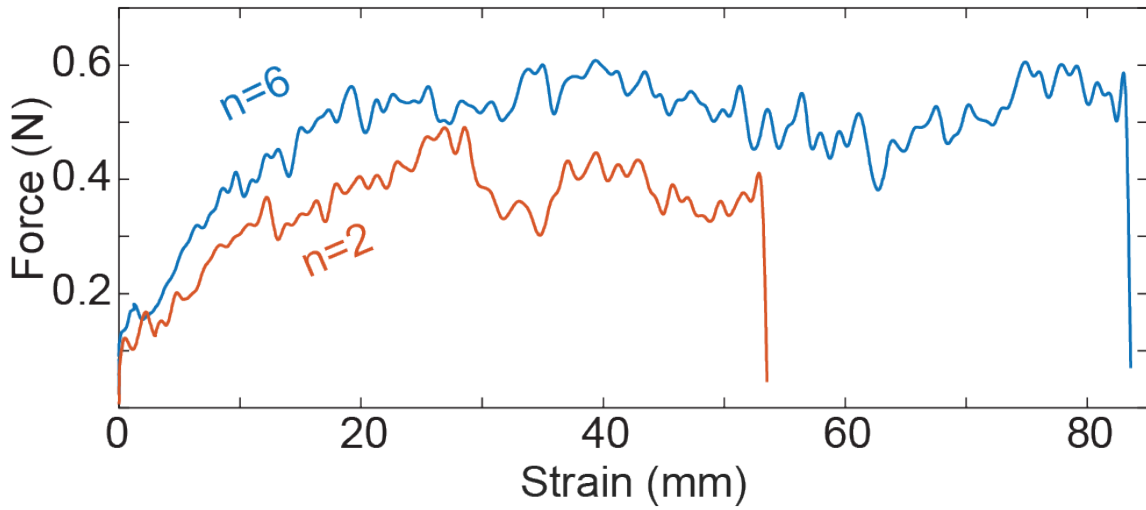


Figure 5.6: **Single fracture trial for $n=2$ and $n=6$ smarticles** Single trials of force as a function of strain for smarticle chain at different n , both strains were continued until the chain fractured.

In our smarticle system, based on smarticle cloud results from chapter 4, we hope to eventually find gaits which can reliably produce contraction as well as expansion for the smarticle cloud system. In a contracting case, for smarticles at the center of the pile experience confinement. With that as our motivation, we tested how confinement affected fracture. We found that the maximum force before fracture will steadily increase, similarly we found a similar result to be true for the maximal strain distance before fracture as well. By leveraging future capabilities of smarticle swarms we could effectively use other smarticles to enforce the confinement conditions, allow a chain to improve performance on command.

5.5 Conclusion

We have performed to our knowledge the first study of time-dependent material-properties of a non-convex granular material. Despite the seemingly complex interactions, we found

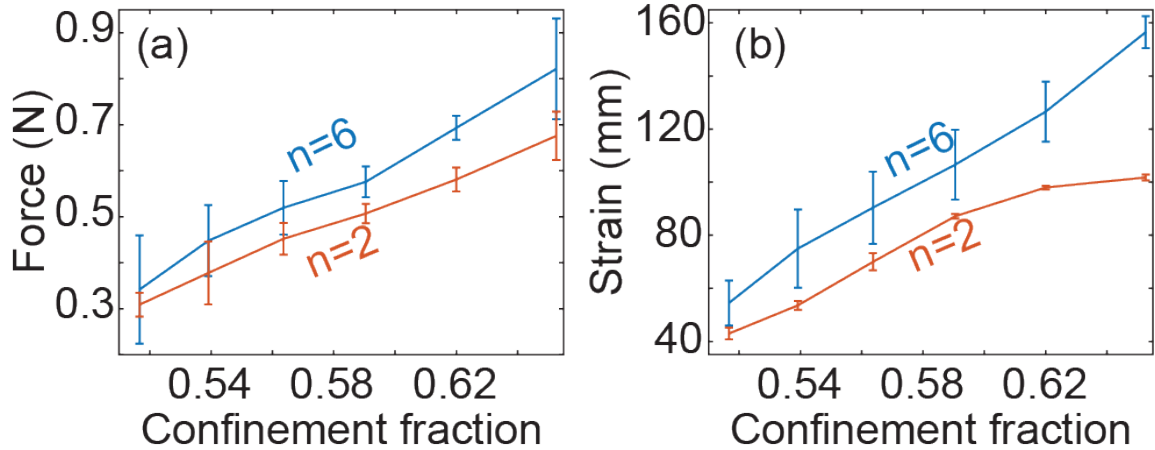


Figure 5.7: **Auxetic behavior in smarticle chain**(a) Peak force before fracture (b) peak strain before fracture.

that entanglement, which encodes much of the material properties, can be controlled. Building from what we knew from previous studies of entangleable granular materials, we found that the fracture force increased as expected as a function of how entangled a collection was in simulation. Finally we performed a 2D fracture test analogue and found emergent robotic material properties, a chain of smarticles was auxetic. Peak force measured before fracture increased as a function of confinement.

In the future, we envision a material capable of generate states of max/min entanglement in response to a stimuli (i.e. fireants raft formations in the presence of flooding [128, 129]). This entanglement response should be able to spread through the collective “organically”, or via local communication, rather than through a global or centralized mechanism. We believe that another major insight from this study is that the choice of how limbs may be activated to alter entanglement can be optimized as a function of energy cost. We posit that by improving our understanding for such systems, those with particles of constant volume but mutable shapes, it will represent a major step forward in the race towards dynamic materials[130].

CHAPTER 6

SIMULATIONS OF TRAFFIC AND WORKLOAD DISTRIBUTION IN FIRE ANT NEST CONSTRUCTION

6.1 Summary

Groups of active particles, insects or humans can form clusters that hinder the goals of the collective; therefore, the development of robust strategies for control of deleterious clusters (i.e. clogs) are essential. Our biological and robophysical experiments, supported by computational and theoretical models, reveal that substrate excavation performance can be robustly optimized within the constraints of narrow tunnels by individual idleness and retreating. Tools from the study of dense particulate ensembles elucidate how idleness reduces the frequency of flow-stopping clogs, and selective retreating reduces cluster dissolution time for the rare clusters that still occur. Our results point to strategies by which dense active matter and swarms can become task-capable without sophisticated sensing, planning and global control of the collective. *

*This chapter was adapted from part the *Science, 2018* publication titled “*Collective clog control: Optimizing traffic flow in confined biological and robophysical excavation*”

6.2 Introduction

Fire ants, *Solenopsis Invicta*, (see section 1.4.2 for more information on this species), build subterranean nests which can span 2 meters in depth and 50 meters in length [131]. There are many benefits to subterranean nests: thermoregulation [132], protection from predators and elements, a protectable location to hide and store food, and a place to rear young [133, 134, 67, 135]. It is hypothesized their excavation behaviors, which allow for rapid nests construction, are a product of their original habitat fig. 1.12(b). They originate from South American rain-forests where they face flooding conditions, requiring both rapid nest evacuation, reconstruction, and even relocation [68]. Effective nest construction is essential to fire ant colony survival.

Fire ant nests, while they provide a myriad of benefits, they also impose many constraints: confined conditions, variable tunnel conditions, non-standard footing, as well as low visibility to name a few. Firstly, the tunnels of nests are quite narrow. While the tunnel widths appear to be affected by worker size, the tunnel width is approximately two ant body widths[15]. Tunnel width size restriction ensures that at most only 2 ants can occupy a single location within a tunnel. Next, due to nest composition (soil or sand at varying wetness), and ant size variability, footholds are not well defined: events, where ants fall, are possible. It is hypothesized the narrow tunnel was arrived at through evolution as it can mitigate catastrophic falling events [68]. When an ant climbs a tunnel, in a direction nearly parallel to gravity, the ants can arrest their a potential fall by pitching their body either forwards or backward upon losing their footing [68]. Low-visibility reduces possibilities for communication. It was found in previous experiments that fire ants utilize unequal workload distributions[15], so, in this study, we will use simulation to understand why an unequal workload distribution is effective.

6.2.1 Simulated system

It is common to use simulation in the study of flocking systems [58, 57, 59] and even in ant systems. There are many different styles of simulations used, in this chapter however, we will be using a cellular automata (CA) to model ant traffic through a confined space. Stephen Wolfram, while not the original inventor, has certainly completed the most comprehensive studies of CA models [136, 137]. In [136], he beautifully introduces CA models thusly:

Cellular automata are mathematical idealizations of physical systems in which space and time are discrete, and physical quantities take on a finite set of discrete values. A cellular automaton consists of a regular uniform lattice (or “array”), usually infinite in extent, with a discrete variable at each site (“cell”). The state of a cellular automaton is completely specified by the values of the variables at each site. A cellular automaton evolves in discrete time steps, with the value of the variables at one site being affected by the values of the variables at sites in its “neighborhood” on the previous time step. The neighborhood of a site is typically taken to be the site itself and all immediately adjacent sites. The variables at each site are updated simultaneously (“synchronously”), based on the values of the variables in their neighborhood at the preceding time step, and according to a definite set of “local rules.”

CA models have been used to model many granular systems studying avalanching, [138], sand piles formation[139], the formation of sand ripples for sand blown by the wind [140, 141], density inhomogeneities which arise in granular pipe flow [37], and perhaps most relevant to model ant bi-directional traffic flow[142]

6.3 Materials and methods

We used a cellular automata model (CA) to elucidate the effects of collective actions on traffic during tunnel construction. Our CA model follows most of the assumptions Wolfram laid out, with a few exceptions. Firstly, we will be using a non-infinite space, and as a result, there are boundary interactions. Next, the state of the sites representing the entry point depends not only on neighbors but on an external probability to enter the tunnel (or lattice) if the state is on the previous step represented by an empty square. Finally, the CA is not perfectly synchronous, at each discrete time step, each cell is updated one by one, but the order is randomized at each new timestep.

In a rectangular tunnel lattice, each cell can take one of four possible states: soil, empty/excavated space, ascending excavator, and descending excavator. The initial conditions of the simulation included the number n of ants excavating in a group each with body length, BL , and body width, BW , as well as the width of the tunnel (W_T), the initial length of the tunnel, and the protocol of social organization of the group. At every simulation step, the ant was characterized by its 2D position (x, y) , the direction of motion, whether or not they were carrying a pellet, and probability P to return back to the tunnel after pellet deposition.

The state of the cells in the model changed by a discrete time step according to simple rules. At each iteration step, ants located in the tunnel progressed (“walked”) one cell forward or diagonally forward with a probability p unless the destination cell was occupied. This probability affected the duration of ant clusters and was chosen from experimental observations [142]. Also, when in a cluster, a descending ant has a probability to turn back and exit the tunnel without excavation (“reversal”). Due to the geometrical constraints of the CA model, the reversal behavior was essential to prevent jamming for infinitely long times for populations $n > 2W_T/BW$. In the absence of the reversal behavior, unresolvable clogs consisting of $n \geq 2W_T/BW$ ants can form, spanning the width of the tunnel and

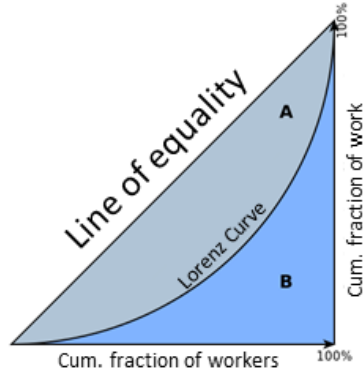


Figure 6.1: **Lorenz curve and Gini coefficient.** The Gini coefficient is calculated by determining first area in regions A and B, and $G = \frac{A}{A+B}$. Figure was altered from its original source https://en.wikipedia.org/wiki/Lorenz_curve

disrupting the excavation process. Thus, reversal behavior was implemented for all CA simulations regardless of workload distribution.

When an ant reached the tip of the tunnel, it spent several time steps excavating, motivated from experimental observations on digging time[16]. The excavated pellet was transported to the entrance of the tunnel and expelled from the tunnel (“pellet deposition”). After a predefined number of pellets were collected from a site the tunnel grew in length by one cell as the state of the soil cell changed to an empty cell. After returning to the tunnel entrance and exiting the system, the ant deposits the pellet. After pellet deposition, the ant would return to the tunnel with probability P or switch to resting mode. During the pellet deposition or resting mode, the ant was neither contributing to the excavation, able to cause clogs, nor increasing tunnel density. The exit from the resting mode was also defined by probability P .

The unequal workload distribution was achieved by introducing the probability, P , to return to excavate in the tunnel after a pellet deposition. To simulate fully active ants, workers attempted to reenter the tunnel immediately after pellet deposition ($P = 1$). In groups with unequal workload distributions, the probability of an ant to return to the tunnel was unique, fixed, and derived from the experimental ant workload distribution measurements

as

$$P\left(\frac{n_i}{n}\right) = f\left(\frac{n_i}{n}\right) - f\left(\frac{n_{i-1}}{n}\right) \quad (6.1)$$

where n_i was the number of ants in a sequence from the least to the most active; n was the excavating group size, and f was a Lorenz function. The Lorenz function relates the cumulative fractions of workers in the population (sorted from least active to most active) to the cumulative fraction of work performed by those same ants. The Lorenz function here was taken from the experiment. To characterize the Lorenz distributions, we calculated the Gini coefficient G , defined as the ratio of the area under the line of equality as shown in fig. 6.1. The use of the Lorenz function, and Gini coefficient, to evaluate and classify differences in workload distribution was motivated by prior studies [143].

Parameters describing ant behaviors were found via experimental observation. The only parameter varied to allow the system to match the experiment were the excavations to grow tunnel size by one cell. The rates were calculated from the slope of the tangential lines fitting the initial portion of the tunnel growth curve. The tunnel excavation rates in simulations could differ greatly depending on excavation scenario. In general, the groups of active diggers ($P = 1$) were most efficient, in energy and excavation rate, when the number of excavators in the group was small. The increase in the number of active excavators led to the formation of ant clusters, which eventually slowed the nest construction down. The unequal workload distribution $P\left(\frac{n_i}{n}\right)$ in large groups of excavators allowed for the reduction of ants density in the tunnel throughout the experiment and, thus, produced high nest construction rates even when the number of diggers in the excavating group was large. In large groups of diggers with unequal workload distributions, the excavation rates were insensitive to the addition of excavators.

The CA simulations were carried out for ant groups of different sizes. The width-normalized ant occupancy and the flux were measured in $L_T = 5$ cell long tunnel (2.5 cm actual length). The flux and occupancy were measured at $i = \text{Floor}(L_T/2) + 1$ position in the simulated tunnel fig. 6.2. We calculate ant occupancy as the time-averaged number of

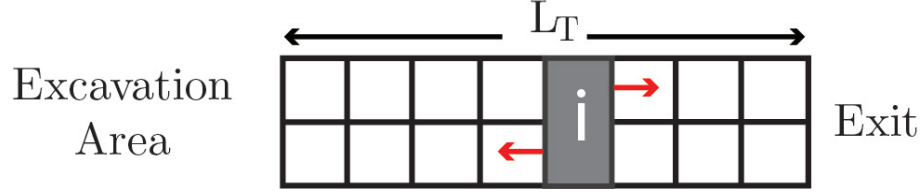


Figure 6.2: **Schematic of the tunnel in CA.** The occupancy of ants and the flux in the tunnel were measured at the highlighted cell i . The possible directions of ant motion are shown with red arrows.

ants in the tunnel divided by the tunnel width, W_T , in ant body widths, BW :

$$\bar{\lambda} = \frac{1}{T} \sum_{t=1}^T \frac{n_i(t)}{W_T} \quad (6.2)$$

where $n_i(t) = 1$ if the site is occupied at time t and 0 otherwise. Occupancy at a fixed site i was averaged over a time period $T = 3$ hours. The average bi-directional flux \bar{q}^T between site i and neighboring sites $i + 1$ and $i - 1$ was defined as

$$\bar{q} = \frac{1}{T} \sum_{t=1}^T \frac{n_{i,i+1}(t) + n_{i,i-1}(t)}{W_T} \quad (6.3)$$

where $n_{i,i+1}(t) = 1$, if the ant moved between sites i and $i + 1$, and $n_{i,i-1}(t) = 1$ if the motion occurred between i and $i - 1$, and zero if the motion was not detected. The flux was averaged over time T corresponding to 3 hours of experiment. The flux was normalized by the tunnel width. We introduced these definitions to compare traffic in groups of different sizes governed both equal and unequal workload distributions.

The implementation of unequal workload distribution reduces the immediate density of the ants in the tunnel in simulations. As a result, the number of clusters (I_c), their spatial extension (a_n) and time duration (T_c), as well as the number of ants involved in the clogs C decrease, allowing for stable traffic formation fig. 6.3.

To analyze traffic, a clog was defined as agglomerations of 2 or more ants located in the neighboring cells at a simulation step k . The number of clusters was defined as the total number of agglomerations observed over 50,000 simulation steps. Each simulation

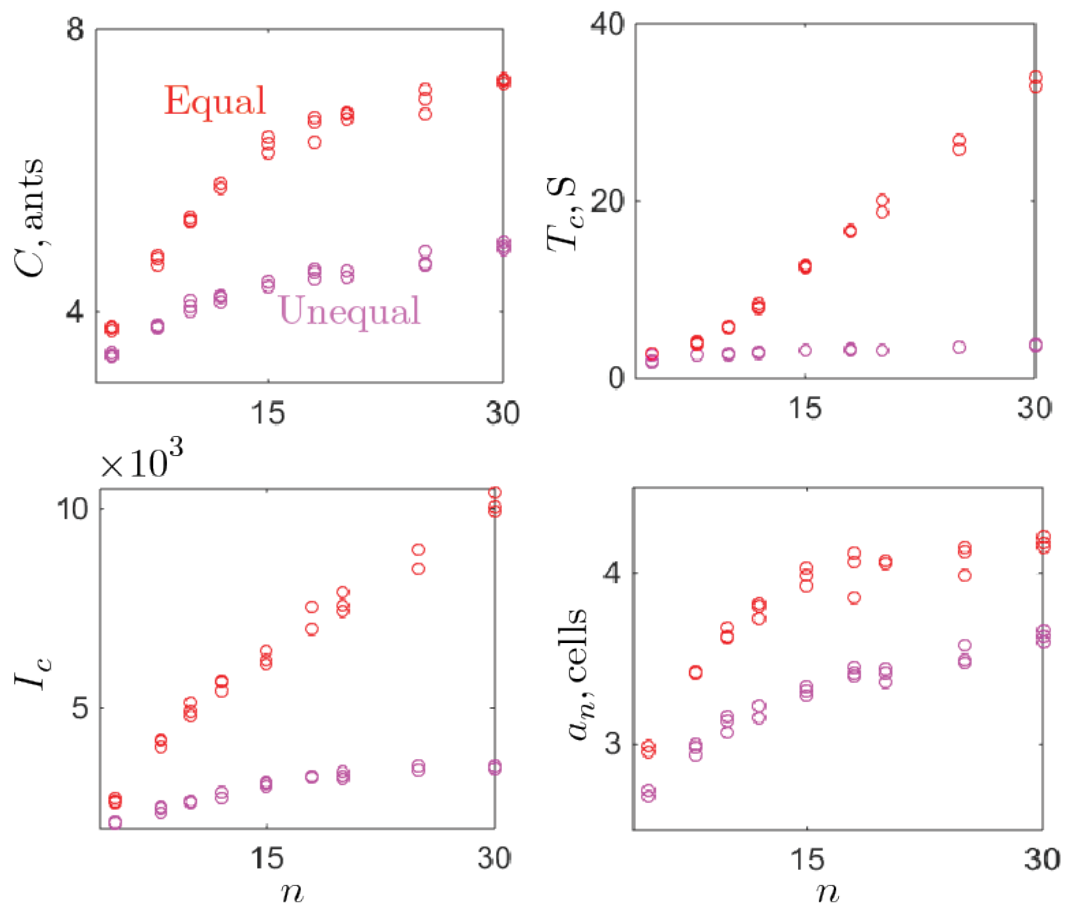


Figure 6.3: **Average number of ants involved in a clog C in simulation**(a), site occupancy time T_c (b), total number of clogs I_c over 50000 simulation steps (c), and average spatial extension of the clog a_n (d) plotted versus the size of the group for groups governed by equal workload distribution (red) and unequal workload distribution protocols (magenta).

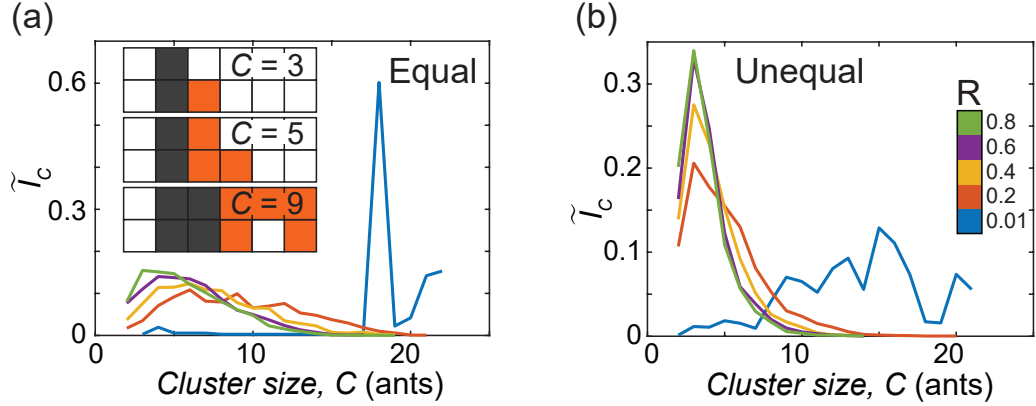


Figure 6.4: **Ant cluster analysis** Proportional number of CA ant clusters, $\tilde{I}_C = \frac{I_C}{I_{total}}$, of different sizes, C , measured over 24 hours for (a) equal and (b) unequal (optimized for 30 CA ants). Workload distributions at different reversal probabilities R (blue: 0.01, red: 0.2, yellow: 0.4, purple: 0.6, green: 0.8). Sample illustrations for different cluster sizes in (a) inset.

step was considered independently. The site occupancy time T_c was defined as the time it takes for a particular cell occupied by an ant involved in a clog to change its value from “occupied” to “vacant”. The average spatial extension of the clog was defined as the number of cells occupied by the ants sequentially along the tunnel length. The number of ants involved in a cluster, the cite occupancy time and the spatial extension of a clog were averaged over all simulation steps and results are reported on fig. 6.3.

We characterized how cluster severity was affected by reversals and unequal workload distributions through an analysis of cluster formation. Clusters in 30-ant simulations were identified at each simulation time point and categorized by the number of CA ants that comprised the cluster. Any group of ants that blocked the entire tunnel width was considered a cluster. We found a prevalence of large clusters for extremely low reversal probabilities in both equal fig. 6.4(a) and unequal fig. 6.4(b) workload distributions. A minimal increase in reversal probability reduced the prevalence of the largest clusters from forming. However, even accounting for higher reversal probabilities, equal workload distributions resulted in the wider distribution of cluster sizes, whereas the optimized workload distribution produced a sharper concentration of small clusters, which were more easily dispersed. Thus,

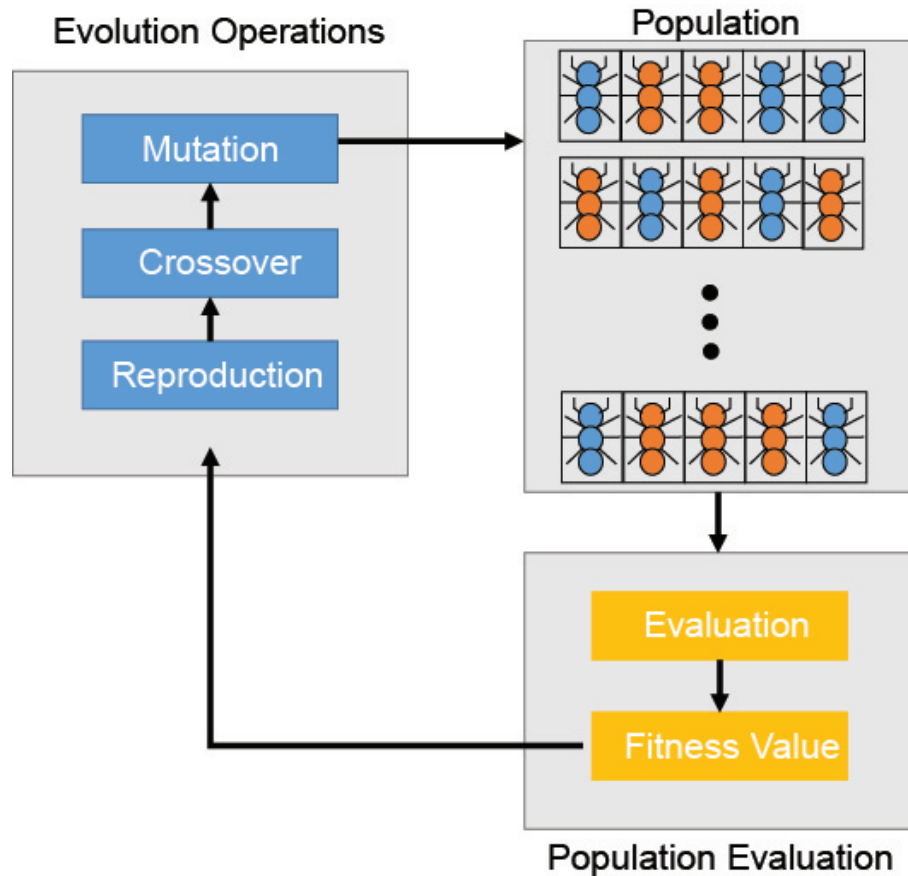


Figure 6.5: **Diagram illustration of genetic algorithm**

cluster mitigation is most effective using both reversals and unequal work probabilities in combination.

A genetic algorithm (GA) was used to search for entrance probability distributions that produced maximal digging rates. The GA is a biologically inspired optimization technique used typically to find solutions where the parameter space is large. GAs modify or evolve populations of solutions at each generation, through processes known as reproduction and mutation, towards the optimal solution fig. 6.5. Each probability distribution for a single simulation is known as a “chromosome”, and each probability for a single ant are called “genes”. The set of all chromosomes at each generation is called a population. The reproduction phase requires each chromosome to be run, and depending on the on the output of the objective function, the metric by which each chromosome is measured, certain chro-

mosomes are selected to be parents for the next generation. Our implementation used the digging rate as the objective function. The best performing chromosomes, known as the elite percent go unchanged to the next generation. The rest of the chromosomes are paired up, and a percentage, known as crossover percentage, are crossed over. Crossover is where a random site is chosen along the length of a chromosome and the genes of the paired chromosomes are switched around that point. After crossover, all genes belonging to the non-elite group of chromosomes have a chance, known as mutation probability, to be assigned a new random value. This helps to mitigate the chances of becoming stuck in local minima (or maxima) of the optimized quantity.

We used MATLAB's genetic algorithm toolbox [144]. Our selection type was the default used in MATLAB GA toolbox, stochastic uniform. The specific values for our reproduction and mutation rates were as follows: 5% for the elite selection, 0% for the crossover fraction, and a variable number of genes were subjected to mutation according to an adaptable mutation rate, the default option for MATLAB. We used a population size of 200 probability distributions per generation and ran 50 generations.

6.4 Results and discussion

We simulated the behavior of CA ants using both equal workload distributions (which we refer to as "Active" CA ants) and unequal workload distributions (which we refer to as "Lorenz" CA ants) with identical reversal probabilities. In unequal workload distributions, individual CA ants were assigned individual "entrance probabilities" defined as the probability of a CA ant to enter the tunnel. The initial entrance probability distribution for the 30 CA ants was taken from the biological distribution. Output workload distributions of CA simulations closely matched the input entrance probability distributions (as measured by the Gini coefficient, fig. 6.6). During a time-step, if its path towards the excavation area was blocked, a CA ant would reverse direction towards the exit with a probability ($R = 0.34$); R was set by the proportion of total reversal events observed in $W = 0.01$ soil

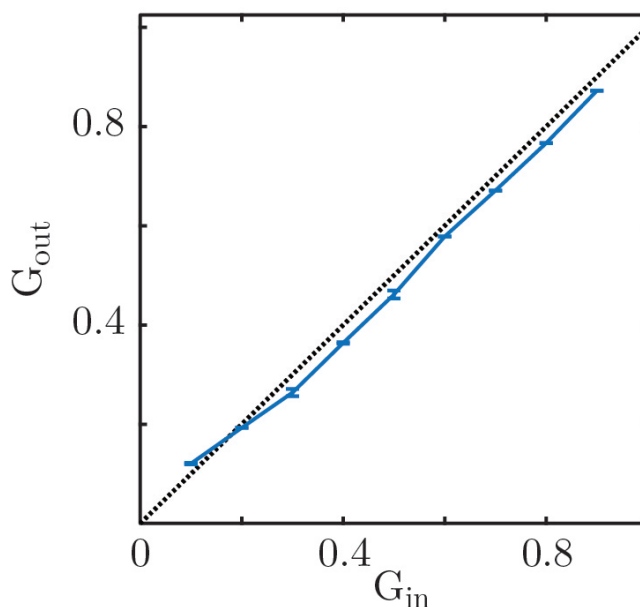


Figure 6.6: **Measured Gini coefficient versus assigned Gini coefficient** We assigned probabilities (G_{in}) and measure the actual resultant output for the system G_{out} for system where initial tunnel length $L = 5 BL$, with 30 ants digging for 24 hours. Each point is mean of 5 simulations with error bars shown.

moisture in the biological experiments.

The CA model using unequal workload distribution and reversals reproduced experimentally observed biological ant digging rates fig. 6.7(b). To determine if these rates represented an optimal workload distribution, we used the GA fig. 6.5 to select for entrance probability distributions that maximized excavated tunnel length within a given duration. Regardless of the initial population distribution (either similar to the ants or highly unequal), within a few generations the GA simulation converged to an unequal workload distribution (fig. 6.8(b) for a 30-ant example) which was similar to the experimentally observed biological workload distributions (fig. 6.7(d), green).

The CA model also revealed the importance of reversal behavior in conjunction with unequal workload distributions. While the Active excavation could be improved by sufficient reversal probability, only a small amount of reversal was needed to increase the excavation performance in the unequal distribution (fig. 6.8(d)). Thus, in addition to the

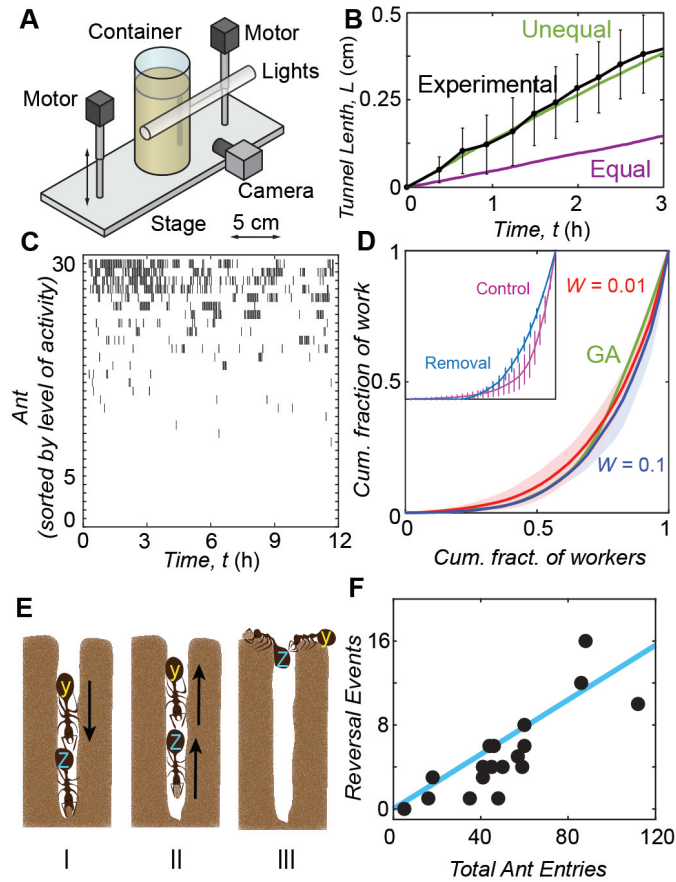


Figure 6.7: **Ant experimental results and CA calibration** (A) Experimental apparatus to track ant excavation; container inner diameter is 5.21 cm. (B) The growth of tunnel length over time: average experimental results \pm SD/2 for *S. invicta* workers (black) and simulations for groups with equal (purple) and unequal (green) workload distribution. Error bars denote 1 standard deviation in each direction. (C) “Visitation” map derived from experimental data. Each point in the map indicates the presence of a particular ant (out of 30 ants) ordered from most active to least active (y axis) in the tunnel at a time t . (moisture content of $W = 0.1$) (D) Lorenz curves for workload distributions obtained in wet 0.25 mm diameter glass particles with moisture content of $W = 0.1$ (blue) and $W = 0.01$ (red), and a CA-model (green) whose excavation rate was optimized with a genetic algorithm (GA). Shaded areas correspond to standard deviation from 3 experiments. (Inset) Average Lorenz curves \pm SD/2 for a workload distribution within the group before (control, purple) and after (repeat, blue) the most active diggers are removed from the group. Error bars correspond to standard deviations from 3 experiments. (E) Illustration of observed reversal behavior. (I) Ant Y’s path to excavate is blocked by ant Z. (II) After Z collects a pellet, it reverses, (III) forcing Y to reverse without excavating. (F) Total number of reversal events vs total ant visitors for first 3 hours of ant excavation. (moisture content of $W = 0.1$) Each data point represents total reversal events and total entries counted for 30 min segments collected from 3 experiments. Linear fit (blue line) with $R^2 = 0.69$. All experimental ant data was taken by Dr. Daria Monaenkova

benefits narrow tunnels provide for climbing and pellet transport [68, 145], we hypothesize that the ants benefit from narrow tunnels by expending less energy to dig deeper, useful for nest construction.

To gain insight into other benefits and constraints set by such narrow tunnels, we simulated using the CA a system with 30 ants and varied workload distributions (characterized by distinct Gini coefficients) in tunnels of different widths. These distributions were created through a randomized Monte-Carlo process such that the Lorenz curves resulted in desired Gini coefficients. A peak in excavated length, L , vs. Gini coefficient was observed in a tunnel 2 cells wide (fig. 6.8(c)). Wider tunnels (3 and 4 cells) resulted in broader performance peaks, indicating a decreased sensitivity in performance due to workload distribution. This indicates that use of a narrow tunnel necessitates the “discovery” of the unequal workload distribution of ants.

We hypothesized that the unequal workload distribution and reversals were linked to the uniform flow of CA ants in the tunnel. We, therefore, measured the average flow rate of successful excavators, \bar{q} , vs the average tunnel-width normalized occupancy of excavators, $\bar{\lambda}$, (the ratio of an average number of ants in the tunnel to tunnel width measured in ant body widths). To generate a wide range of average occupancies, we varied the population size of the CA system.

The flow rate was optimal at an intermediate occupancy (fig. 6.8(e)). This non-monotonic trend in \bar{q} vs $\bar{\lambda}$ is characteristic of various multi-agent systems including bridge-building army ants [146] and vehicle traffic [147, 148] and is referred to in traffic literature as the “fundamental diagram” [149]. Active ants, which do not modulate their workload distribution, increase tunnel occupancy with increasing population and thus exhibit optimal flow rates for only a few population sizes. In contrast, GA-optimized Lorenz ants produced tunnel occupancies in the ideal range by generating increasingly unequal workload distributions for increasing CA ant population sizes. Of particular importance, fire ants produced tunnel densities in the ideal range (fig. 6.8(e), shaded orange region).

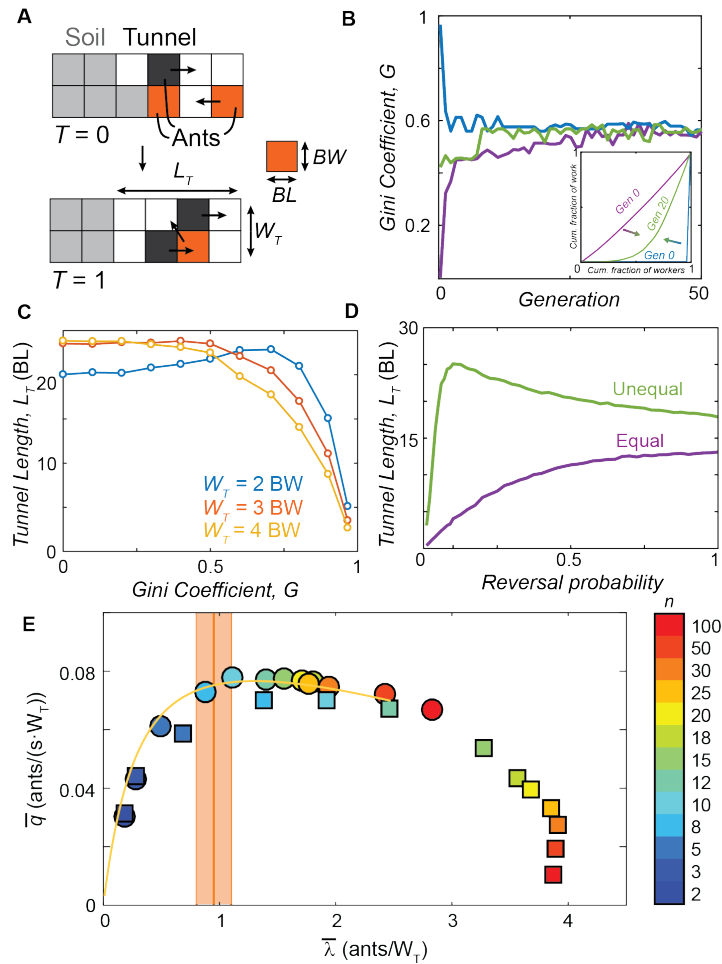


Figure 6.8: **GA applied to CA** (A) Schematic showing the main components of cellular automata model. Cell colors denote soil (light grey), tunnel (white), ants moving towards the excavation site (orange) and exiting the tunnel (dark grey). (B) Gini coefficient over time under genetic algorithm optimization. for groups started with a completely equal (purple), completely unequal (blue) and random (green) workload distribution. Lorenz curves (inset) for groups that begin with complete equality or inequality rapidly reach a similar workload distribution. (C) Excavated tunnel length, L , after 24-hour simulation time vs. Gini coefficient for tunnels of different widths for 30 CA ant population. (D) Excavated tunnel length after 24-hour simulation time vs. reversal probability for equal and unequal (optimized for 30 CA ants) workload distributions. (E) Simulated traffic flow (\bar{q}) versus CA ant occupancy ($\bar{\lambda}$ number of ants / tunnel width, W_T , in excavator body widths, BW) for groups of equally (squares) and unequally (circles) active ants. Color bar indicates the size of the excavating group. The theoretical fundamental diagram of the OAT model (yellow curve) illustrates the need to limit tunnel traffic to one worker per body width of tunnel width to optimize flow and prevent deleterious clogs. Experimental ant observations reveal an average occurrence around this density (shaded orange region, where, the orange center line is the mean, and the extents are one standard deviation away from the mean). All experimental ant data was taken by Dr. Daria Monaenkova.

The ability of the ants to operate at the optimum in the fundamental diagram and the rapidity by which the GA model converges (fig. 6.8(b)) indicates the existence of a simple governing principle for traffic control in confined task-oriented systems. To elucidate this principle, a minimal model of ant traffic in the narrowest (single-lane) tunnel: the one-at-a-time (OAT) model was formulated [16]. The model, which builds on recent work on traffic of motor proteins on microtubules [150], allows us to estimate analytically how the excavation rate varies with the rate of ants entering the tunnel for various work distribution strategies.

6.5 Conclusion

Based on prior experimental data, we found that the workload distribution in tunnel excavation was highly skewed. To probe the reason for such a workload disparity, we used a CA simulation, coupled with a robotic ant system, and found traffic flow was optimal with an intermediate occupancy of excavators, $\bar{\lambda} = N_T/W_T$, where N_T is the number of ants in the tunnel area averaged across all simulation steps and W_T is the width of the tunnel. Indeed, the peak we found in our CA simulation falls within the values the ants typically perform at. Furthermore, despite the biological and mechanical aspects mentioned previously for having narrow tunnels, we have shown that the narrow tunnels may have facilitated the “discovery” of optimal workload distributions expansion we see in the fire ant system.

6.6 Appendix

Table 6.1: **Parameters for CA Simulation**

Time step, (dt)	0.5 s
Ant size	1 cell
Tunnel Width (w)	2 cells
Reversal Probability (R)	0.34
Sim length	172800 steps (24 hrs)
Time to drop pellet	20 steps
Probability to move sideways (p)	0.52
Probability to move forwards	1
Excavations to grow tunnel size by 1 cell	200
Rest time	600 steps

CHAPTER 7

CONCLUSION

7.1 General Remarks

In this dissertation we have examined how shape and coordination affect the dynamics of granular systems. In chapter 2 A fully automated scallop robotic system was created to systematically study effect of ϕ on reversibility for a reciprocal granular swimmer. These experiments revealed that granular systems exhibit a bifurcation in the displacement response upon the first stroke. All states lose memory of initial ϕ , asymptoting to the behavior corresponding to a $\phi = \phi_c$ system. From our studies of the scallop robot in a less frictional granular system, we found that swimmers exhibit a higher degree of reversibility at larger burial depths, resulting from surface state destruction and hill and valley formation. For geometric mechanics to approach to work in a granular system the swimmer must be deep below surface, or ensure surface formations from previous strokes do not affect the dynamics of subsequent movements.

In chapter 3, a smarticle walker, and an automated setup was used to measure crawling efficacy as a function of limb size and gait length for two specific gaits. We then adapted geometric mechanics to a hybrid dynamical system. To our knowledge this was the first adaption to this type of system. We found, quite surprisingly, good agreement between the theory and a simulated system, as well as qualitative agreement with the experimental system.

We found in chapter 4, initially on accident, that a group of smarticles, who on their own are incapable of translating or rotating, can be coordinated to produce movement, by performing shape changes. A cloud was shown to displayed a transient drift and diffusion of the center of mass. By enclosing the system in an unanchored ring, the collective could

achieve stable drifts. This drift could be controlled by coordinating a single other particle in a specific way. A statistical model, developed by collaborators, accurately described the direction of motion of the ring as a function of mass ratio of the inactive particles mass to the ring's mass. The model pointed towards methods to steer the supersmarticle. We implemented such control via exogenous and endogenous phototaxis.

In chapter 5 we studied the rheology of chains. We tested how to change the material properties of a system of active non-convex granular smarticles. Using simulation, we varied the properties of the individual grains, how they were activated and their geometry and found it affected how entangled the collection of particles was. The level of entanglement was related to how difficult it was to fracture a group of smarticles, thereby affecting the system rheology. Using our experimental realization of these smarticles, we found emergent robotic material properties from a 2D fracture analogue to the simulation.

REFERENCES

- [1] H. M. Jaeger, S. R. Nagel, and R. P. Behringer, “Granular solids, liquids, and gases,” *Rev. Mod. Phys.*, vol. 68, pp. 1259–1273, 4 Oct. 1996.
- [2] P. G. de Gennes, “Granular matter: A tentative view,” *Rev. Mod. Phys.*, vol. 71, S374–S382, 2 Mar. 1999.
- [3] J. Ottino, “Sands, powders, and grains: An introduction to the physics of granular materials, by jacques duran; and pattern formation in granular materials, by gerald h. ristow,” *Journal of Fluid Mechanics*, vol. 419, pp. 345–347, 2000, Type: Review.
- [4] H. M. Jaegar and S. R. Nagel, “Physics of the granular state,” *Science*, vol. 255, no. 5051, pp. 1523–1531, 1992. eprint: <http://science.sciencemag.org/content/255/5051/1523.full.pdf>.
- [5] R. M. Nedderman, *Statics and Kinematics of Granular Materials*. Cambridge University Press, 1992.
- [6] L. E. Silbert, D. Ertas, G. S. Grest, T. C. Halsey, and D. Levine, “Analogies between granular jamming and the liquid-glass transition,” *Physical Review E*, vol. 65, no. 5, p. 051 307, 2002.
- [7] T. Majmudar, M Sperl, S. Luding, and R. P. Behringer, “Jamming transition in granular systems,” *Physical review letters*, vol. 98, no. 5, p. 058 001, 2007.
- [8] A Tordesillas, “Force chain buckling, unjamming transitions and shear banding in dense granular assemblies,” *Philosophical Magazine*, vol. 87, no. 32, pp. 4987–5016, 2007.
- [9] K. Sakaie, D. Fenistein, T. J. Carroll, M. van Hecke, and P. Umbanhowar, “Mr imaging of reynolds dilatancy in the bulk of smooth granular flows,” *EPL (Europhysics Letters)*, vol. 84, no. 3, p. 38 001, 2008.
- [10] J. Bourgeois and S. C. Goldstein, “Distributed intelligent mems: Progresses and perspectives,” *IEEE Systems Journal*, vol. 9, no. 3, pp. 1057–1068, 2015.
- [11] M. Rubenstein, A. Cornejo, and R. Nagpal, “Programmable self-assembly in a thousand-robot swarm,” *Science*, vol. 345, no. 6198, pp. 795–799, 2014.

- [12] R. Sharma and D Ghose, “Collision avoidance between uav clusters using swarm intelligence techniques,” *International Journal of Systems Science*, vol. 40, no. 5, pp. 521–538, 2009.
- [13] T. M. Blackwell and P. J. Bentley, “Dynamic search with charged swarms,” in *Proceedings of the 4th Annual Conference on Genetic and Evolutionary Computation*, Morgan Kaufmann Publishers Inc., 2002, pp. 19–26.
- [14] A. J. Calise and D. Preston, “Swarming/flocking and collision avoidance for mass airdrop of autonomous guided parafoils,” *Journal of guidance, control, and dynamics*, vol. 31, no. 4, pp. 1123–1132, 2008.
- [15] N. Gravish, M. Garcia, N. Mazouchova, L. Levy, P. B. Umbanhowar, M. A. D. Goodisman, and D. I. Goldman, “Effects of worker size on the dynamics of fire ant tunnel construction,” *Journal of The Royal Society Interface*, vol. 9, no. 77, pp. 3312–3322, 2012.
- [16] J. Aguilar, D. Monaenkova, V. Linevich, W. Savoie, B. Dutta, H.-S. Kuan, M. D. Betterton, M. A. D. Goodisman, and D. I. Goldman, “Collective clog control: Optimizing traffic flow in confined biological and robophysical excavation,” *Science*, vol. 361, no. 6403, pp. 672–677, 2018. eprint: <http://science.sciencemag.org/content/361/6403/672.full.pdf>.
- [17] E. M. Purcell, “Life at low reynolds number,” *American Journal of Physics*, vol. 45, no. 1, pp. 3–11, 1977.
- [18] A. Shapere and F. Wilczek, “Geometry of self-propulsion at low reynolds number,” *Journal of Fluid Mechanics*, vol. 198, 557–585, 1989.
- [19] Y. Ding, S. S. Sharpe, A. Masse, and D. I. Goldman, “Mechanics of undulatory swimming in a frictional fluid,” *PLOS Computational Biology*, vol. 8, no. 12, pp. 1–13, Dec. 2012.
- [20] R. L. Hatton and H. Choset, “Geometric motion planning: The local connection, stokes’ theorem, and the importance of coordinate choice,” *The International Journal of Robotics Research*, vol. 30, no. 8, pp. 988–1014, 2011. eprint: <https://doi.org/10.1177/0278364910394392>.
- [21] B. McInroe, H. C. Astley, C. Gong, S. M. Kawano, P. E. Schiebel, J. M. Rieser, H. Choset, R. W. Blob, and D. I. Goldman, “Tail use improves performance on soft substrates in models of early vertebrate land locomotors,” *Science*, vol. 353, no. 6295, pp. 154–158, 2016. eprint: <http://science.sciencemag.org/content/353/6295/154.full.pdf>.

- [22] Y. Ozkan Aydin, B. Chong, C. Gong, J. Rieser, J. Rankin, K. Michel, A. Nicieza, J. Hutchinson, H. Choset, and D. Goldman, “Geometric mechanics applied to tetrapod locomotion on granular media,” *Lecture Notes in Computer Science (including subseries Lecture Notes in Artificial Intelligence and Lecture Notes in Bioinformatics)*, vol. 10384 LNAI, pp. 595–603, 2017.
- [23] J. Melli, C. Rowley, and D. Rufat, “Motion planning for an articulated body in a perfect planar fluid,” *SIAM Journal on Applied Dynamical Systems*, vol. 5, no. 4, pp. 650–669, 2006. eprint: <https://doi.org/10.1137/060649884>.
- [24] D. Tam and A. E. Hosoi, “Optimal stroke patterns for purcell’s three-link swimmer,” *Phys. Rev. Lett.*, vol. 98, p. 068 105, 6 Feb. 2007.
- [25] R. L. Hatton, Y. Ding, H. Choset, and D. I. Goldman, “Geometric visualization of self-propulsion in a complex medium,” *Phys. Rev. Lett.*, vol. 110, p. 078 101, 7 Feb. 2013.
- [26] C. Gong, D. I. Goldman, and H. Choset, “Simplifying gait design via shape basis optimization,” in *Robotics: Science and Systems XII, University of Michigan, Ann Arbor, Michigan, USA, June 18 - June 22, 2016*, 2016.
- [27] J. Dai, H. Faraji, C. Gong, R. L. Hatton, D. I. Goldman, and H. Choset, “Geometric swimming on a granular surface,” in *Proceedings of Robotics: Science and Systems*, AnnArbor, Michigan, Jun. 2016.
- [28] J. Aguilar, T. Zhang, F. Qian, M. Kingsbury, B. McInroe, N. Mazouchova, C. Li, R. Maladen, C. Gong, M. Travers, *et al.*, “A review on locomotion robophysics: The study of movement at the intersection of robotics, soft matter and dynamical systems,” *Reports on Progress in Physics*, vol. 79, no. 11, p. 110 001, 2016.
- [29] T. Zhang and D. I. Goldman, “The effectiveness of resistive force theory in granular locomotion,” *Physics of Fluids*, vol. 26, no. 10, p. 101 308, 2014. eprint: <https://doi.org/10.1063/1.4898629>.
- [30] R. Warkentin, W. Savoie, and D. I. Goldman, “Locomoting robots composed of immobile robots,” in *2018 Second IEEE International Conference on Robotic Computing (IRC)*, IEEE, 2018, pp. 224–227.
- [31] P. E. Schiebel, J. M. Rieser, A. M. Hubbard, L. Chen, and D. I. Goldman, “Collisional diffraction emerges from simple control of limbless locomotion,” in *Biomimetic and Biohybrid Systems*, M. Mangan, M. Cutkosky, A. Mura, P. F. Verschure, T. Prescott, and N. Lepora, Eds., Cham: Springer International Publishing, 2017, pp. 611–618, ISBN: 978-3-319-63537-8.

- [32] X. Xiong, A. D. Ames, and D. I. Goldman, “A stability region criterion for flat-footed bipedal walking on deformable granular terrain,” in *2017 IEEE/RSJ International Conference on Intelligent Robots and Systems (IROS)*, Sep. 2017, pp. 4552–4559.
- [33] H. C. Astley, C. Gong, J. Dai, M. Travers, M. M. Serrano, P. A. Vela, H. Choset, J. R. Mendelson, D. L. Hu, and D. I. Goldman, “Modulation of orthogonal body waves enables high maneuverability in sidewinding locomotion,” *Proceedings of the National Academy of Sciences*, vol. 112, no. 19, pp. 6200–6205, 2015. eprint: <https://www.pnas.org/content/112/19/6200.full.pdf>.
- [34] J. Aguilar, A. Lesov, K. Wiesenfeld, and D. I. Goldman, “Lift-off dynamics in a simple jumping robot,” *Phys. Rev. Lett.*, vol. 109, p. 174 301, 17 Oct. 2012.
- [35] R. Ablowitz, “The theory of emergence,” *Philosophy of Science*, vol. 6, no. 1, pp. 1–16, 1939.
- [36] A. Clark, L. Kondic, and R. Behringer, “Particle scale dynamics in granular impact,” *Physical review letters*, vol. 109, p. 238 302, Dec. 2012.
- [37] T. Pöschel and T. Schwager, “Computational granular dynamics,” *Computational Granular Dynamics: Models and Algorithms*, ISBN 978-3-540-21485-4. Springer-Verlag Berlin Heidelberg, 2005, Jan. 2005.
- [38] J. Lee and H J Herrmann, “Angle of repose and angle of marginal stability: Molecular dynamics of granular particles,” *Journal of Physics A: Mathematical and General*, vol. 26, p. 373, Jan. 1999.
- [39] Y. Ding, S. S. Sharpe, A. Masse, and D. I. Goldman, “Mechanics of undulatory swimming in a frictional fluid,” *PLOS Computational Biology*, vol. 8, no. 12, pp. 1–13, Dec. 2012.
- [40] R. D. Maladen, Y. Ding, P. B. Umbanhowar, A. Kamor, and D. I. Goldman, “Mechanical models of sandfish locomotion reveal principles of high performance sub-surface sand-swimming,” *Journal of The Royal Society Interface*, vol. 8, no. 62, pp. 1332–1345, 2011.
- [41] T. Larsson, “Multibody dynamic simulation in product development,” PhD thesis, Jan. 2001, p. 60.
- [42] A. Tasora, R. Serban, H. Mazhar, A. Pazouki, D. Melanz, J. Fleischmann, M. Taylor, H. Sugiyama, and D. Negrut, “Chrono: An open source multi-physics dynamics engine,” Jun. 2016, pp. 19–49, ISBN: 978-3-319-40360-1.

- [43] Project Chrono, *Chrono: An Open Source Framework for the Physics-Based Simulation of Dynamic Systems*, <http://projectchrono.org>, Accessed: 2019-01-17.
- [44] R. Al Nazer, A. Klodowski, T. Rantalainen, A. Heinonen, H. Sievänen, and A. Mikkola, “Analysis of dynamic strains in tibia during human locomotion based on flexible multibody approach integrated with magnetic resonance imaging technique,” *Multibody System Dynamics*, vol. 20, no. 4, pp. 287–306, Nov. 2008.
- [45] K. O’Riordain, P. Thomas, J. Phillips, and M. Gilchrist, “Reconstruction of real world head injury accidents resulting from falls using multibody dynamics,” *Clinical Biomechanics*, vol. 18, no. 7, pp. 590–600, 2003.
- [46] G. Ilewicz, “Multibody model of dynamics and optimization of medical robot to soft tissue surgery,” in *Advanced Mechatronics Solutions*, R. Jabłoński and T. Brezina, Eds., Cham: Springer International Publishing, 2016, pp. 129–134, ISBN: 978-3-319-23923-1.
- [47] W. Savoie, S. Cannon, J. J. Daymude, R. Warkentin, S. Li, A. W. Richa, D. Randall, and D. I. Goldman, “Phototactic supersmarticles,” *Artificial Life and Robotics*, Sep. 2018.
- [48] M. R. R. Playter M. Buehler, “Bigdog,” vol. 6230, 2006, pp. 6230–6230–6.
- [49] T. Zhang, “Modeling and control of locomotion in complex environments,” PhD thesis, Apr. 2016.
- [50] C. K. Liu and S. Jain, “A quick tutorial on multibody dynamics,”
- [51] A. Tasora and M. Anitescu, “A matrix-free cone complementarity approach for solving large-scale, nonsmooth, rigid body dynamics,” *Computer Methods in Applied Mechanics and Engineering*, vol. 200, no. 5, pp. 439–453, 2011.
- [52] P. G. De Gennes, “Tight knots,” *Macromolecules*, vol. 17, no. 4, pp. 703–704, 1984. eprint: <https://doi.org/10.1021/ma00134a030>.
- [53] M. Backholm, R. D. Schulman, W. S. Ryu, and K. Dalnoki-Veress, “Tangling of tethered swimmers: Interactions between two nematodes,” *Physical review letters*, vol. 113, no. 13, p. 138 101, 2014.
- [54] H. S. Fisher, L. Giomi, H. E. Hoekstra, and L. Mahadevan, “The dynamics of sperm cooperation in a competitive environment,” *Proceedings of the Royal Society B: Biological Sciences*, vol. 281, no. 1790, p. 20 140 296, 2014.

- [55] M. F. Copeland and D. B. Weibel, “Bacterial swarming: A model system for studying dynamic self-assembly,” *Soft matter*, vol. 5, no. 6, pp. 1174–1187, 2009.
- [56] J. Dunkel, S. Heidenreich, K. Drescher, H. H. Wensink, M. Bär, and R. E. Goldstein, “Fluid dynamics of bacterial turbulence,” *Phys. Rev. Lett.*, vol. 110, p. 228 102, 22 May 2013.
- [57] C. W. Reynolds, “Flocks, herds and schools: A distributed behavioral model,” *SIG-GRAPH Comput. Graph.*, vol. 21, no. 4, pp. 25–34, Aug. 1987.
- [58] T. Vicsek, A. Czirók, E. Ben-Jacob, I. Cohen, and O. Shochet, “Novel type of phase transition in a system of self-driven particles,” *Phys. Rev. Lett.*, vol. 75, pp. 1226–1229, 6 Aug. 1995.
- [59] I. D. Couzin and N. R. Franks, “Self-organized lane formation and optimized traffic flow in army ants,” *Proceedings of the Royal Society of London. Series B: Biological Sciences*, vol. 270, no. 1511, pp. 139–146, 2003.
- [60] R. Olfati-Saber, “Flocking for multi-agent dynamic systems: Algorithms and theory,” *IEEE Transactions on Automatic Control*, vol. 51, no. 3, pp. 401–420, Mar. 2006.
- [61] R. Beckers, O. Holland, and J.-L. Deneubourg, “From local actions to global tasks: Stigmergy and collective robotics,” 1994.
- [62] C. Kube and E. Bonabeau, “Cooperative transport by ants and robots,” *Robotics and Autonomous Systems*, vol. 30, no. 1, pp. 85–101, 2000.
- [63] B. Guénard, M. Weiser, K. Gomez, N. Narula, and E. P. Economo, *The global ant biodiversity informatics (gabi) database: A synthesis of ant species geographic distributions*, 2017.
- [64] J. Janicki, N. Narula, M. Ziegler, B. Guénard, and E. P. Economo, *Visualizing and interacting with large-volume biodiversity data using client-server web-mapping applications: The design and implementation of antmaps.org*. 2016.
- [65] W. R. Tschinkel, *The fire ants*. Cambridge, Mass.: The Belknap Press of Harvard University Press, 2006.
- [66] Wikipedia contributors, *Solenopsis invicta*, [Online; accessed 30-January-2019], 2019.
- [67] N. Gravish, “Collective dynamics of matter with granularity,” PhD thesis, May 2013.

- [68] N. Gravish, D. Monaenkova, M. A. D. Goodisman, and D. I. Goldman, “Climbing, falling, and jamming during ant locomotion in confined environments,” *Proceedings of the National Academy of Sciences*, vol. 110, no. 24, pp. 9746–9751, 2013. eprint: <http://www.pnas.org/content/110/24/9746.full.pdf>.
- [69] W. Savoie, Z. Jackson, S. Li, R. Warkentin, K. Wiesenfeld, and D. I. Goldman, “Emergent collective self-propulsion via shape-changing immotile robots,” Submitted.
- [70] M. Nicole, G. Nick, S. Andrei, and G. D. I., “Utilization of granular solidification during terrestrial locomotion of hatchling sea turtles,” *Biology Letters*, vol. 6, no. 3, pp. 398–401, Jun. 2010.
- [71] C. Li, P. B. Umbanhowar, H. Komsuoglu, D. E. Koditschek, and D. I. Goldman, “Sensitive dependence of the motion of a legged robot on granular media,” *Proceedings of the National Academy of Sciences*, vol. 106, no. 9, pp. 3029–3034, 2009. eprint: <https://www.pnas.org/content/106/9/3029.full.pdf>.
- [72] A. J. Liu and S. R. Nagel, “Jamming is not just cool any more,” *Nature*, vol. 396, Nov. 1998.
- [73] P. B. Umbanhowar, F. Melo, and H. L. Swinney, “Localized excitations in a vertically vibrated granular layer,” *Nature*, vol. 382, no. 6594, pp. 793–796, 1996.
- [74] N. Mazouchova, N. Gravish, A. Savu, and D. I. Goldman, “Utilization of granular solidification during terrestrial locomotion of hatchling sea turtles,” *Biology Letters*, vol. 6, no. 3, pp. 398–401, 2010.
- [75] N. Gravish, P. B. Umbanhowar, and D. I. Goldman, “Force and flow transition in plowed granular media,” *Phys. Rev. Lett.*, vol. 105, p. 128 301, 12 Sep. 2010.
- [76] ———, “Force and flow at the onset of drag in plowed granular media,” *Phys. Rev. E*, vol. 89, p. 042 202, 4 Apr. 2014.
- [77] V. Deshpande and D. Cebon, “Micromechanical modeling of steady-state deformation in asphalt,” *Journal of Materials in Civil Engineering - J MATER CIVIL ENG*, vol. 16, Apr. 2004.
- [78] A. N. A. N. Schofield and j. a. Wroth Peter, *Critical state soil mechanics*. New York : McGraw-Hill, 1968, Includes bibliographies.
- [79] Y. O. Aydin, J. M. Rieser, C. M. Hubicki, W. Savoie, and D. I. Goldman, “Physics approaches to natural locomotion: Every robot is an experiment,” in *Robotic Systems and Autonomous Platforms*, ser. Woodhead Publishing in Materials, S. M.

Walsh and M. S. Strano, Eds., Woodhead Publishing, 2019, pp. 109–127, ISBN: 978-0-08-102260-3.

- [80] J. Aguilar and D. I. Goldman, “Robophysical study of jumping dynamics on granular media,” *Nature Physics*, vol. 12, Nov. 2015, Article.
- [81] C. C. S., “Granular flows and gas-fluidization,” in. Jul. 2004, vol. 2, 1.
- [82] C. Li, A. M. Hoover, P. Birkmeyer, P. B. Umbanhowar, R. S. Fearing, and D. I. Goldman, “Systematic study of the performance of small robots on controlled laboratory substrates,” *Proceedings of SPIE*, vol. 7679, 2010.
- [83] O. Wiezel and Y. Or, “Optimization and small-amplitude analysis of purcell’s three-link microswimmer model,” *Proceedings of the Royal Society of London A: Mathematical, Physical and Engineering Sciences*, vol. 472, no. 2192, 2016. eprint: <http://rspa.royalsocietypublishing.org/content/472/2192/20160425.full.pdf>.
- [84] L. E. Becker, S. A. Koehler, and H. A. Stone, “On self-propulsion of micro-machines at low reynolds number: Purcell’s three-link swimmer,” *Journal of fluid mechanics*, vol. 490, pp. 15–35, 2003.
- [85] L. Giraldi, P. Martinon, and M. Zoppello, “Optimal design of purcell’s three-link swimmer,” *Physical Review E*, vol. 91, no. 2, p. 023 012, 2015.
- [86] L. Y. Vorocheva, G. S. Naumov, and S. F. Yatsun, “Simulation of motion of a three-link robot with controlled friction forces on a horizontal rough surface,” *Journal of Computer and Systems Sciences International*, vol. 54, no. 1, pp. 151–164, Jan. 2015.
- [87] F. L. Chernousko, “Simulation and optimization of crawling robots,” in *Modeling, Simulation and Optimization of Complex Processes*, Springer, 2005, pp. 85–104.
- [88] Y. Ozkan Aydin, J. Molnar, D. I. Goldman, and F. L. Hammond, “Design of a soft robophysical earthworm model,” Apr. 2018, pp. 83–87.
- [89] B. Trimmer, H.-T. Lin, A. Baryshyan, G. G. Leisk, and D. Kaplan, “Towards a biomorphic soft robot: Design constraints and solutions,” Jun. 2012, pp. 599–605, ISBN: 978-1-4577-1199-2.
- [90] D. Accoto, P. Castrataro, and P. Dario, “Biomechanical analysis of oligochaeta crawling,” *Journal of Theoretical Biology*, vol. 230, no. 1, pp. 49–55, 2004.
- [91] L. I. van Griethuijsen and B. A. Trimmer, “Kinematics of horizontal and vertical caterpillar crawling,” *Journal of Experimental Biology*, vol. 212, no. 10, pp. 1455–

1462, 2009. eprint: <http://jeb.biologists.org/content/212/10/1455.full.pdf>.

- [92] J. Teran, L. Fauci, and M. Shelley, “Viscoelastic fluid response can increase the speed and efficiency of a free swimmer,” *Phys. Rev. Lett.*, vol. 104, p. 038 101, 3 Jan. 2010.
- [93] E. Lauga and T. R. Powers, “The hydrodynamics of swimming microorganisms,” *Reports on Progress in Physics*, vol. 72, no. 9, p. 096 601, 2009.
- [94] J. Yu, B. Wang, X. Du, Q. Wang, and L. Zhang, “Ultra-extensible ribbon-like magnetic microswarm,” *Nature Communications*, vol. 9, no. 1, p. 3260, 2018.
- [95] D. I Goldman, T. S Chen, D. M Dudek, and R. J Full, “Dynamics of rapid vertical climbing in cockroaches reveals a template,” vol. 209, pp. 2990–3000, Sep. 2006.
- [96] E. Frazzoli, M. A. Dahleh, and E. Feron, “Real-time motion planning for agile autonomous vehicles,” *Journal of guidance, control, and dynamics*, vol. 25, no. 1, pp. 116–129, 2002.
- [97] R. Mahony, V. Kumar, and P. Corke, “Multirotor aerial vehicles,” *IEEE Robotics and Automation magazine*, vol. 20, no. 32, 2012.
- [98] M. Raibert, K. Blankespoor, G. Nelson, and R. Playter, “Bigdog, the rough-terrain quadruped robot,” *IFAC Proceedings Volumes*, vol. 41, no. 2, pp. 10822 –10 825, 2008, 17th IFAC World Congress.
- [99] M. Yim, W. Shen, B. Salemi, D. Rus, M. Moll, H. Lipson, E. Klavins, and G. S. Chirikjian, “Modular self-reconfigurable robot systems [grand challenges of robotics],” *IEEE Robotics Automation Magazine*, vol. 14, no. 1, pp. 43–52, Mar. 2007.
- [100] E. Pinçe, S. K. P. Velu, A. Callegari, P. Elahi, S. Gigan, G. Volpe, and G. Volpe, “Disorder-mediated crowd control in an active matter system,” *Nature Communications*, vol. 7, 10907 EP –, Mar. 2016.
- [101] J. K. Parrish and W. M. Hammer, *Animal Groups in Three Dimensions: How Species Aggregate (Psychiatry and Medicine)*. Cambridge University Press, 1997.
- [102] F. J. Ndlec, T. Surrey, A. C. Maggs, and S. Leibler, “Self-organization of microtubules and motors,” *Nature*, vol. 389, no. 6648, pp. 305–308, Sep. 1997.
- [103] J. Palacci, S. Sacanna, A. P. Steinberg, D. J. Pine, and P. M. Chaikin, “Living crystals of light-activated colloidal surfers,” *Science*, vol. 339, no. 6122, pp. 936–940, 2013.

- [104] A. P. Petroff, X.-L. Wu, and A. Libchaber, “Fast-moving bacteria self-organize into active two-dimensional crystals of rotating cells,” *Phys. Rev. Lett.*, vol. 114, p. 158 102, 15 Apr. 2015.
- [105] L. Giomi, N. Hawley-Weld, and L. Mahadevan, “Swarming, swirling and stasis in sequestered bristle-bots,” *Proceedings of the Royal Society of London A: Mathematical, Physical and Engineering Sciences*, vol. 469, no. 2151, 2013.
- [106] Z. Gao, H. Li, X. Chen, and H. P. Zhang, “Using confined bacteria as building blocks to generate fluid flow,” *Lab Chip*, vol. 15, pp. 4555–4562, 24 2015.
- [107] A. Deblais, T. Barois, T. Guerin, P. H. Delville, R. Vaudaine, J. S. Lintuvuori, J. F. Boudet, J. C. Baret, and H. Kellay, “Boundaries control collective dynamics of inertial self-propelled robots,” *Phys. Rev. Lett.*, vol. 120, p. 188 002, 18 May 2018.
- [108] N. Gravish, S. V. Franklin, D. L. Hu, and D. I. Goldman, “Entangled granular media,” *Phys. Rev. Lett.*, vol. 108, p. 208 001, 20 May 2012.
- [109] Since experiments were terminated at a specific time, rather than when all interactions stopped, the cloud granular temperature in Fig. 4.2 (c) does not reach the average noise floor.
- [110] K. Zahedi and N. Ay, “Quantifying morphological computation,” *Entropy*, vol. 15, no. 5, pp. 1887–1915, 2013.
- [111] Z. Derakhshandeh, R. Gmyr, A. W. Richa, C. Scheideler, and T. Strothmann, “Universal shape formation for programmable matter,” in *Proceedings of the 28th ACM Symposium on Parallelism in Algorithms and Architectures*, ACM, 2016, pp. 289–299.
- [112] R. M. Fuchsli and Andrej Dzyakanchuk and Dandolo Flumini and Helmut Hauser and Kenneth J. Hunt and Rolf H. Luchsinger and Benedikt Reller and Stephan Scheidegger and Richard Walker, “Morphological computation and morphological control: Steps toward a formal theory and applications,” *Artificial life*, vol. 19 1, pp. 9–34, 2013.
- [113] J. Li, B. E.-F. de Ávila, W. Gao, L. Zhang, and J. Wang, “Micro/nanorobots for biomedicine: Delivery, surgery, sensing, and detoxification,” *Sci. Robot.*, vol. 2, no. 4, 2017.
- [114] S. Li, Q. Jiang, S. Liu, Y. Zhang, Y. Tian, C. Song, J. Wang, Y. Zou, G. J. Anderson, J.-Y. Han, *et al.*, “A dna nanorobot functions as a cancer therapeutic in response to a molecular trigger in vivo,” *Nature biotechnology*, vol. 36, no. 3, p. 258, 2018.

- [115] S. Yim and M. Sitti, “Shape-programmable soft capsule robots for semi-implantable drug delivery,” *IEEE Transactions on Robotics*, vol. 28, no. 5, pp. 1198–1202, 2012.
- [116] C. Li, A. O. Pullin, D. W. Haldane, H. K. Lam, R. S. Fearing, and R. J. Full, “Terradynamically streamlined shapes in animals and robots enhance traversability through densely cluttered terrain,” *Bioinspiration & biomimetics*, vol. 10, no. 4, p. 046 003, 2015.
- [117] E. Moore and C. Shannon, “Reliable circuits using less reliable relays,” *Journal of the Franklin Institute*, vol. 262, no. 3, pp. 191 –208, 1956.
- [118] C. H. Hsueh and W. C. J. Wei, “Effective viscosity of semidilute suspensions of rigid ellipsoids,” *Journal of Applied Physics*, vol. 107, no. 2, p. 024 905, 2010. eprint: <https://doi.org/10.1063/1.3283925>.
- [119] E. Brown, H. Zhang, N. A. Forman, B. W. Maynor, D. E. Betts, J. M. DeSimone, and H. M. Jaeger, “Shear thickening and jamming in densely packed suspensions of different particle shapes,” *Phys. Rev. E*, vol. 84, p. 031 408, 3 Sep. 2011.
- [120] R. G. Egres and N. J. Wagner, “The rheology and microstructure of acicular precipitated calcium carbonate colloidal suspensions through the shear thickening transition,” *Journal of Rheology*, vol. 49, no. 3, pp. 719–746, 2005. eprint: <https://doi.org/10.1122/1.1895800>.
- [121] R. C. Kramb and C. F. Zukoski, “Nonlinear rheology and yielding in dense suspensions of hard anisotropic colloids,” *Journal of Rheology*, vol. 55, no. 5, pp. 1069–1084, 2011. eprint: <https://doi.org/10.1122/1.3613978>.
- [122] W. Man, A. Donev, F. H. Stillinger, M. T. Sullivan, W. B. Russel, D. Heeger, S. Inati, S. Torquato, and P. M. Chaikin, “Experiments on random packings of ellipsoids,” *Phys. Rev. Lett.*, vol. 94, p. 198 001, 19 May 2005.
- [123] K. Desmond and S. V. Franklin, “Jamming of three-dimensional prolate granular materials,” *Phys. Rev. E*, vol. 73, p. 031 306, 3 Mar. 2006.
- [124] M. Z. Miskin and H. M. Jaeger, “Evolving design rules for the inverse granular packing problem,” *Soft Matter*, vol. 10, pp. 3708–3715, 21 2014.
- [125] M. Trepanier and S. V. Franklin, “Column collapse of granular rods,” *Phys. Rev. E*, vol. 82, p. 011 308, 1 Jul. 2010.
- [126] J. Blouwolff and S. Fraden, “The coordination number of granular cylinders,” *EPL (Europhysics Letters)*, vol. 76, no. 6, p. 1095, 2006.

- [127] M. Tennenbaum, Z. Liu, D. Hu, and A. Fernandez-Nieves, “Mechanics of fire ant aggregations,” *Nature Materials*, vol. 15, Oct. 2015.
- [128] N. J. Mlot, C. A. Tovey, and D. L. Hu, “Fire ants self-assemble into waterproof rafts to survive floods,” *Proceedings of the National Academy of Sciences*, vol. 108, no. 19, pp. 7669–7673, 2011. eprint: <http://www.pnas.org/content/108/19/7669.full.pdf>.
- [129] N. J. Mlot, C. Tovey, and D. L. Hu, “Dynamics and shape of large fire ant rafts,” *Communicative & Integrative Biology*, vol. 5, no. 6, pp. 590–597, 2012, PMID: 23336030. eprint: <https://doi.org/10.4161/cib.21421>.
- [130] M. A. McEvoy and N. Correll, “Materials that couple sensing, actuation, computation, and communication,” *Science*, vol. 347, no. 6228, p. 1 261 689, 2015.
- [131] G. P. Markin, J. O’Neal, and J. Dillier, “Foraging tunnels of the red imported fire ant, *solenopsis invicta* (hymenoptera: Formicidae),” *Journal of the Kansas Entomological Society*, vol. 48, no. 1, pp. 83–89, 1975.
- [132] J. C. Jones and B. P. Oldroyd, “Nest thermoregulation in social insects,” in, ser. *Advances in Insect Physiology*, S. Simpson, Ed., vol. 33, Academic Press, 2006, pp. 153–191.
- [133] J. Gould and C. Gould, *Animal Architects: Building and the Evolution of Intelligence*. Basic Books, 2007, ISBN: 9780465027828.
- [134] M. Hansell, “Animal architecture,” in. Jan. 2005.
- [135] B. Holldobler and E. O. Wilson, *The ants*. Springer Berlin, 1990, ISBN: 3540520929.
- [136] S. Wolfram, “Statistical mechanics of cellular automata,” *Rev. Mod. Phys.*, vol. 55, pp. 601–644, 3 Jul. 1983.
- [137] ———, *A New Kind of Science*. Wolfram Media Inc., 2002, ISBN: 1-57955-008-8.
- [138] P. Bak, C. Tang, and K. Wiesenfeld, “Self-organized criticality: An explanation of the 1/f noise,” *Phys. Rev. Lett.*, vol. 59, pp. 381–384, 4 Jul. 1987.
- [139] H Puhl, “On the modeling of real sand piles,” *Physica A: Statistical Mechanics and its Applications*, vol. 182, Mar. 1992.
- [140] H. Nishimori and N. Ouchi, “Computational models for sand ripple and sand dune formation,” *International Journal of Modern Physics B*, vol. 07, pp. 2025–2034, 1993. eprint: <https://doi.org/10.1142/S0217979293002742>.

- [141] ———, “Formation of ripple patterns and dunes by wind-blown sand,” *Physical Review Letters - PHYS REV LETT*, vol. 71, Oct. 1993.
- [142] N. Gravish, G. Gold, A. Zangwill, M. A. D. Goodisman, and D. I. Goldman, “Glass-like dynamics in confined and congested ant traffic,” *Soft Matter*, vol. 11, pp. 6552–6561, 33 2015.
- [143] P. Tenczar, C. C. Lutz, V. D. Rao, N. Goldenfeld, and G. E. Robinson, “Automated monitoring reveals extreme interindividual variation and plasticity in honeybee foraging activity levels,” *Animal Behaviour*, vol. 95, pp. 41–48, 2014.
- [144] *Matlab optimization toolbox*, The MathWorks, Natick, MA, USA, 2017b.
- [145] D. Monaenkova, N. Gravish, G. Rodriguez, R. Kutner, M. A. D. Goodisman, and D. I. Goldman, “Behavioral and mechanical determinants of collective subsurface nest excavation,” *Journal of Experimental Biology*, vol. 218, no. 9, pp. 1295–1305, 2015. eprint: <http://jeb.biologists.org/content/218/9/1295.full.pdf>.
- [146] C. R. Reid, M. J. Lutz, S. Powell, A. B. Kao, I. D. Couzin, and S. Garnier, “Army ants dynamically adjust living bridges in response to a cost–benefit trade-off,” *Proceedings of the National Academy of Sciences*, vol. 112, no. 49, pp. 15 113–15 118, 2015. eprint: <http://www.pnas.org/content/112/49/15113.full.pdf>.
- [147] C. Gershenson and D. Helbing, “When slower is faster,” *Complexity*, vol. 21, no. 2, pp. 9–15, 2015. eprint: <https://onlinelibrary.wiley.com/doi/pdf/10.1002/cplx.21736>.
- [148] K. Nagel and M. Schreckenberg, “A cellular automaton model for freeway traffic,” *Journal de Physique I*, vol. 2, pp. 2221–2229, Dec. 1992.
- [149] R. KUHNE, “Traffic patterns in unstable traffic flow on freeways,” *Highway Capacity and Level of Service*, pp. 211–223, 1991.
- [150] H.-S. Kuan and M. D. Betterton, “Phase-plane analysis of the totally asymmetric simple exclusion process with binding kinetics and switching between antiparallel lanes,” *Phys. Rev. E*, vol. 94, p. 022 419, 2 Aug. 2016.